UC Santa Cruz

UC Santa Cruz Electronic Theses and Dissertations

Title

Synthesis, Characterization, Surface Tailoring, and Applications of Hollow Gold Nanospheres and Perovskite Nanomaterial

Permalink

https://escholarship.org/uc/item/6h21756f

Author

Vickers, Evan

Publication Date

2020

Peer reviewed|Thesis/dissertation

eScholarship.org Powered by the California Digital Library
University of California

UNIVERSITY OF CALIFORNIA

SANTA CRUZ

Synthesis, Characterization, Surface Tailoring, and Applications of Hollow Gold Nanospheres and Perovskite Nanomaterial

A dissertation submitted in partial satisfaction

of the requirements for the degree of

DOCTOR OF PHILOSOPHY

in

CHEMISTRY

by

Evan Thomas Vickers

September 2020

The dissertation of
Evan Thomas
Vickers is approved:

_____
Professor Jin Z. Zhang,
Chair

_____
Professor Scott R. J. Oliver

_____
Professor Yat Li

_____
Quentin Williams
Acting Vice Provost and Dean of Graduate Studies

Copyright © by

Evan Thomas Vickers

2020

Table of Contents

List of Figures ..... **ix**

List of Tables ..... **xvi**

Abstract ..... **xvii**

Acknowledgements ..... **xx**

Dedication ..... **xxiii**

Chapter 1. Introduction **1**

1.1. Hollow Gold Nanospheres for Cancer Theranostics 1

1.1.1. Plasmonic Nanoparticles *1*

1.1.2. Hollow Gold Nanospheres *2*

1.1.3. Photothermal Therapy *3*

1.1.4. Two-Photon Spectroscopy *4*

1.2. Perovskite 5

1.2.1. Structure *5*

1.2.2. Organic-Inorganic Metal Halide Perovskite *5*

1.2.3. Electronic Properties *6*

1.3. Methylammonium Lead Bromide Perovskite Quantum Dots 8

1.3.1. Quantum Dots *8*

1.3.2. Methylammonium Lead Bromide Perovskite *8*

1.3.3. Charge Transport in PQD Solid Film *9*

1.3.4. Exciton-Delocalizing Ligands *10*

1.4. Magic Sized Clusters 11

1.4.1. Properties *11*

1.4.2. Synthesis and Characterization *12*

1.5. References 13

Chapter 2. Two-Photon Photoluminescence and Photothermal Properties of Hollow Gold Nanospheres for Efficient Theranostic Applications 28

2.1. Abstract 28

2.2. Introduction 29

2.3. Experimental Section 32

2.3.1. Synthesis and Characterization *32*

2.3.2. 2PPL Measurements of HGN and GNR in Solution *34*

2.3.3. Comparing HGN and GNR 2PPL yield *35*

2.3.4. Two-Photon Action Cross-Section Measurements *35*

2.3.5. Nonlinear Excitation Profile of HGNs *36*

2.3.6. Cell Culture *38*

2.3.7. Conjugation of Folic Acid-PEG-SH to HGNs *38*

2.3.8. Excitation Profile, Bioimaging, and Cancer Treatment *38*

2.4. Results and Discussions 40

2.5. Conclusions 57

2.6. References 57

Chapter 3. Dependence of Stability and Electronic and Optical Properties of Perovskite Quantum Dots on Capping Ligand Chain Length.....65

3.1. Abstract 65

3.2. Introduction 66

3.3. Experimental Section 68

3.3.1. Materials 68

3.3.2. Synthesis of $CH_3NH_3PbBr_3$ PQDs 69

3.3.3. Spectroscopy and Microscopy Measurements 69

3.3.4. Electroanalytical Measurements 70

3.3.5. Testing of Stability of PQDs 71

3.4. Results and Discussions 71

3.4.1. Electroanalytical Characterization 77

3.4.2. Stability of PQDs 80

3.4.3. Model of Charge Transport 83

3.5. Conclusions 86

3.6. References 86

Chapter 4. Improving Charge Carrier Delocalization in Perovskite Quantum Dots by Surface Passivation with Conductive Aromatic Ligands 92

4.1. Abstract 92

4.2. Introduction 92

4.3. Experimental Section 95

4.3.1. Materials *95*

4.3.2. BZA-BA-MAPbBr$_3$ QD Synthesis *96*

4.3.3. APTES-OA-MAPbBr$_3$ QD Synthesis *96*

4.3.4. OCTA-OA-MAPbBr$_3$ QD Synthesis *96*

4.3.5. UV-Vis Spectroscopy *97*

4.3.6. Fluorescence Spectroscopy *97*

4.3.7. X-Ray Diffraction Spectroscopy *98*

4.3.8. Fourier-Transform Infrared Spectroscopy *98*

4.3.9. Time-Correlated Single Photon Counting Spectroscopy *99*

4.3.10. Electrochemical Impedance Spectroscopy Measurement *100*

4.3.11. Cyclic Voltammetry Measurement *101*

4.3.12. Transient Photovoltage and Photocurrent Measurements *102*

4.3.13. References *102*

4.4. Results and Discussion 103

4.5. Conclusion 120

4.6. References 121

Chapter 5. Enhancing Charge Carrier Delocalization in Perovskite Quantum Dot Solids with Energetically Aligned Conjugated Capping Ligands 133

5.1. Abstract 133

5.2. Introduction 133

5.3. Experimental Section 136

5.3.1. Materials 136

5.3.2. Spectroscopy and Microscopy 137

5.3.3. Absolute PLQY 137

5.3.4. BTYA-VA,-TCA,-TFCA,-PFCA, and -MOCA $MAPbBr_3$ Synthesis 138

5.3.5. DPPA-VA,-TCA,-TFCA,-PFCA, and -MOCA $MAPbBr_3$ Synthesis 139

5.3.6. BTYA-OA and DPPA-OA MSC Synthesis 140

5.3.7. Fourier Transform-Infrared Spectroscopy 140

5.3.8. Ligand Exchange of BTYA-OA and DPPA-OA MSCs with TCA 141

5.3.9. Time-Correlated Single Photon Counting Spectroscopy 142

5.3.10. Calculation of Relevant Energy Levels for the Ligands 144

5.3.11. Electrochemical Impedance Spectroscopy 145

5.3.12. Photoelectrochemical Measurements 146

5.3.13. Transient Photovoltage and Photocurrent Measurements 148

5.3.14. PQD-based LED Fabrication 148

5.3.15. References 150

5.4. Results and Discussion.....151

5.5. Conclusion.....168

5.6. References.....169

Chapter 6. Ligand Dependent Growth and Optical Properties of Hybrid Organo-Metal Halide Perovskite Magic Sized Clusters.....177

6.1. Abstract.....177

6.2. Introduction.....178

6.3. Experimental Section.....179

6.3.1. Materials.....179

6.3.2. Synthesis of BTYA-VA PMSCs.....180

6.3.3. Synthesis of DPPA-VA PMSCs.....180

6.3.4. Spectroscopic Measurements.....181

6.3.5. Time-Correlated Single Photon Counting Spectroscopy.....181

6.4. Results and Discussion.....182

6.4.1. Synthesis and Characterization of PMSCs.....182

6.4.2. Growth and Stability of PMSCs.....186

6.4.3. Concentration Dependence of PL Emission of PMSCs.....189

6.4.4. Time-Correlated Single Photon Counting.....192

6.5. Conclusion.....194

6.6. References.....195

List of Figures

Figure 1.1.1. Conducting electrons coherent oscillatory response incident EM radiation in resonance. Figure reproduced with permission from Coordination Chemistry Reviews 2016, 320-321, 18-37. 1

Figure 1.2.1. The general structure of perovskite. 5

Figure 1.2.2. The electronic structure of OHMP. 7

Figure 2.3.1. a) The dependence of 2PPL emission intensity on the excitation power. Emission was detected in Channel 2 (495-540 nm) of the photomultiplier tube. At the excitation wavelength of 800 nm, with excitation pulse energy at 2.43 pJ, 3.01 pJ, 3.70 pJ, 4.49 pJ, 5.42 pJ, 6.44 pJ, and 8.4 pJ. b) The nonlinear 2PPL excitation spectra of HGNs (dotted lines) are plotted with the one-photon extinction spectrum that has SPR peaked at 780 nm. An incident pulse energy of 32.5 pJ was used for all excitation wavelengths.....37

Figure 2.4.1. UV-Vis spectra of HGNs a) and GNRs b). HR-TEM images of HGNs with peak SPR 790 nm c) and GNRs d). STEM images of HGNs with peak SPR 620 nm e), 680 nm f), and 786 nm g). 42

Figure 2.4.2. The 2PPL spectra of GNRs a) and HGNs b) measured using an 820 nm excitation source from a femtosecond Ti:Sapphire laser. Individual spectra were normalized to the same optical density at 820 nm, using Equation 2 in the experimental section. 47

Figure 2.4.3. Yellow color represents Channel 4 (575-630nm), green for Channel 2 (495-540 nm) and magenta for Channel 1 (420-460 nm). a) Z-scan images of HeLa cells taken 1.775 μm apart using HGN-FA (yellow). b) HeLa cell image using DAPI (magenta) and H GN-FA. c) Zoomed-out image of HeLa cells containing HGN-FA without DAPI, represented by overlap of Channel 1, Channel 2 and Channel 4. White color indicates similar intensity from all channels. d) FA linker with HeLa cells. e) HeLa cells only. 50

Figure 2.4.4. a) Confocal fluorescence microscopy images of cancer cells under the following conditions: HGN-FA+Laser, FA-PEG+Laser, HGN+Laser, Laser Only, FA-PEG Only, HGN Only, at 25, 32, and 39 mW average power. Red color represents dead cells stained with PI (propidium iodide) and live cells are represented as blue stained with DAPI (4,6-Diamidino-2-Phenylindole, Dihydrochloride). b) Multiphoton microscopy image of cancer cells during treatment using HGN-FA (green) and DAPI (blue). c) Irradiation power dependent viability of HeLa cells treated with HGN-FA+Laser, Cells+Laser, and HGN-FA only. d) Offset image from the scanned area exemplifying the precision of using laser scanning multiphoton microscopy for cancer therapy.....53

Figure 2.4.5. Bright-field transmission images of HeLa cells after three scans with multiphoton microscope at 800 nm wavelength and 39 mW average power: a) without HGN-FA incubation; b) with HGN-FA incubation; c) overlay image of (b) with ROS detection; ; d) without HGN-FA; e) overlay image of (d) with ROS detection; f) zoomed-in region of (c) presenting protein aggregation; g) zoomed-out image of (f) revealing dead cells stained with PI red dye; h) different zoomed-in region of (c)

displaying empty cavitating structures; i) using 25 mW average power, HeLa cell membrane blebbing and ROS. 56

Figure 3.4.1. UV-Vis absorption and PL spectra of (a) BUTY-VA, (b) OCTY-CA, and (c) DODE-LA $MAPbBr_3$ PQDs. HRTEM images of (d) BUTY-VA, (e) OCTY-CA, and (f) DODE-LA $MAPbBr_3$ PQDs. Inset shows lattice spacing image (red square is where measurement was made) and XRD. 73

Figure 3.4.2. FT-IR spectra of (a) BUTY-VA, (b) OCTY-CA, and (c) DODE-LA $MAPbBr_3$ PQDs. 76

Figure 3.4.3. Nyquist spectra of BUTY-VA, OCTY-CA, and DODE-LA $MAPbBr_3$ PQD films under 1 sun illumination (100 mW/cm^2) and dark conditions. Inset displays equivalent circuit. 78

Figure 3.4.4. Transient photocurrent response of BUTY-VA, OCTY-CA, and DODE-LA $MAPbBr_3$ PQD films. 79

Figure 3.4.5. The relative PL intensity versus time of BUTY-VA, OCTY-CA, and DODE-LA $MAPbBr_3$ PQDs under the conditions of (a) air and dark as well as (b) air, dark, and isopropanol solvent. 82

Figure 3.4.6. Model of charge transport mechanisms in BUTY-VA and OCTY-CA $MAPbBr_3$ PQD film in an electrochemical cell. (β) is the Butler-Volmer transfer factor. 85

Figure 4.3.1. UV-Vis and Fluorescence spectra of PQD films used in the EIS, CV, TPC, and TPV measurements. Dotted lines are Absorbance and solid lines are PL Intensity. 98

Figure 4.3.2. FTIR spectra of BZA ligand, BZA-BA-$MAPbBr_3$ QD, and $MAPbBr_3$ bulk in the mono-substituted aromatic C-H bending region.....99

Figure 4.4.1. UV-Vis absorption and PL spectra of (a) BZA-BA-$MAPbBr_3$, (b) APTES-OA-$MAPbBr_3$ and (c) OCTA-OA-$MAPbBr_3$ QDs. Inset is digital photograph of respective QD solution. (d) TEM image of BZA-BA-$MAPbBr_3$ QDs (scale bar 50 nm), lower left inset is HRTEM image with lattice spacing (scale bar 1 nm), and upper right inset is XRD with symbols assigned to the cubic phase. (e) TEM image of APTES-OA-$MAPbBr_3$ (scale bar 50 nm) and (f) OCTA-OA-$MAPbBr_3$ QDs (scale bar 20 nm). 106

Figure 4.4.2. FT-IR spectra of (a) BZA-BA-$MAPbBr_3$ QDs, (b) BZA free ligand, and (c) $MAPbBr_3$ bulk. 109

Figure 4.4.3. Time-resolved PL spectra of (a) BZA-BA-$MAPbBr_3$, (b) APTES-OA-$MAPbBr_3$, and (c) OCTA-OA-$MAPbBr_3$ QDs on SiO_2-B_2O_3 and ITO-TiO_2. 112

Figure 4.4.4. (a) Electrochemical impedance responses of FTO without film deposited, BZA-BA-$MAPbBr_3$, APTES-OA-$MAPbBr_3$, and OCTA-OA-$MAPbBr_3$ QD film deposited. (b) Cross-sectional SEM images of the different QD film deposits used for EIS measurements. Scale bars represent 2, 1, and 1 μm, respectively. 115

Figure 4.4.5. Cyclic voltammograms of (a) BZA-BA-$MAPbBr_3$, (b) APTES-OA-$MAPbBr_3$, and (c) OCTA-OA-$MAPbBr_3$ QD film. FTO electrode with QD film deposit is represented by the blue line and FTO without QD film is in red. 117

Figure 4.4.6. AFM topography images of (a) BZA-BA-$MAPbBr_3$, (b) APTES-OA-$MAPbBr_3$, and (c) OCTA-OA-$MAPbBr_3$ PQD films. Red square indicates area

measured. (d) Normalized TPC decay curve and (e) normalized TPV decay curve from the corresponding PQDs. 120

Figure 5.3.1. Diagram of integrated sphere for measuring absolute PLQY. 138

Figure 5.3.2. FT-IR spectra of each $MAPbBr_3$ PQD in ranges with characteristic TCA, TFCA, PFCA, or MOCA peaks. 141

Figure 5.3.3. Diagram of energy levels between PQD core and ligands TCA, TFCA, PFCA, and MOCA. Solid lines are values from references 5 and 6, and dashed lines are calculated results from this work. 145

Figure 5.3.4. Transient photocurrent response of (a) BTYA-VA,-TCA,-TFCA,-PFCA, and -MOCA and (b) DPPA-VA,-TCA,-TFCA,-PFCA, and -MOCA $MAPbBr_3$ PQD films on FTO substrate. Every 25 sec. PQD films were exposed to one sun illumination (100 mW/cm^2).....147

Figure 5.3.5. Current density-voltage (J-V) curve of DPPA-TCA and DPPA-VA $MAPbBr_3$ PQD-based LEDs. Inset is SEM cross-sectional image and digital photograph of device.....149

Figure 5.3.6. Electroluminescence spectra of DPPA-TCA $MAPbBr_3$ PQD-based LED. 150

Figure 5.4.1. UV-vis absorption (solid line) and PL spectra (dotted line) of (a) BTYA-VA (a, red), -TCA (b, blue), -TFCA (c, green), -PFCA (d, orange), and -MOCA (e, magenta) and (b) DPPA-VA (a, red), -TCA (b, blue), -TFCA (c, green), -PFCA (d, orange), and -MOCA (e, magenta) $MAPbBr_3$ PQDs suspended in toluene. (c) HRTEM image of $MAPbBr_3$ PQDs passivated with DPPA-TCA (scale bar 10 nm). The lower left inset is image of lattice spacing (scale bar 2 nm). (d) HRTEM image of BTYA-

TCA $MAPbBr_3$ PQDs (scale bar 10 nm), and the lower left inset is lattice spacing image (scale bar 2 nm). HRTEM images are similar with respect to BTYA or DPPA amine with each acid. 154

Figure 5.4.2. UV-vis absorption spectra of (a) BTYA-OA and (b) DPPA-OA MSCs before and after ligand exchange with TCA. FT-IR spectra of (c) BTYA-OA and (d) DPPA-OA MSCs before and after ligand exchange with TCA in the C-H aromatic region, and (e) BTYA-OA and (f) DPPA-OA MSCs before and after ligand exchange with TCA in the C=O stretching region.....158

Figure 5.4.3. Time-resolved PL spectra of (a) BTYA-VA (e, red), -TCA (a, blue), -TFCA (d, green), -PFCA (c, orange), and -MOCA (b, magenta) and (b) DPPA-VA (e, red), -TCA (b, blue), -TFCA (d, green), -PFCA (c, orange), and -MOCA (a, magenta) $MAPbBr_3$ PQD film on borosilicate glass substrate. Inset displays $\tau 1$, $\tau 2$, $A1$, $A2$, and τave representing the fast and slow decay component lifetime and amplitude, and average PL lifetime, respectively.....161

Figure 5.4.4. Nyquist spectra of (a) BTYA-VA, -TCA,-TFCA, -PFCA, and -MOCA and (b) DPPA-VA, -TCA, -TFCA, -PFCA, and -MOCA $MAPbBr_3$ PQD film on FTO substrate under one sun illumination (100 mW/cm^2). Inset displays equivalent circuit. 164

Figure 5.4.5. AFM topography images of (a) DPPA-VA, (b) DPPA-TCA, (c) DPPA-TFCA, (d) DPPA-PFCA, and (e) DPPA-MOCA $MAPbBr_3$ PQD films on FTO substrate. The area in the red square is where films were measured for TPC and TPV. (f) TPC decay curves of DPPA-VA (e, red), -TCA (b, blue), -TFCA (a, green), -PFCA (d, orange), and -MOCA (c, magenta) $MAPbBr_3$ PQD films. (g) TPV decay curves of

DPPA-VA (b, red), -TCA (e, blue), -TFCA (c, green), -PFCA (a, orange), and -MOCA (d, magenta) $MAPbBr_3$ PQD films. 167

Figure 6.4.1. UV-Vis absorption and PL spectra of (A) BTYA-VA and (B) DPPA-VA PMSCs. Insets contain amine capping ligand and digital photographs of the respective PMSC solution. 183

Figure 6.4.2. FTIR spectra of DPPA-VA PMSCs and DPPA PQDs. 185

Figure 6.4.3. UV-Vis absorption and PL spectra of (A) BTYA-VA and (B) DPPA-VA PMSCs overtime. The lightest band in each spectrum represents the measurement taken at 24 hours. 188

Figure 6.4.4. Stability of DPPA-VA MSCs and BTYA-VA MSCs solution in air and in the dark: the relative fluorescence intensity as a function of exposure time. 189

Figure 6.4.5. PL spectra of (A) BTYA-VA and (B) DPPA-VA PMSCs in a series dilution. PL spectra were measured during the initial dilution, and then after 2 hours and 24 hours. Insets contain digital photographs after each measurement. 191

Figure 6.4.6. DPPA-VA PMSC's PL spectra in a series dilution using chloroform. 191

Figure 6.4.7. Time-resolved photoluminescence spectra of (blue) BTYA-VA and (green) DPPA-VA PMSCs. 194

List of Tables

Table 2.4-1 SPR band position, dimension, normalized integrated 2PPL intensity, and molar extinction coefficient and two-photon action cross-section at 820 nm of HGNs and GNRs. 41

Table 5.3-1 Non-radiative and radiative lifetimes of each $MAPbBr_3$ PQD calculated using absolute PLQY. 144

Table 5.4-1 Absolute PLQY of $MAPbBr_3$ QDs and molecular structure of a) TCA, b) TFCA, c) PFCA, d) MOCA, e) VA, f) BTYA, and g) DPPA. 153

Table 5.4-2 Series resistance (R_s), charge transport resistance (R_{CT}), and charge transfer lifetime (τ_{rel}) of each $MAPbBr_3$ PQD film on FTO substrate. 165

Synthesis, Characterization, Surface Tailoring, and Applications of Hollow Gold Nanospheres and Perovskite Nanomaterial

Evan Thomas Vickers

Abstract

Two-photon photoluminescence (2PPL) together with hollow gold nanosphere's (HGN's) photothermal properties are utilized as a single theranostic agent for cancer. HGNs bioconjugated with folic acid-PEG-thiol (HGN-FA) selectively bind to the overexpressed folate receptor of cervical cancer HeLa cells and the 2PPL from HGN-FA captures high-resolution cancer cells images using multiphoton microscopy. Subsequent power increase and laser scanning dwell time results in highly efficient photothermal destruction of cancer cells. Using femtosecond laser pulses, microseconds of laser exposure generates well-localized superheating of HGNs, yielding subcellular thermal damage and cell death.

The following chapters transition to the synthesis and characterization of colloidal and solid film perovskite quantum dots (PQDs). Important hindrances for commercialization of PQD solid film in optoelectronic devices are insufficient charge transport and long-term stability. This is mostly contributed to their lack of charge transfer in PQD solid films and degradation in the presence of moisture, oxygen, heat, and light. These hindrances can be overcome by exploring different surface ligand passivation strategies and understanding their functionality associated with PQD solid

film's optical, electronic, and electrical properties. Enhancing the charge transport properties of PQDs is dependent on mitigating the tunneling barrier which is imposed by the distance charges must travel between PQDs. Using long alkyl chain passivating ligands instills greater stability, however, a diminishment in charge transport. Moreover, short alkyl chain or counter ion passivation leads to instability but improved charge transport. To overcome these inversely related properties, an effective strategy to mitigate the charge tunneling barrier and simultaneously provide stability is passivating with exciton-delocalization ligands (EDLs). EDLs consist of π delocalizing orbitals that hybridize with the electronic wave function of PQDs. This enables charges to delocalize to the PQD's surface and eliminates the tunneling barrier imposed by surface ligands. The following chapters discuss the dependence of charge transport and stability of PQD solid film on the capping ligand chain length, and then, the investigations of using EDLs for enhancing the optical and charge transport properties of PQD solid film.

The final chapter discusses the synthesis of perovskite magic sized clusters (PMSCs). Specifically, the ligand dependence of their growth and optical properties. Here, PMSCs are synthesized using an excess amount of capping ligands. The two different ligand combinations used to synthesized PMSCs are butylamine-valeric acid (BTYA-VA) and 3,3-diphenylpropylamine-valeric acid (DPPA-VA). These PMSCs were observed to have the bluest shifted absorption and PL peaks that correspond to their smallest stable size. For BTYA-VA PMSCs, the excitonic absorption peak is at 424 nm and PL peak at 434 nm, while the DPPA-VA PMSCs exhibited an absorption peak at 428 nm and PL peak at 451 nm. Due to the shift in absorption, the size of

PMSCs is determined to be ligand dependent. In addition, it was discovered that different size PQDs can be synthesized from DPPA-VA PMSCs that correspond to a specific dilution. This method to precisely tune size, and hence, optical properties simply by dilution may provide a more exact and facile synthesis of PQDs.

Acknowledgements

I would first like to acknowledge my P.I. Prof. Jin Z. Zhang for all his support, help, and training. When I first met Jin, I felt his passion for science and research. I too felt the same passion, however, it was his openness to new ideas that allowed me to thrive in his research group. When discussing a new project idea that I could potentially do in his lab if I joined, he immediately jumped on the project and gave me new ideas to help advance the project. This first project in his lab did not work out, but here I learned through dedication and constantly pushing new ideas to the test that I could achieve great success. Jin and I are very good at thinking of new ideas for projects, and together, we feed off of each other's ideas which generates limitless boundaries in our research. Moreover, Jin has provided excellent collaboration support to my research from his large tree of connections that he gained from experience and actively participating in conferences. My research would not have gained the impact as it did without access to the supplemental measurements from the collaborators. In addition, I would like to thank Jin for pushing me to write papers, improve my writing, conducting research, and learning new instrumentation. Finally, Jin is very support and encouraging of my future endeavors.

I would like to acknowledge my thesis members Prof. Scott R. J. Oliver and Prof. Yat Li for supporting me through the years. I thank them for taking the time to be a part of my committee, mentoring me throughout my PhD program, and writing letters of recommendation for my potential future jobs.

I would like to acknowledge my current lab members Vivien Cherrette and Melissa Guarino-Hotz for their support and encouragement.

I want to thank my lab members that provided me mentorship throughout the years Dr. Sara Bonabi Naghadeh, Dr. Staci A. Adams, and Dr. Sarah Lindley. They were all very supportive when I first joined the lab. Staci was a pleasure to have in the lab as she always had something to say to spark up a fun conversation. Bless her for driving more than 3 hours a day to come to work. I want to thank Staci for teaching me the hollow gold nanosphere synthesis and mentoring me in other areas in the lab. I want to thank Sarah for advising me in my projects and teaching me lab techniques. Sarah was very nice to have in lab and fun person to talk with. She taught me a lot about professionalism and conducting high quality research. I want to acknowledge Sara for being a really good friend and helping me anyway she can in my research. Sara taught me the perovskite quantum dot synthesis and provided helpful insight in this research when I switched to this different field. She made the transition a lot easier for me. I want to thank Sara for putting in the effort and contributing to my projects. Sara was a pleasure to be around in lab as she was easy to talk and relate with. We both struggled together and overcame the obstacles to become success.

I want to acknowledge my fellow cohort member and lab mate A'Lester C. Allen. We supported each other in our research and PhD milestones, and it helped me overcome these difficulties. A'Lester is a very nice guy, polite and helpful. He is fun to talk with as he is a very good listener and provides excellent feedback. A'Lester is very on top of things and did everything he could to support the lab. Also, I want to thank A'Lester for allowing me to park at his house when I fly out of San Jose.

I want to thank my undergraduates Jessica Hibbs, Ben Dreskin, and Thomas Graham. Jessica is a very smart person that helped me with the challenging hollow gold

nanosphere synthesis. I want to thank Ben and Thomas for putting in the effort and contributing significantly to important projects that defined my graduate career. Ben and Thomas became really good friends of mine. I will always treasure the special memories we had together.

I want to especially thank the “CREW” Dr. Miguel Pinto, Dr. Tianyi Kou, and Dr. Michael Roders. These guys became my best friends during my PhD career, and we share a lot of very special memories together. They really brought a lot of joy to my graduate school experience.

Finally, I would like to acknowledge my family: brother Chris Vickers, sister Emma Foens, mother Leigh Tappe, father Steven Vickers, grandmother Joyce Beeman, grandfather Ron Beeman, grandmother Carolyn Vickers, grandfather Edward Vickers, grandfather Buddy Tappe, aunt Sue Vickers, and girlfriend Jessica Gutierrez. I am grateful for their support and giving me the tools to succeed.

Dedication

I dedicate this thesis to my mother Leigh Tappe and father Steve Vickers. Thank you for raising and supporting me throughout my life. Without their care and love I would not have been where I am today.

Chapter 1. Introduction

1.1. Hollow Gold Nanospheres for Cancer Theranostics

1.1.1. Plasmonic Nanoparticles

Plasmonic nanoparticles are metal nanoparticles that possess surface plasmon resonance (SPR) optical properties.[1] Plasmons are collective oscillations of free electrons in metals. These oscillations occur at a well-defined frequency. When exposed to incident electromagnetic (EM) radiation that is on resonance with these oscillations, the EM radiation creates a coherent oscillatory response of conducting electrons, as illustrated in **Figure 1.1.1**.[2] The photons can be absorbed by the nanoparticle and transformed into heat, luminescence, or scattered light.[3,4] The SPR wavelengths that can be absorbed or scattered are dependent on the size and shape of the plasmonic nanoparticle, which effect the confinement and oscillation of the free electron cloud.[5]

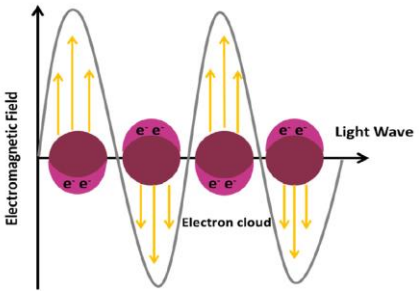

Figure 1.1.1. *Conducting electrons coherent oscillatory response incident EM radiation in resonance. Figure reproduced with permission from Coordination Chemistry Reviews 2016, 320-321, 18-37.*

1.1.2. Hollow Gold Nanospheres

Hollow gold nanospheres (HGNs) are plasmonic nanoparticles with unique shape and optical properties that are advantageous in numerous applications.[2,6,7] HGNs are comprised of a slightly porous spherical polycrystalline gold shell and a solvent filled dielectric core. An effective method for synthesizing HGNs is using a sacrificial template, cobalt nanoparticles, which are synthesized by reducing Co^{2+} using sodium borohydride, and then, through a galvanic exchange between Au^{+} and $Co_{(s)}$.[2,6-11] Here, Au^{+} is converted to $Au_{(s)}$ and $Co_{(s)}$ is converted Co^{2+} on the cobalt nanoparticle surface, and the remainder $Co_{(s)}$ is converted to Co^{2+} when exposed to air. HGN diameter and shell thickness is controlled by adjusting the temperature and injection speed of the sodium borohydride as well as the concentration of precursors. Their spherical diameter can be tuned from 20 to 125 nm and shell thickness from 3 nm to solid gold nanosphere. The aspect ratio between nanosphere diameter and shell thickness dictates their SPR peak position, which can be tuned from near solid gold nanospheres at 525< nm to ~900 nm. Larger diameter and thinner shelled HGNs exhibit red-shifted SPR corresponding to its lower energy oscillation of free electron cloud. HGNs are unique as they possess an inner core and outer core surface that enhances SPR through strong coupling and hybridization of its two individual plasmon modes as in a coupled harmonic oscillator. The strength of this coupling increases as shell thickness decreases. In addition, thinning the shell decreases the mean free path of electrons. By decreasing the mean free path of electrons by confining them in a thin shell, more electrons are consequently forced into a denser conduction band along with a more coalescing electron resonance.[12] This allows greater electron resonance to incident EM

radiation, and therefore, HGNs are observed to have higher molar extinction coefficients at peak SPR than any solid gold nanoparticle that is similar in size, shape, and mass of gold. In addition, due to the shell and solvent filled core of HGNs, there are more dynamic vibrational modes than in most solid gold nanoparticles.[13-16] Consequently, HGNs are demonstrated to have ultrafast electron-phonon coupling times. This faster and more efficient light-to-heat conversion property of HGNs is befitting of highly prospective material for photothermal therapy.

1.1.3. Photothermal Therapy

Photothermal therapy or photoablation therapy involves delivering heat to cancerous and other harmful cells using EM radiation.[17] By bring heat into the cells, there are numerous mechanisms that could occur leading to the death of the cell. Depending on exposure time, lower temperatures between 41°C and 46°C induce apoptosis, necroptosis, and necrosis.[18] Temperatures between 46°C and 60°C causes irreversible damage having higher percentage of necroptosis and necrosis, and temperatures greater than 60°C protein coagulation occurs instantly as cell death. Another mechanism is generating micro- and nanobubbles into the cell from well-confined superheating.[19] This causes mechanical damage to the cell leading to apoptosis.

The method of photothermal therapy using gold nanoparticles involves first tailoring the surface of the gold nanoparticles to selectively bind to the cancer cells.[20-23] Ligands containing lone pairs, such as amines and especially thiols bind covalently to the electron rich surface of the gold. These ligands include antibodies that are

engineering to bind specifically and strongly to antigens that are overexpressed or only present on the cancer cells or nutrients that fuel cancer cells overactive metabolism. The gold nanoparticles that are functionalized with these selectively binding ligands bind to the cancer cell surface, where depending on the metabolic mechanism, may remain on the surface or become ingested by the cell.[24] To excite the gold nanoparticles on or in the cells the light needs to be able to penetrate through the biomolecules of the cell to reach the gold nanoparticles. The biomolecules in cells absorb strongly in the UV to visible region, however, near-infrared (NIR) light in tissue transparency windows 650-950 nm and 1100-1350 nm has been demonstrated to penetrate through tissue 0-2 cm.[25,26]

1.1.4. Two-Photon Spectroscopy

Two-photon absorption is a rare event when two photons are absorbed within ~0.5 fs of each other.[27,28] The first incident photon absorbed brings the material to a virtual state and the second incident photon with the same energy excites the material again to a higher state that is quantum equivalent to double the energy of the incident photons. The probability of two-photon absorption is proportional to the intensity squared of the excited light. To achieve sufficient photon densities, pulsed lasers with high peak power density and collimated beams using numerical apertures are employed. One advantage to this excitation is that higher electronic states can be accessed through exciting with lower energy photons. This method is useful in phototherapy as NIR-tissue-penetrable light can be used to excite drug delivery material.[29,30]

1.2. Perovskite

1.2.1. Structure

The term "Perovskite" refers to the class of materials with the same structure as $CaTiO_3$ that was first reported in 1920 by Goldschmidt *et al.*[31] It was first discovered in 1839 and named after the Russian mineralogist L. A. Perovski. The structure of perovskite is generalized with the formula ABX_3, where A is a monovalent cation, B is a divalent metal cation, and X is a monovalent anion. The main contributor to the structure and properties of the perovskite is the BX_6 octahedra network that is structurally supported by the A cation.[31-34] The center of the octahedra is the B larger metal cation and X is positioned at the octahedra corners around B. A is arranged at the holes surrounding the octahedra and creates a balance charge to stabilize the whole network, as illustrated in **Figure 1.2.1**.

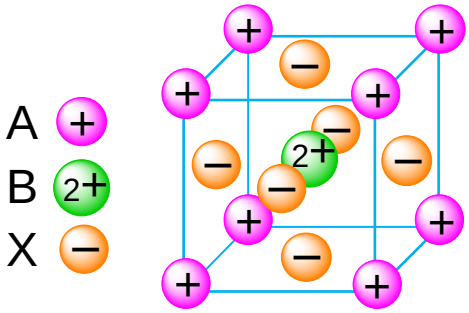

Figure 1.2.1. *The general structure of perovskite.*

1.2.2. Organic-Inorganic Metal Halide Perovskite

Organic-inorganic metal halide perovskite (OMHP) with the formula ABX_3 ($A=CH_3NH_3^+$(MA), $CH(NH_2)_2^+$(FA), Cs^+, etc.; $B=Pb^{2+}$, Sn^{2+}, etc.; $X=Cl^-$, Br^-, and I^-)

is a highly studied material over the past decade.[35-40] Their facile synthesis and low-cost enables the material to be easily studied with the prospect high output commercial manufacturing, while their extraordinary optical, electronic, and electrical properties allows exponential advancement in the efficiency of optoelectronic technology. This includes photovoltaics (PV), light-emitting diodes (LED), photodetectors, transistors, solar fuels, etc. Due to the ever-increasing global energy demands and environment impact of fossil fuel being our current major source of energy, one of the main focuses have been PV research and development. Over the past decade the power conversion efficiency (PCE) of OMHP-based PV devices have risen from 3.8% to 24.2% (reported by the U.S. National Renewable Energy Laboratory (NREL), https://www.nrel.gov/pv/assets/pdfs/pv-efficiencychart.201812171.pdf).[41] The large increase in PCE is contributed to the material's high absorption coefficient, solar spectrum overlap, large number of photogenerated charge carriers, long diffusion length of charge carriers, defect tolerance, and high photoluminescence quantum yield (PLQY) as well as flexibility in tuning their electronic and optical properties.[42-44]

1.2.3. Electronic Properties

The electronic structure of OMHP is shown in **Figure 1.2.2**. As mentioned in section 1.2.1., the BX_6 octahedra dictates the electronic properties of perovskite especially near the band edge. In the $[BX_6]^{4-}$ units, the valence band (VB) or highest occupied molecular orbital (HOMO) consists of B(5s/6s)-X(3p/4p/5p) σ-antibonding orbital and the conduction band (CB) or lowest unoccupied molecular orbital (LUMO) includes the B(5p/6p)-X(3p/4p/5p) π-antibonding and B(5p/6p)-X(3s/4s/5s) σ-

antibonding orbitals.[32] An uncommon aspect in its electronic properties is the occupied lone pair in the B(5s/6s) orbital that lies just below the top of the VB. The VB maximum has strong B(5s/6s) and X(3p/4p/5p) antibonding character, while the CB maximum is mostly contributed from B(5p/6p) orbital. This attributes to the ionic and covalent dual nature of OMHP. Moreover, the electronic structure of OMHP is unique compared to conventional semiconductors, such as in GaAs and Si-based solar cells, because the CB contains less dispersion of states from its higher density of states in its p-orbital, whereas in conventional semiconductors the CB consists of s-orbitals. This enables longer diffusion length and higher population of photogenerated charge carriers. Another advantage of OMHP is that it has a strong direct band gap which allows for a greater probability of VB and CB transitions.

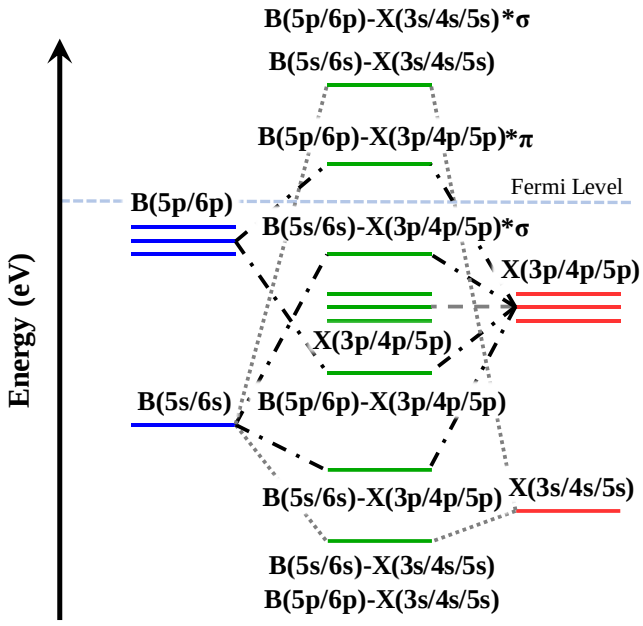

Figure 1.2.2. *The electronic structure of OHMP.*

1.3. Methylammonium Lead Bromide Perovskite Quantum Dots

1.3.1. Quantum Dots

One of the most promising materials for integrating into optoelectronic devices is semiconductor quantum dots (QDs),[45-52] which exhibit spatial quantum confinement when their dimensions are smaller than or on the order of the Bohr exciton radius.[53-55] QDs are zero dimensional compared to their bulk counterpart, and consequently, contain a limited number of electrons in discrete quantized energy levels. Hence, these nanostructured materials bridge the gap between bulk semiconductors and molecules. Semiconductor QDs exhibit quantum confinement states of their excitons. Therefore, adjusting the size of QDs shift their optical absorption and emission energies. This results in tunable and sometimes enhanced optical and electronic properties that are potentially useful for photovoltaic (PV), light-emitting diode (LED), and other applications.[56-59]

1.3.2. Methylammonium Lead Bromide Perovskite

The highest efficiency perovskite-based PV devices are mainly obtained using methylammonium lead iodide with a band gap 1.5-1.6 eV.[60-62] Its smaller band gap allows greater absorption overlap with the solar spectrum, which in turn, generates higher photocurrent. However, there are advantages using bromide-based materials. Methylammonium lead bromide perovskite has a wider band gap of 2.3 eV, and therefore, has potential for greater open-circuit voltages (V_{OC}).[63] In addition, it can be incorporated in a tandem solar cell device by adding another active layer that absorbs

in the infrared (IR) region.[64-68] Furthermore, bromide-based perovskites have been demonstrated to be significantly more stable and easier to synthesize than iodide-based ones, due to greater thermodynamic stability and lower sensitivity to superoxide.[69,70] However, even bromide-based perovskite still suffer from instability towards environmental factors, such as moisture, oxygen, heat, and light.[71,72]

One approach to overcome instability is to passivate the surface with molecular ligands that effectively remove surface defects and block infiltrating molecules that can degrade the perovskite core.[73-77] Perovskite quantum dots (PQDs) have been demonstrated to be an excellent model for this approach.[78-87] Due to the advancements in the synthesis of PQDs, PQDs achieve high PLQY (>90%) and monodispersity. In addition, PQDs have size tunable optical properties, which is especially useful for specific optoelectronic applications that occur in PV, LED, photodetectors, etc. However, due to the insulating nature of its surface passivating ligands, PQD-PQD electronic coupling, and hence, PQD solid film, lacks sufficient charge transport.

1.3.3. Charge Transport in PQD Solid Film

An important hindrance for commercialization of PQD solid film in optoelectronic devices is its lack of charge transport.[87,88] This is due to poor PQD-PQD electronic coupling. The key to high-mobility of charge carriers in PQD solid film is the emergence from carrier tunneling through localized quantum-confined states to band-like charge transport in delocalized and hybridized states derived from strong PQD-PQD electronic coupling.[89] This is strongly dictated by the interdot distance. As the distance is reduced the states transition from discrete to extended electronic state

formation from wavefunction overlap of neighboring PQDs. In addition, the dispersity in the size, shape, and composition generates inhomogeneous solid film which creates midgap trap states and widens the distribution of electronic states.

Monodispersed PQDs that have a reduced interdot distance in solid film has been previously reported to enhance charge transport, however, due to the lack of steric hindrance boundary from its small surface ligands or lack thereof, the stability of PQDs is significantly diminished.[90] Hence, when passivating the PQD surface using insulating or electronically inactive ligands there is a trade-off between enhancing the stability from long and/or large ligands and enhancing the charge transport from short and/or small ligands.

1.3.4. Exciton-Delocalizing Ligands

One approach for solving the trade-off between stability and charge transport from using different size insulating ligands is to passivate using exciton-delocalizing ligands (EDLs). EDLs delocalize charge carriers from the PQD core to its ligands.[91-100] This allows greater permeation of charge carrier/exciton wave functions into interfacial regions, facilitating charge transfer by mitigating tunneling barriers imposed by the ligand shell. The effectiveness of electronically coupling PQDs *via* the ligand shell is determined by the spatial and energetic alignment between ligand frontier molecular orbitals and the band-edge positions of the PQDs.[91-97] The ligand molecular frontier orbitals can be tuned to match the PQD band-edge positions by functionalizing the ligands with electron-donating and withdrawing groups into its charge delocalizing π-bonding system.[95-97] This alignment contributes to the PQD-ligand orbital

hybridization and reduces the confinement of excitons. Following the quantum confinement principle, the increase in charge carrier delocalization volume causes a bathochromic shift in excitonic transitions.[91-92] QD-ligand orbital hybridization also enhances the optical absorption, radiative recombination rate, and photoluminescence quantum yield (PLQY).[94,96] This may be attributed to a greater oscillator strength of the transition from an increase in the number of states involved in band-edge transitions.[92] However, if the EDL is bound to the QD core in a state that facilitates charge trapping, the strong QD-ligand electronic coupling results in an increase of non-radiative recombination.[101] Therefore, energy level alignment together with specific surface-bound states are crucial elements to resolve in order to effectively enhance PQD-PQD electronic coupling, and consequently, more efficient charge transport in PQD solid films.

1.4. Magic Sized Clusters

1.4.1. Properties

Semiconductor magic size clusters (MSCs) are ultra-small nanoparticles that have a narrow size distribution and strong quantum confinement.[102] MSCs represent the molecular limit for which the smallest stable nanoparticle exists relative to its QD form. These discretely sized nanoclusters are usually smaller than 2 nm and have sharp absorption and photoluminescence (PL) peaks due to their molecule-like properties.[103-106] MSCs exhibit optical properties that are significantly blue shifted with respect to their bulk optical properties and reflect the structure approaching unit cell limit of the

material's lattice.[86] MSCs are the smallest building blocks for forming larger nanostructures such as nanocrystals (NCs) or quantum dots (QDs), and exhibit intriguing optical and physical properties for studying nanostructure growth and fundamental properties of well-defined nanostructures.

1.4.2. Synthesis and Characterization

The synthesis of MSCs involves the same or similar method for synthesizing QDs.[77,78,102,104,107,108] However, due to stability issues and other parameters such as temperature, solubility, ligand binding strength, acid-base chemistry, and ligand steric hindrance, MSC synthesis is more complex. However, our lab has contributed to the MSC synthesis using diverse approaches. To synthesize MSCs one must minimize to a significant measure the growth after nucleation. One way to accomplish this is to use an excess concentration of capping ligands. Our lab has previously reported that this method is an effective route for successful MSC synthesis. However, the quality of the ligand is also an important factor for synthesizing different sizes of MSCs as well as dictating its success. The size and steric arrangement of the ligand has been shown to affect the size and growth of the MSCs. In addition, the strength of the ionic bond between the terminal functional group of the ligand and the site of passivation on the cluster determines the success of the reaction. For the co-passivation method, using ammonium and carboxylate functional groups for anchoring onto the cluster, the success of the MSC synthesis is determined by the strength of the amine base and carboxylic acid. Due to the instability and thermodynamically unfavorable reaction, strong ionic bonding promotes more stable, uniformed, and smaller MSCs.

The characterization of MSCs has been limited to optical spectroscopy methods as its instability, ultra-small size and lack of crystal structure prevents atomic scale characterization, such as high-resolution transmission (HRTEM) spectroscopy, X-ray diffraction (XRD) spectroscopy, mass spectrometry, etc. However, UV-vis and photoluminescence (PL) spectroscopy provides clues to its structure. MSCs have distinctive narrow optical bandwidths due to their narrow or single size distribution and molecular-like properties. In contrast, QDs typically have smooth and broad absorption spectral signatures indicative of their higher density of states, whereas MSCs resemble molecules with very discrete states.

1.5. References

(1) Yu, H., Peng, Y., Yang, Y. *et al.* Plasmon-enhanced light–matter interactions and applications. *npj Comput. Mater.* **2019**, *5*, 45.

(2) Adams, S.; Zhang, J. Z. Unique Optical Properties and Applications of Hollow Gold Nanospheres. *Coord. Chem. Rev.* **2016**, *320-321*, 18-37.

(3) Zhang, T., Lu, G., Shen, H. *et al.* Photoluminescence of a single complex plasmonic nanoparticle. *Sci Rep* **2015**, ***4,*** 3867.

(4) Kim, M.; Lee, J.-H.; Nam, J.-M. Plasmonic Photothermal Nanoparticles for Biomedical Applications. *Adv. Sci.* **2019**, *6*, 1900471.

(5) Agrawal, A.; Kriegel, I.; Milliron, D. J. Shape-Dependent Field Enhancement and Plasmon Resonance of Oxide Nanocrystals. *J. Phys. Chem. C* **2015**, *119*, 6227-6238.

(6) Ren, Q.-Q.; Bai, L.-Y.; Zhang, X.-S.; Ma, Z.-Y.; Liu, B.; Zhao, Y.-D.; Cao, Y.-C. Preparation, Modification, and Application of Hollow Gold Nanospheres. *J. Nanomater.* **2015**, *2015*, 534070.

(7) Biomedical Applications of Shape-Controlled Plasmonic Nanostructures: A Case Study of Hollow Gold Nanospheres for Photothermal Ablation Therapy of Cancer. *J. Phys. Chem. Lett.* **2010**, *1*, 686-695.

(8) Lindley, S. A.; Cooper, J. K.; Rojas-Andrade, M. D.; Fung, V.; Leahy, C. J.; Chen, S.; Zhang, J. Z. Highly Tunable Hollow Gold Nanospheres: Gaining Size Control and Uniform Galvanic Exchange of Sacrificial Cobalt Boride Scaffolds. *ACS Appl. Mater. Interfaces* **2018**, *10*, 12992-13001.

(9) Adams, S.; Thai, D.; Mascona, X.; Schwartzberg, A. M.; Zhang, J. Z. Key Factors Affecting the Reproducibility of Synthesis and Growth Mechanism of Near-Infrared Absorbing Hollow Gold Nanospheres. *Chem. Mater.* **2014**, *26*, 6805-6810.

(10) Adams, S.; Thai, D.; Mascona, X.; Schwartzberg, A. M.; Zhang, J. Z. Key Factors Affecting the Reproducibility of Synthesis and Growth Mechanism of Near-Infrared Absorbing Hollow Gold Nanospheres. *Chem. Mater.* **2014**, *26*, 6805-6810.

(11) Schwartzberg, A. M.; Olson, T. Y.; Talley, C. E.; Zhang, J. Z. Synthesis, Characterization, and Tunable Optical Properties of Hollow Gold Nanospheres. *J. Phys. Chem. B* **2006**, *110*, 19935-19944.

(12) Wheeler, D.; Newhouse, R.; Wang, H.; Zou, S.; Zhang, J. Z. Optical Properties and Persistent Spectral Hole-Burning of Near Infrared-Absorbing Hollow Gold Nanospheres. *J. Phys. Chem. C* **2010**, *114*, 18126−18133.

(13) Dowgiallo, A.-M.; Knappenberger Jr., K. L. Ultrafast Electron-Phonon Coupling in Hollow Gold Nanospheres. *Phys. Chem. Chem. Phys.* **2011**, *13*, 21585-21592.

(14) Fan, Y.; Li, J.; Chen, H.; Lu, X.; Liu, X. Size-Dependence of the Effective Electron-Phonon Energy Relaxation in Hollow Gold Nanospheres. *Opto-Electron Rev.* **2006**, *22*, 36-40.

(15) Newhouse, R. J.; Wang, H.; Hensel, J. K.; Wheeler, D. A.; Zou, S.; Zhang, J. Z. Coherent Vibrational Oscillations of Hollow Gold Nanospheres. *J. Phys. Chem. Lett.* **2011**, *2*, 228-235.

(16) Dowgiallo, A.-M.; Schwartzberg, A. M.; Knappenberger Jr., K. L. Structure-Dependent Coherent Acoustic Vibrations of Hollow Gold Nanospheres. *Nano Lett.* **2011**, *11*, 3258-3262.

(17) Vines, J. B.; Yoon, J.-H.; Ryu, N.-E.; Lim, D.-J.; Park, H. Gold Nanoparticles for Photothermal Cancer Therapy. *Front. Chem.* **2019**, *7*, 167.

(18) Zhang, Y.; Zhan, X.; Xiong, J.; Peng, S.; Huang, W.; Joshi, R.; Cai, Y.; Liu, Y.; Li, R.; Yuan, K.; Zhou, N.; Min, W. Temperature-Dependent Cell Death Patterns Induced by Functionalized Gold Nanoparticle Photothermal Therapy in Melanoma Cells. *Sci. Rep.* **2018**, *8*, 8720.

(19) Kotaidis, V.; Plech, A. Cavitation Dynamics on the Nanoscale. *Appl. Phys. Lett.* **2005**, *87*, 213102.

(20) Singh, P.; Pandit, S.; Mokkapati, V.R.S.S.; Garg, A.; Ravikumar, V.; Mijakovic, I. Gold Nanoparticles in Diagnostic and Therapeutics for Human Cancer. *Int. J. Mol. Sci.* **2018**, *19*, 1979.

(21) Jazayeri, M. H.; Amani, H.; Pourfatollah, A. A.; Pazoki-Toroudi, H.; Sedighimoghaddam, B. Various Methods of Gold Nanoparticles (GNPs) Conjugation to Antibodies. *Sens. Biosensing Res.* **2016**, *9*, 17-22.

(22) Friedman, A. D.; Claypool, S. E.; Liu, R. The Smart Targeting of Nanoparticles. *Curr. Pharm. Des.* **2013**, *19*, 6315-6329.

(23) Liu, S.; Lämmerhofer, M. Functionalized Gold Nanoparticles for Sample Preparation: A Review. *Electrophoresis* **2019**, *40*, 2438-2461.

(24) Wang, Y.-P.; Lei, Q.-Y. Metabolite Sensing and Signaling in Cell Metabolism. *Signal Transduct. Tar.* **2018**, *3*, 30.

(25) Pastrana, E. Near-Infrared Probes. *Nat. Methods* **2013**, *10*, 36.

(26) Golovynskyi, S.; Golovynska, I.; Stepanova, L. I.; Datsenko, O. I.; Liu, L.; Qu, J.; Ohulchanskyy, T. Y. Optical Windows for Head Tissues in Near-Infrared and Short-Wave Infrared Regions: Approaching Transcranial Light Applications. *J. Biophotonics* **2018**, *11*, e201800141.

(27) Rumi, M.; Perry, J. W. Two-Photon Absorption: An Overview of Measurements and Principles. *Adv. Opt. Photonics* **2010**, *2*, 451-518.

(28) Olesiak-Banska, J.; Waszkielewicz, M.; Obstarczyk, P.; Samoc, M. Two-Photon Absorption and Photoluminescence of Colloidal Gold Nanoparticles and Nanoclusters. *Chem. Soc. Rev.* **2019**, *48*, 4087-4117.

(29) Croissant, J.; Chaix, A.; Mongin, O.; Wang, M.; Clément, S.; Raehm, L.; Durand, J.-O.; Hugues, V.; Blanchard-Desce, M.; Maynadier M. *et al.* Two-Photon-Triggered Drug Delivery via Fluorescent Nanovalves. *Small* **2014**, *10*, 1752-1755.

(30) Shen, Y.; Shuhendler, A. J.; Ye, D.; Xu, J. J.; Chen, H. Y. Two-Photon Excitation Nanoparticles for Photodynamic Therapy. *Chem. Soc. Rev.* **2016**, *45*, 6725-6741.

(31) Cheng, Z.; Lin, J. Layered Organic-Inorganic Hybrid Perovskites: Structure, Optical Properties, Film Preparation, Patterning and Templating Engineering. *CrystEngComm* **2010**, *12*, 2646-2662.

(32) Elumalai, N. K.; Mahmud, M. A.; Wang, D.; Uddin, A. Perovskite Solar Cells: Progress and Advancements. *Energies* **2016,** *9*, 861.

(33) Zhao, Y.; Zhu, K. Organic-Inorganic Hybrid Lead Halide Perovskite for Optoelectronic and Electronic Applications. *Chem. Soc. Rev.* **2016**, *45*, 655.

(34) Walsh, A. Principles of Chemical Bonding and Band Gap Engineering in Hybrid Organic-Inorganic Halide Perovskites. *J. Phys. Chem. C* **2015**, *119*, 5755-5760.

(35) Snaith, H. J. Present Status and Future Prospects of Perovskite Photovoltaics. *Nat. Mater.* **2018**, *17*, 372−376.

(36) Shi, Z.; Jayatissa, A. H. Perovskite-Based Solar Cells: A Review of Recent Progress, Materials and Processing Methods. *Materials* **2018**, *11*, 729.

(37) Kamat, P. V. Quantum Dot Solar Cells. The Next Big Thing in Photovoltaics. *J. Phys. Chem. Lett.* **2013**, *4*, 908−918.

(38) Carey, G. H.; Abdelhady, A. L.; Ning, Z.; Thon, S. M.; Bakr, O. M.; Sargent, E. H. Colloidal Quantum Dot Solar Cells. *Chem. Rev.* **2015**, *115*, 12732−12763.

(39) Sogabe, T.; Shen, Q.; Yamaguchi, K. Recent Progress on Quantum Dot Solar Cells: A Review. *J. Photonics Energy* **2016**, *6*, 040901.

(40) Pan, J.; Shang, Y.; Yin, J.; De Bastiani, M.; Peng, W.; Dursun, I.; Sinatra, L.; El-Zohry, A. M.; Hedhili, M. N.; Emwas, A.-H.; Mohammed, O. F.; Ning, Z.; Bakr,

O. M. Bidentate Ligand-Passivated $CsPbI_3$ Perovskite Nanocrystals for Stable Near-Unity Photoluminescence Quantum Yield and Efficient Red Light-Emitting Diodes. *J. Am. Chem. Soc.* **2018**, *140*, 562-565.

(41) Jena, A. K.; Kulkarni, A.; Miyasaka, T. Halide Perovskite Photovoltaics; Background, Status, and Future Prospects. *Chem. Rev.* **2019**, *119*, 3036-3103.

(42) Huang, H.; Bodnarchuk, M. I.; Kershaw, S. V.; Kovalenko, M. V.; Rogach, A. L. Lead Halide Perovskite Nanocrystals in the Research Spotlight: Stability and Defect Tolerance. *ACS Energy Lett.* **2017**, *2*, 2071-2083.

(43) Xiang, W.; Tress, W. Review on Recent Progress of All-Inorganic Metal Halide Perovskites and Solar Cells. *Adv. Mater.* **2019**, *31*, 1902851.

(44) Stranks, S. D.; Snaith, H. J. Metal-Halide Perovskites for Photovoltaics and Light-Emitting Devices. *Nat. Nanotechnol.* **2015**, *10*, 391-402.

(45) Kamat, P. V. Quantum Dot Solar Cells. Semiconductor Nanocrystals as Light Harvesters. *J. Phys. Chem. C* **2008**, *112*, 18737-18753.

(46) Lan, X.; Voznyy, O.; García de Arquer, F. P.; Liu, M.; Xu, J.; Proppe, A. H.; Walters, G.; Fam, F.; Tan, H.; Liu, M.; *et al.* 10.6% Certified Colloidal Quantum Dot Solar Cells via Solvent-Polarity-Engineered Halide Passivation. *Nano Lett.* **2016**, *16*, 4630-4634.

(47) Yang, Z.; Fan, J. Z.; Proppe, A. H.; García de Arquer, F. P.; Rossouw, D.; Voznyy, O.; Lan, X.; Liu, M.; Walters, G.; Quintero-Bermudez, R.; *et al.* Mixed-quantum-dot Solar Cells. *Nat. Commun.* **2017**, *8*, 1325.

(48) Pan, Z.; Rao, H.; Mora-Seró, I.; Bisquert, J.; Zhong, X. Quantum Dot-Sensitized Solar Cells. *Chem. Soc. Rev.* **2018**, *47*, 7659.

(49) Liu, C.; Hu, M.; Zhou, X.; Wu, J.; Zhang, L.; Kong, W.; Li, X.; Zhao, X.; Dai, S.; Xu, B.; et al. Efficiency and Stability Enhancement of Perovskite Solar Cells by Introducing $CsPbI_3$ Quantum Dots as an Interface Engineering Layer. *NPG Asia Materials* **2018**, *10*, 552-561.

(50) Karani, A.; Yang, L.; Bai, S.; Futscher, M. H.; Snaith, H. J.; Ehrler, B.; Greenham, N. C.; Di, D. Perovskite/Colloidal Quantum Dot Tandem Solar Cells: Theoretical Modeling and Monolithic Structure. *ACS Energy Lett.* **2018**, *3*, 869-874.

(51) Thulasivarma Chebrolu, V.; Kim, H.-J. Recent Progress in Quantum Dot Sensitized Solar Cells: An Inclusive Review of Photoanode, Sensitizer, Electrolyte, and the Counter Electrode. *J. Mater. Chem. C* **2019**, *7*, 4911-4933.

(52) Brus, L. E. Electron–electron and Electron-hole Interactions in Small Semiconductor Crystallites: The Size Dependence of the Lowest Excited Electronic State. *J. Chem. Phys.* **1984**, *80*, 4403-4409.

(53) Ekimov, A. I.; Efros, A. L.; Onushchenko, A. A. Quantum Size Effect in Semiconductor Microcrystals. *Solid State Commun.* **1985**, *56*, 921-924.

(54) Weller, H. Quantized Semiconductor Particles: A Novel State of Matter for Materials Science. *Adv. Mater.* **1993**, *5*, 88–95.

(55) Park, N.-G. Perovskite Solar Cells: An Emerging Photovoltaic Technology. *Mater. Today* **2015**, *18*, 65-72.

(56) Liu, F.; Zhang, Y.; Ding, C.; Kobayashi, S.; Izuishi, T.; Nakazawa, N.; Toyoda, S.; Ohta, T.; Hayase, S.; Minemoto, T. et al. Highly Luminescent Phase-Stable $CsPbI_3$ Perovskite Quantum Dots Achieving Near 100% Absolute Photoluminescence Quantum Yield. *ACS Nano* **2017**, *11*, 10373-10383.

(57) Maes, J.; Balcaen, L.; Drijvers, E.; Zhao, Q.; De Roo, J.; Vantomme, A.; Vanhaecke, F.; Geiregat, P.; Hens, Z. Light Absorption Coefficient of $CsPbBr_3$ Perovskite Nanocrystals. *J. Phys. Chem. Lett.* **2018**, *9*, 3093-3097.

(58) Kong, X.; Zong, K.; Lee, S. S. Nanoconfining Optoelectronic Materials for Enhanced Performance and Stability. *Chem. Mater.* **2019**, *31*, 4953-4970.

(59) Y. Zhao, H. Tan, H. Yuan, Z. Yang, J. Z. Fan, J. Kim, O. Voznyy, X. Gong, L. N. Quan, C. S. Tan, J. Hofkens, D. Yu, Q. Zhao, E. H. Sargent, Perovskite seeding growth of formamidinium-lead-iodide-based perovskites for efficient and stable solar cells. *Nat. Comm.* **2018**, *9*, 1607.

(60) L. Gil-Escrig, A. Miquel-Sempere, M. Sessolo, H. J. Bolink, Mixed iodide-bromide methylammonium lead perovskite-based diodes for light emission and photovoltaics. *J. Phys. Chem. Lett.* **2015**, *6*, 3743-3738.

(61) C. Momblona, O. Malinkiewicz, C. Rold´an-Carmona, A. Soriano, L. Gil-Escrig, E. Bandiello, M. Scheepers, E. Edri, H. J. Bolink, Efficient methylammonium lead iodide perovskite solar cells with active layers from 300 to 900 nm. *APL Mater.* **2014**, *2*, 081504.

(62) R. Sheng, A. Ho-Baillie, S. Huang, S. Chen, X. Wen, X. Hao, M. Green, Methylammonium lead bromide perovskite-based solar cells by vapor-assisted deposition. *J. Phys. Chem. C* **2015**, *119*, 3545-3549.

(63) Z. Song, C. Chen, C. Li, R. A. Awni, D. Zhao, Y. Yan, Wide-bandgap, low-bandgap, and tandem perovskite solar cells. *Semicond. Sci. Technol.* **2019**, *34*, 093001.

(64) Q. Wali, N. Kumar Elumalai, Y. Iqbal, A. Uddin, R. Jose, Tandem perovskite solar cells. *Renew. Sust. Energ. Rev.* **2018**, *84*, 89-110.

(65) J.-W. Lee, Y.-T. Hsieh, N. De Marco, S.-H. Bae, Q. Han, Y. Yang, Halide perovskite for tandem solar cells. *J. Phys. Chem. Lett.* **2017**, *8*, 1999-2011.

(66) P. P. Boix, S. Agarwala, T. M. Koh, N. Mathews, S. G. Mhaisalkar, Perovskite solar cells: beyond methylammonium lead iodide. *J. Phys. Chem. Lett.* **2015**, *6*, 898-907.

(67) J. H. Heo, S. H. Im, $CH_3NH_3PbBr_3$-$CH_3NH_3PbI_3$ perovskite-perovskite tandem solar cells with exceeding 2.2 V open circuit voltage. *Adv. Mater.* **2016**, *28*, 5121-5125.

(68) M. Faghihnasiri, M. Izadifard, M. Ebrahim Ghazi, DFT study of mechanical properties and stability of cubic methylammonium lead halide perovskite ($CH_3NH_3PbX_3$, X = I, Br, Cl). *J. Phys. Chem. C* **2017**, *121*, 27059-27070.

(69) S. Pont, D. Bryant, C.-T. Lin, N. Aristidou, S. Wheeler, X. Ma, R. Godin, S. A. Haque, J. R. Durrant, Tuning $CH_3NH_3Pb(I_{1-x}Br_x)_3$ perovskite oxygen stability in thin films and solar cells. *J. Mater. Chem. A* **2017**, *5*, 9553-9560.

(70) T. T. Ava, A. Al Mamun, S. Marsillac, G. Namkoong, A review: Thermal stability of methylammonium lead halide-based perovskite solar cells. *Appl. Sci.* **2019**, *9*, 188.

(71) B. Brunetti, C. Cavallo, A. Ciccioli, G. Gigli, A. Latini, On the thermal and thermodynamic (In)stability of methylammonium lead halide perovskites. *Sci. Rep.* **2016**, *6*, 31896.

(72) C. Aranda, A. Guerrero, J. Bisquert, Ionic effect enhances light emission and the photovoltage of methylammonium lead bromide perovskite solar cells by reduced surface recombination. *ACS Energy Lett.* **2019,** *4*, 741-746.

(73) B. Li, Y. Zhang, L. Fu, T. Yu, S. Zhou, L. Zhang, L. Yin, Surface passivation engineering strategy to fully-inorganic cubic $CsPbI_3$ perovskites for high-performance solar cells. *Nat. Comm.* **2018**, *9*, 1076.

(74) P. Zhao, B. J. Kim, H. S. Jung, Passivation in perovskite solar cells: A review. *Mater. Today Energy* **2018**, *7*, 267-286.

(75) Y. Zhou, F. Wang, Y. Cao, J.-P. Wang, H.-H. Fang, M. A. Loi, N. Zhao, C.-P. Wong, Benzylamine-treated wide-bandgap perovskite with high thermal-photostability and photovoltaic performance. *Adv. Energy Mater.* **2017**, *7*, 1701048.

(76) F. Wang, W. Geng, Y. Zhou, H.-H. Fang, C.-J. Tong, M. A. Loi, L.M. Liu, N. Zhao, Phenylalkylamine passivation of organolead halide perovskite enabling high-efficiency and air-stable photovoltaic cells. *Adv. Mater.* **2016**, *28*, 9986-9992.

(77) K. Xu, A. C. Allen, B. Luo, E. T. Vickers, Q. Wang, W. Hollingsworth, A. L. Ayzner, X. Li, and J. Z. Zhang, Tuning from quantum dots to magic sized clusters of $CsPbBr_3$ using novel planar ligands based on trivalent nitrate coordination complex. *J. Phys. Chem. Lett.* **2019,** 10, 4409-4416.

(78) E. T. Vickers, K. Xu, B. W. Dreskin, T. A. Graham, X. Li, J. Z. Zhang, Ligand dependent growth and optical properties of hybrid organo-metal halide perovskite magic sized clusters. *J. Phys. Chem C* **2019**, *123*, 18746-18752.

(79) J. Z. Zhang, A "Cocktail" approach to effective surface passivation of multiple surface defects of metal halide perovskites using a combination of ligands. *J. Phys. Chem. Lett.* **2019**, *10*, 5055-5063.

(80) S. Bonabi Naghadeh, B. Luo, Y.-C. Pu, Z. Schwartz, W. Hollingsworth, S. Lindley, A. Brewer, A. Ayzner, J. Z. Zhang, Size dependence of charge carrier dynamic in organometal halide perovskite nanocrystals: Deciphering the radiative vs non-radiative components. *J. Phys. Chem. C* **2019**, *123*, 4610-4619.

(81) E. T. Vickers, T. A. Graham, A. H. Chowdhury, B. Bahrami, B. W. Dreskin, S. Lindley, S. Bonabi Naghadeh, Q. Qiao, J. Z. Zhang, Improving charge carrier delocalization in perovskite quantum dots by surface passivation with conductive aromatic ligands. *ACS Energy Lett.* **2018**, *3*, 2931–2939.

(82) S. Bonabi Naghadeh, B. Luo, G. Abdelmageed, Y.-C. Pu, C. Zhang, J. Z. Zhang, Photophysical properties and improved stability of organic-inorganic perovskite by surface passivation. *J. Phys. Chem C* **2018**, *122*, 15799–15818.

(83) B. Luo, S. Bonabi Naghadeh, A. Allen, X. Li, J. Z. Zhang, Peptide-passivated lead halide perovskite nanocrystals based on synergistic effect between amino and carboxylic functional groups. *Adv. Functional Mater.* **2017**, *27*, 1604018.

(84) F. Krieg, S. T. Ochsenbein, S. Yakunin, S. ten Brinck, P. Aellen, A. Süess, B. Clerc, D. Guggisberg, O. Nazarenko, Y. Shynkarenko, S. Kumar, C.-J. Shih, I. Infante, M. V. Kovalenko, Colloidal $CsPbX_3$ (X = Cl, Br, I) nanocrystals 2.0: Zwitterionic capping ligands for improved durability and stability. *ACS Energy Lett.* **2018**, *3*, 641-646.

(85) S. A. Veldhuis, Y. K. E. Tay, A. Bruno, S. S. H. Dintakurti, S. Bhaumik, S. K. Muduli, M. Li, N. Mathews, T. C. Sum, S. G. Mhaisalkar, Benzyl alcohol-treated $CH_3NH_3PbBr_3$ nanocrystals exhibiting high luminescence, stability, and ultralow amplified spontaneous emission thresholds. *Nano Lett.* **2017**, *17*, 7424-7432.

(86) L. Peng, A. Dutta, R. Xie, W. Yang, N. Pradhan, Dot-wire-platelet-cube: Step growth and structural transformation in $CsPbBr_3$ perovskite nanocrystals. *ACS Energy Lett.* **2018**, *3*, 2014-2020.

(87) Talapin, D. V.; Lee, J.-S.; Kovalenko, M. V.; Shevchenko, E. V. Prospects of Colloidal Nanocrystals for Electronic and Optoelectronic Applications. *Chem Rev.* **2010**, *110*, 389-458.

(88) Zolfaghari, Z.; Hassanabadi, E.; Pitarch-Tena, D.; Joon Yoon, S.; Shariatinia, Z.; van de Lagemaat, J.; Luther, J. M.; Mora-Séro, I. Operation Mechanism of Perovskite Quantum Dot Solar Cells Probed by Impedance Spectroscopy. *ACS Energy Lett.* **2019**, *4*, 251-258.

(89) Kagan, C. R.; Murray, C. B. Charge Transport in Strongly Coupled Quantum Dot Solids. *Nat. Nanotechnol.* **2015**, *11*, 1013-1026.

(90) Lan, X.; Chen, M.; Hudson, M. H.; Kamysbayev, V.; Wang, Y.; Guyot-Sionnest, P.; Talapin, D. V. Quantum Dot Solids Showing State-Resolved Band-Like Transport. *Nat. Mater.* **2020**, *19*, 323-329.

(91) Frederick, M. T.; Weiss, E. A. Relaxation of Exciton Confinement in CdSe Quantum Dots by Modification with a Conjugated Dithiocarbamate Ligand. *ACS Nano* **2010**, *4*, 3195−3200.

(92) Frederick, M. T.; Amin, V. A.; Weiss, E. A. Optical Properties of Strongly Coupled Quantum Dot-Ligand Systems. *J. Phys. Chem. Lett.* **2013**, *4*, 634−640.

(93) Liu, I.-S.; Lo, H.-H.; Chien, C.-T.; Lin, Y.-Y.; Chen, C.-W.; Chen, Y.-F.; Su, W.-F.; Liou, S.-C. Enhancing Photoluminescence Quenching and Photoelectric Properties of CdSe Quantum Dots with Hole Accepting Ligands. *J. Mater. Chem.* **2008**, *18*, 675−682.

(94) Jin, S.; Harris, R. D.; Lau, B.; Aruda, K. O.; Amin, V. A.; Weiss, E. A. Enhanced Rate of Radiative Decay in CdSe Quantum Dots upon Adsorption of an Exciton-Delocalizing Ligand. *Nano Lett.* **2014**, *14*, 5323−5328.

(95) Kroupa, D. M.; Vörös, M.; Brawand, N. P.; McNichols, B. W.; Miller, E. M.; Gu, J.; Nozik, A. J.; Sellinger, A.; Galli, G.; Beard, M. C. Tuning Colloidal Quantum Dot Band Edge Positions through Solution-Phase Surface Chemistry Modification. *Nat. Commun.* **2017**, *8*, 15257.

(96) Kroupa, D. M.; Vörös, M.; Brawand, N. P.; Bronstein, N.; McNichols, B. W.; Castaneda, C. V.; Nozik, A. J.; Sellinger, A.; Galli, G.; Beard, M. C. Optical Absorbance Enhancement in PbS QD/Cinnamate Ligand Complexes. *J. Phys. Chem. Lett.* **2018**, *9*, 3425−3433.

(97) Bronstein, N. D.; Martinez, M. S.; Kroupa, D. M.; Vörös, M.; Lu, H.; Brawand, N. P.; Nozik, A. J.; Sellinger, A.; Galli, G.; Beard, M. C. Designing Janus Ligand Shells on PbS Quantum Dots using Ligand-Ligand Cooperativity. *ACS Nano* **2019**, *13*, 3839−3846.

(98) Harris, R. D.; Amin, V. A.; Lau, B.; Weiss, E. A. Role of Interligand Coupling in Determining the Interfacial Electronic Structure of Collodial CdS Quantum Dots. *ACS Nano* **2016**, *10*, 1395-1403.

(99) Lian, S. Weinberg, D. J.; Harris, R. D.; Kodaimati, M. S.; Weiss, E. A. Subpicosecond Photoinduced Hole Transfer from a CdS Quantum Dot to a Molecular Acceptor Bound Through an Exciton-Delocalizing Ligand. *ACS Nano* **2016,** *10*, 6372-6382.

(100) Westmoreland, D. E.; López-Arteaga, R.; Weiss, E. A. N-Heterocyclic Carbenes as Reversible Exciton-Delocalizing Ligands for Photoluminescence Quantum Dots. *J. Am. Chem. Soc.* **2020**, *142*, 2690-2696.

(101) Azzaro, M. S.; Babin, M. C.; Stauffer, S. K.; Henkelman, G.; Roberts, S. T. Can Exciton-Delocalizing Ligands Facilitate Hot Hole Transfer from Semiconductor Nanocrystals? *J. Phys. Chem. C* **2016**, *120*, 28224−28234.

(102) Harrell, S. M.; McBride, J. R.; Rosenthal, S. J. Synthesis of Ultrasmall and Magic-Sized CdSe Nanocrystals. *Chem. Mater.* **2013**, *25*, 1199−1210.

(103) Evans, C. M.; Guo, L.; Peterson, J. J.; Maccagnano-Zacher, S.; Krauss, T. D. Ultrabright PbSe Magic-Sized Clusters. *Nano Lett.* **2008**, *8*, 2896−2899.

(104) Ning, J.; Banin, U. Magic Size InP and InAs Clusters: Synthesis, Characterization and Shell Growth. *Chem. Commun.* **2017**, *53*, 2626.

(105) Zhang, B.; Zhu, T.; Ou, M.; Rowell, N.; Fan, H.; Han, J.; Tan, L.; Dove, M. T.; Ren, Y.; Zuo, X.; *et al.* Thermally-Induced Reversible Structural Isomerization in Collodial Semiconductor CdS Magic-Sized Clusters. *Nat. Commun.* **2018**, *9*, 2499.

(106) Zhu, D.; Hui, J.; Rowell, N.; Liu, Y.; Chen, Q. Y.; Steegemans, T.; Fan, H.; Zhang, M.; Yu, K. Interpreting the Ultraviolet Absorption in the Spectrum of 415 nm-Bandgap CdSe Magic-Size Clusters. *J. Phys. Chem. Lett.* **2018**, *9*, 2818−2824.

(107) Xu, K.; Vickers, E. T.; Luo, B.; Allen, A. C.; Chen, E.; Roseman, G.; Wang, Q.; Kliger, D. S.; Millauser, G. L.; Yang, W.; Li, X.; Zhang, J. Z. First Synthesis of Mn-Doped Cesium Lead Bromide Perovskite Magic Sized Clusters at Room Temperature. *J. Phys. Chem. Lett.* **2020**, *11*, 1162-1169.

(108) Xu, K.; Vickers, E. T.; Luo, B.; Wang, H.; Cherrette, V.; Li, X.; Zhang, J. Z. Room Temperature Synthesis of Cesium Lead Bromide Perovskite Magic Sized Clusters with Controlled Ratio of Carboxylic Acid and Benzylamine Capping Ligands. *Sol. Energy Mater. Sol. Cells* **2019**, *208*, 110341.

Chapter 2. Two-Photon Photoluminescence and Photothermal Properties of Hollow Gold Nanospheres for Efficient Theranostic Applications

2.1. Abstract

The ability to successfully pinpoint and subsequently destroy cancer cells using biologically inert material and non-invasive methods is ideal for low-risk procedures. One way to accomplish this is using plasmonic gold nanoparticles, which have two-photon photoluminescence (2PPL) and photothermal properties that can be triggered by deep-tissue-penetrable near-infrared (NIR) light (650-950 nm). Herein, the first 2PPL of hollow gold nanospheres (HGNs) is reported using multiphoton luminescence microscopy. The two-photon action cross-section of the HGNs, using gold nanorods (GNRs) as a reference, is 1.02×10^6 GM at 820 nm. Additionally, the HGNs have ~0.75 times the 2PPL quantum yield of GNRs. The larger two-photon action cross-section and lower quantum yield corresponds to a higher efficiency for heat generation desired for photothermal conversion applications. To this end, the 2PPL and photothermal properties of HGNs can be applied towards simultaneous cancer cell imaging and photothermal therapy (PTT). HGNs bioconjugated with folic acid-PEG-thiol (HGN-FA) selectively binds to overexpressed folate receptor of cervical cancer HeLa cells and the 2PPL from HGN-FA captures high resolution cancer cell images. Subsequent power increase and laser scanning dwell time results in highly efficient photothermal destruction of cancer cells. Using femtosecond laser pulses, microseconds of laser

exposure generates well-localized superheating of HGNs, yielding subcellular thermal damage and cell death.

2.2. Introduction

Photoluminescence from bulk gold was first reported in 1969 by Mooradian.[1] The origin of emission was attributed to radiative recombination due to transition of holes from the upper *d* band states to energy levels at or above the Fermi energy in the conduction band. To demonstrate that the observed emission was not due to Raman scattering, several different excitation wavelengths were used, and the same peak of emission energy resulted. Since then, innovative noble metal nanostructures with optical properties tunable for biosensing, bioimaging, and phototherapy have been exploited.[2] Gold nanoparticles have emerged as a central focus in diagnostic and therapeutic biomedical applications due to their inertness in biological systems and tunable light absorption properties.[3] Generally, gold nanoparticles have been used as contrasting agents in X-ray imaging applications of cancer, however, most recent investigations have discovered two-photon photoluminescence (2PPL) from gold nanoparticles for nonlinear bioimaging applications.[4,5] In nonlinear bioimaging applications, conventional organic dyes have poor photostability along with relatively small two-photon absorption cross-sections (1-100 GM) (GM = 10^{-50} cm^4 s/photon), while semiconductor quantum dots (QDs) are hindered by their photoblinking behavior and high cytoxicity.[6] To overcome these limitations, attention has been brought to the strong 2PPL of a variety of gold nanoparticles such as gold nanospheres,[7] gold nanoshells,[8] gold nanocages,[9] and gold nanorods (GNRs).[10] GNRs have been the

forefront in this research due to its large two-photon action cross-section ~4.2×10^4 GM.11 GNR's large two-photon action cross-section can be explained by the "lightning rod effect" and localized SPR (surface plasmon resonance) modes.[12,13] Consequently, GNRs have been utilized in several two-photon imaging applications.[10,14-17] In addition, GNRs have been used for photothermal therapy (PTT) of cancer by means of two-photon excitation microscopy.[16,17]

The challenges of using light as a tool for diagnosis and therapy of cancer are poor tissue penetration (0-2 cm), high noise from tissue scattering in the visible light region, tissue auto-fluorescence as well as light absorption by proteins, heme groups, and water.[18-20] To address these challenges, biocompatible fluorescent probes absorbing in the NIR tissue transparency windows (650-950 nm) and (1,100-1,350 nm) must be employed to minimize light scattering and absorption from tissue for maximum penetration.[21] Furthermore, fs laser pulsing of NIR light increases penetration depth by delivering high power density into tissue with troughs of energy.[22] Key advantages of using NIR pulsed laser light for biomedical applications include delivering overall less energy into tissue compared to CW lasers and high-order nonlinear excitation. By means of nonlinear absorption, involving two or more lower-energy photons absorbing simultaneously, excitation of nanomaterials from electromagnetic (EM) radiation in the relatively long wavelength tissue transparency windows can be accomplished.[23] Complementary to longer wavelength excitation, nonlinear absorption facilitates excitation to higher electronic states that generally would not be achieved because of the limited ability of plasmonic nanoparticles to absorb photons only within the local plasmonic resonant wavelengths.

Advantages of nonlinear excitation are recognized in multiphoton microscopy. With the continuing development of solid-state fs lasers, new capabilities of nonlinear microscopy have heightened biological imaging.[24] Multiphoton microscopy has facilitated noninvasive imaging, subcellular 3D mapping, higher penetration depth, and reduced photobleaching.[25] When Denk *et al.* in 1990 first demonstrated two-photon microscopy of living cells, this technique has been increasingly applied.[26] Additionally, multiphoton microscopy can be used not only for bioimaging but also for triggering plasmonic heat generation from gold nanoparticles.[16,17,27]

One of the unique and useful plasmonic nanostructures developed recently is the hollow gold nanospheres (HGNs).[28,29] HGNs have surface plasmon resonance (SPR) absorption that is highly tunable in the entire visible to near IR region controlled by varying the shell diameter and thickness. HGNs have been applied successfully for surface enhanced Raman scattering (SERS) and PTT cancer treatment applications.[30-32]

In this work, we report the first study of 2PPL from HGNs and quantitatively compared them with GNRs. The stronger 2PPL from GNRs were partly attributed to the "lightning rod effect," however, we have identified stronger 2PPL by varying the shell thickness of HGNs. Thin shell HGNs, with strong electron confinement, were observed to have a higher 2PPL quantum yield than HGNs with thicker shells. In addition, an exceptionally large two-photon action cross-section from HGNs (~1.02×10^6 GM at 820 nm) was discovered as well as similar but slightly lower 2PPL quantum yield compared to GNRs. Due to the much larger two-photon action cross-section of HGNs compared to GNRs and their slightly lower 2PPL yield, HGNs may

provide an improved platform for cancer theranostics. As a demonstration, HGNs were applied towards nonlinear bioimaging and PTT of cervical cancer HeLa cells using multiphoton microscopy. HGNs bioconjugated with folic acid nutrient were shown to selectively bind and image HeLa cells. Subsequently, slight increases in the power and laser scanning dwell time led to effective destruction of the cancer cells. Significantly less mean power density and exposure time was used to kill cancer cells in this report compared to previous studies using GNRs.[16,17]

2.3. Experimental Section

2.3.1. Synthesis and Characterization

For the synthesis of HGNs,[33] aqueous $CoCl_2$ (0.4 M, 100 μL) and aqueous sodium citrate (0.1 M, 100 μL) were added to 100 mL of Milli-Q water in a double neck round-bottom flask. The solution was vacuumed for 5 min to deoxygenate the solution and then exposed to nitrogen gas. After 2 min under nitrogen gas, freshly prepared $NaBH_4$ solution (0.25 M; 390, 400, 420, or 480 μL) and aqueous PVP (0.1%, 10 μL) was simultaneously injected into the solution. The amount of $NaBH_4$ solution corresponds from red-shifted to blue-shifted HGNs synthesized, respectively. The round-bottom flask was then swirled by hand until the color changed from clear to brown to gray (stayed brown for blue-shifted HGNs). Aqueous citric acid (0.1 M, 160 μL) was then injected and swirled for 10 seconds. After 10 min of growth, 30 mL of the solid cobalt particle solution was quickly added to 10 mL of Milli-Q water containing of aqueous $HAuCl_4$ (0.1 M; 20, 20, 28, or 35 μL) and swirled. More gold

was added for the blue-shifted HGNs. The solution color changed immediately from gray to green for the HGNs with peak SPR at 786 and 790 nm, and from brown to blue for the HGNs with peak SPR at 620 and 680 nm. HGNs were washed 3x by centrifugation with Milli-Q water to purify the particles.

For the GNR synthesis,[34] CTAB aqueous solution (0.1 M, 10 mL) was mixed with $HAuCl_4$ (50 mM, 50 mL) and ice-cold $NaBH_4$ (10 mM, 0.6 mL) to form a brownish-yellow seed solution. This seed solution was kept at room temperature for at least 2 h. In the growth solution, CTAB solution (0.1 M, 10 mL) was mixed with $HAuCl_4$ (50 mM, 0.1 mL), $AgNO_3$ (10 mM, 72 mL), HCl (1.0 M, 0.2 mL) and ascorbic acid (0.1 M, 80 mL). After gentle mixing, the color of the growth solution changed to colorless. The gold seed solution (25 mL) was then added into the growth solution and the reaction mixture was left undisturbed overnight. The obtained GNRs were purified once by washing with de-ionized water to remove excess CTAB and re-dispersed in 10 mL de-ionized water.

The UV-Vis absorption spectra were obtained using an Agilent Cary 60 UV-Vis spectrophotometer (Agilent Technologies). The HR-TEM images were obtained using a Tecnai 12 electron microscope at the National Center for Electron Microscopy in Lawrence Berkeley National Laboratory and the STEM images were taken using a Quanta 3D FEG at the Baskin Engineering at UC Santa Cruz. Image-J software was used to determine the average gold nanoparticle dimensions by measuring at least 50 nanoparticles. The concentrations of nanoparticles were determined using a Perkin Elmer Optima 5300DV inductively Coupled Plasma-Optical Emission Spectrometer (ICP-OES) for determining the gold concentration of each nanoparticle solution. The

dimensions of a hollow sphere and solid cylinder were used for HGN and GNR, respectively, to determine the number of gold nanoparticles for each solution.

2.3.2. 2PPL Measurements of HGN and GNR in Solution

The 2PPL spectra of HGNs and GNRs were measured by using mode-locked Ti:Sapphire laser (Chameleon Ultra II, Coherent) as excitation source with center wavelength at 820 nm, 140 fs pulse duration and a repetition rate of 80 MHz. The uncertainty of the center wavelength was calculated using the following equation:

$$\Delta\lambda \geq \frac{\lambda_0^2}{\Delta t \cdot c}$$

where $\Delta\lambda$ is the full width at half maximum (FWHM), λ_0 is the center wavelength, and Δt is the pulse duration. The HGN and GNR solutions were placed in a 1 cm cuvette and were excited with a tightly focused laser beam. The power before the sample was measured to be 100 mW. The emission signal was collected at 90° angle to the direction of excitation laser beam to minimize the laser scattering. Signal was detected by a CCD (Princeton Instrument, Pixis 100B) coupled monochromator (Acton, Spectra Pro 2300i) through an optical fiber. To reduce the interference of laser scattering, an 800 nm long pass filter and a 750 nm short pass filter, blocking edge BrightLine® multiphoton emission filters purchased from Semrock, were placed in the excitation and emission path, respectively. The concentration of HGNs measured with peak SPR 620, 680, 786, and 790 nm were 1.5×10^{-12} M, 4.6×10^{-12} M, 1.5×10^{-12} M, and 1.9×10^{-12} M, respectively, while the GNRs were at 1.0×10^{-10} M.

2.3.3. Comparing HGN and GNR 2PPL yield

During the 2PPL emission spectra measurements of HGNs with peak SPR 620, 680, 786, and 790 nm the optical densities at 820 nm were 0.0339, 0.0408, 0.0944, and 0.0951, respectively, and the GNR was 0.272. The quantum yield of HGNs was calculated using the following equation:

$$QY = QY_{ref}\frac{A_{ref}}{A}\frac{I}{I_{ref}}$$

where, QY_{ref} is the quantum yield of GNRs with similar size and aspect ratio in this study, previously reported to be 2×10^{-4}.[35] A_{ref} and A and are optical densities at 820 nm of the GNR and HGN, and I and I_{ref} are integrated 2PPL intensities of HGN and GNR, respectively.

2.3.4. Two-Photon Action Cross-Section Measurements

Two-photon action cross-sections $\eta\delta_2$ (where η is photoluminescence quantum yield and δ_2 is two-photon absorption cross-section) of HGNs were determined by using GNR (average aspect ratio 4.08, average size 49 × 12 nm) as the reference (two-photon action cross-section 2.6×10^4 GM at 820 nm).[11] The 2PPL spectra of various HGNs and the 808 nm GNR solution were measured using 820 nm fs laser pulses under identical experimental conditions. The molar extinction coefficient of different nanoparticles was measured by using the method from Orendorff *et al.*[36] The two-photon action cross-section was calculated using the following equation:[37]

$$(\eta\delta_2)_{sample} = \frac{I_{sample}}{I_{ref}} \times \frac{A_{ref}}{\varepsilon_{ref}} \times \frac{\varepsilon_{sample}}{A_{sample}} \times (\eta\delta_2)_{ref}$$

where $(\eta\delta_2)_{sample}$ and $(\eta\delta_2)_{ref}$ are two-photon action cross-section of sample and reference. I_{sample} and I_{ref} are integrated 2PPL intensities measured under the same experimental conditions. A_{sample} and A_{ref} are optical densities of sample and reference at 820 nm. ε_{sample} and ε_{ref} are molar extinction coefficient of sample and reference at 820 nm.

2.3.5. Nonlinear Excitation Profile of HGNs

To determine the nature of the nonlinear excitation process of HGNs, the 2PPL emission intensity was measured as a function of excitation power. The 2PPL intensity from the HGNs were measured at increasing excitation pulse energies (**Figure 2.3.1a**). For 2PPL, a quadratic dependence of PL emission intensity on the excitation intensity is expected. Therefore, on logarithmic scale, a straight line connecting the data with a slope factor of 2 should be observed for a two-photon excitation process. In this excitation intensity study, a pulse energy dependence (Signal $\propto$ Power^n) was observed with a slope value of n = 1.8103, characteristic of a two-photon excitation mechanism.

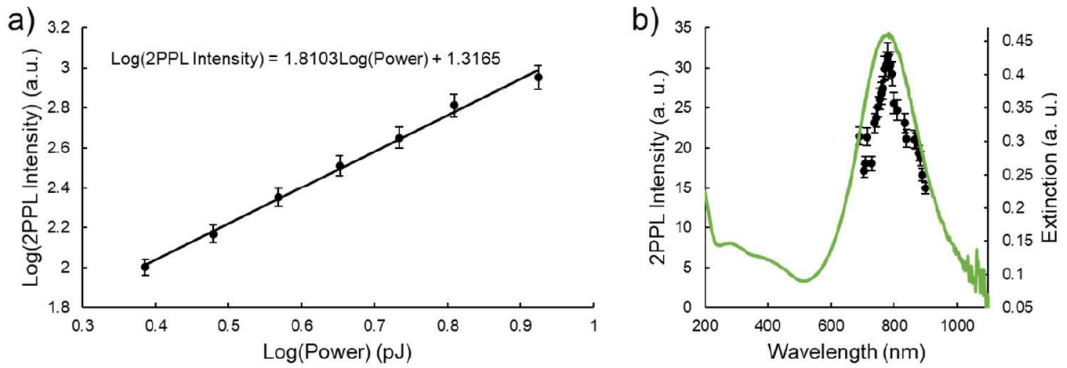

Figure 2.3.1. *a) The dependence of 2PPL emission intensity on the excitation power. Emission was detected in Channel 2 (495-540 nm) of the photomultiplier tube. At the excitation wavelength of 800 nm, with excitation pulse energy at 2.43 pJ, 3.01 pJ, 3.70 pJ, 4.49 pJ, 5.42 pJ, 6.44 pJ, and 8.4 pJ. b) The nonlinear 2PPL excitation spectra of HGNs (dotted lines) are plotted with the one-photon extinction spectrum that has SPR peaked at 780 nm. An incident pulse energy of 32.5 pJ was used for all excitation wavelengths.*

With the aim of gaining further understanding of the 2PPL from HGNs, an excitation profile was acquired for investigating two-photon emission intensity in response to resonant excitation wavelength (**Figure 2.3.1b**). The linear extinction spectrum overlaid with the 2PPL excitation spectrum showed paralleled 2PPL intensity with extinction, indicating a stronger 2PPL intensity via plasmon coupling. Near the plasmon resonance, the two-photon excitation spectrum was observed to have a narrower bandwidth than the one-photon extinction band, which is expected due to the quadratic dependence of two-photon luminescence.

2.3.6. Cell Culture

HeLa cervical cancer cells (ATCC® CCL-2™) were cultured in an incubation chamber in 5% CO_2 at 37 °C in Dulbecco's Modified Eagle's Medium with 10% fetal bovine serum. Cells were collected by trypsinization and plated at a concentration of ~1.3×10^4 per well in a µ-Slide 8 Well and incubated overnight.

2.3.7. Conjugation of Folic Acid-PEG-SH to HGNs

Heterobifunctional Folic acid-PEG-Thiol (MW 5K Da), was purchased from NANOCS Inc. Hank's Balanced Salt Solution (HBSS) was purchased from ThermoFisher Scientific. HGNs were washed with Milli-Q water 3x and concentrated using a 13k rpm centrifuge. The concentration of washed particles was adjusted by their optical density to 5.0 measured by UV-Vis spectroscopy. Concentrated HGNs were bioconjugated by addition of 100 µL of 1 mg/mL folic acid-PEG-thiol (prepared in air free condition) to 500 µL of nanoparticle solution. The prepared solution was incubated overnight while stirring at 4 °C. Conjugated HGNs were washed the next day by centrifuging for 5 minutes at 13k rpm and re-dispersed in HBSS buffer solution. Bioconjugation of nanoparticles was tested using UV-Vis spectroscopy. HGN-FAs displayed a 25 nm red-shift in SPR.

2.3.8. Excitation Profile, Bioimaging, and Cancer Treatment

An Olympus FV1000 dedicated Multiphoton scope with a standard Hamamatsu PMT non-descanned detectors and Spectra Physics MaiTai HP DeepSee fs Ti:Sapphire laser was used to obtain the excitation spectrum and pulse energy dependence profile

as well as perform cancer imaging and treatment experiments. The laser has a pulse duration of 100 fs and a repetition rate of 80 MHz. The laser beam was directed into a 25×/1.05 NA water immersion objective and focused on HGN-FA/cell solutions in a μ-Slide 8 Well (ibiTreat, 80826). The 1.05 NA water immersion objective was used to image fixed HeLa cells in ethanol, while the 10×/0.3 NA dry objective was used in the simultaneous treatment and imaging experiments. The 0.3 NA objective penetrated a ~ 7 mm depth of HBSS buffer before reaching the HeLa cells. For treatment, cells were plated and incubated overnight. The next day, cells were washed 3× with HBSS buffer with 300 μL HBSS buffer volume remaining in the wells. Then, 200 μL of HGN-FA at an optical density of 3.0 was added and cells were incubated for an additional hour. After incubation, cells were washed again 3× with HBSS buffer and brought to the multiphoton microscope for treatment. Origin coordinates were marked at the bottom corner of the letter b on the slide, and then areas at each well were focused and its (x, y, z) coordinates recorded using the fluoview program. Well coordinates were used to scan the exact area in the center of the well three consecutive times with a 95 s pause between each scan at 800 nm wavelength. The time per scan for treatment was 11.88 s and the dwell time was 20 μs/pixel. The area scanned was 512 pixels by 512 pixels (1269 μm by 1269 μm), and the beam spot area was calculated using the equation $\pi d^2/4$, where d=1.22λ/NA. To calculate the exposure time for individual HGN particles, the following equation was used (beam spot area/pixel area) × 20 μs = 27 μs. For total exposure time, t = 27 μs × 3 scans = 81 μs. The mean power density of the treatment site was calculated by dividing the average laser power with the scanned area.[15,16] After treatment, an ImageXpress Micro XLS Widefield High-Content Analysis System was

used to determine cell viability of the scanned area using confocal imaging protocol for live/dead staining by detecting Propidium Iodide (dead) and DAPI (live). In separate experiments for imaging cell morphological changes and ROS, a Leica SP5 Confocal Microscope was used with a 10×/0.3 NA dry and 63×/1.2 NA water immersion objective. The same treatment conditions were used for these experiments, except for the addition of 2.5 μL of CellROX green during the HGN incubation period.

2.4. Results and Discussions

HGNs, synthesized using the previously reported method by Adams *et al*.,[33] are compared to that of GNRs, synthesized using an earlier described seeding growth method.[34] The linear extinction spectra of several HGN samples and GNRs are shown in **Figure 2.4.1a**,**b**, respectively. The full width half maximum (FWHM) of the HGNs with SPR bands peaked at 620, 680, 786, and 790 nm are 133, 144, 205 and 214 nm, respectively, analogous to a previous report.[29] The GNRs with SPR peaked at 808 nm has a FWHM at 155 nm, which is similar to earlier reported GNRs with the same aspect ratio of 4.08.[11] Both STEM and HR-TEM were used to determine the structure of the HGNs and GNRs, with HR-TEM images shown in Figure 1c,d for the HGNs with peak SPR at 790 nm and GNRs, respectively, and STEM images shown in Figure 1e,f,g for the HGNs with peak SPR at 620, 680, and 786 nm, respectively. The images show a slightly rough and uneven surface for the HGNs, while the GNRs have smoother surface. Two sets of HGN solutions were synthesized to have an outer diameter approximately the same (83, 74, 73, and 83 nm), to observe shell thickness dependence

on optical properties. A summary of the standard deviations as well as the optical and structural characteristics of the HGNs and GNRs is provided in **Table 2.4-1**.

Table 2.4-1 *SPR band position, dimension, normalized integrated 2PPL intensity, and molar extinction coefficient and two-photon action cross-section at 820 nm of HGNs and GNRs.*

HGN SPR peak (nm)	Dimensions (nm)	Normalized Integrated 2PPL intensity	Molar extinction coefficient (ε, M^{-1} cm^{-1}) at 820 nm	Two-photon action cross-section (GM) at 820 nm	Molar extinction coefficient (ε, M^{-1} cm^{-1}) at λ (max)
620	Diameter: 83 ± 14 Shell: 29 ± 5.2	6.07E+6	3.39E+10 ±1.02E+10	8.43E+4 ±2.54E+4	9.93E+10 ±2.99E+10
680	Diameter: 74 ± 14 Shell: 21 ± 4.3	7.85E+6	3.37E+10 ±1.20E+10	1.08E+5 ±3.88E+4	8.18E+10 ±2.93E+10
786	Diameter: 73 ± 13 Shell: 12 ± 2.7	1.63E+7	1.12E+11 ±6.00E+10	7.47E+5 ±3.34E+5	1.18E+11 ±5.29E+10
790	Diameter: 83 ± 12 Shell: 11 ± 2.1	1.76E+7	1.42E+11 ±5.01E+10	1.02E+6 ±4.32E+5	1.49E+11 ±6.29E+10
GNR (reference) SPR peak at 808 nm	Length: 49 ± 6.1 Width: 12 ± 1.7	2.34E+7	2.72E+09	2.60E+4	2.92E+09

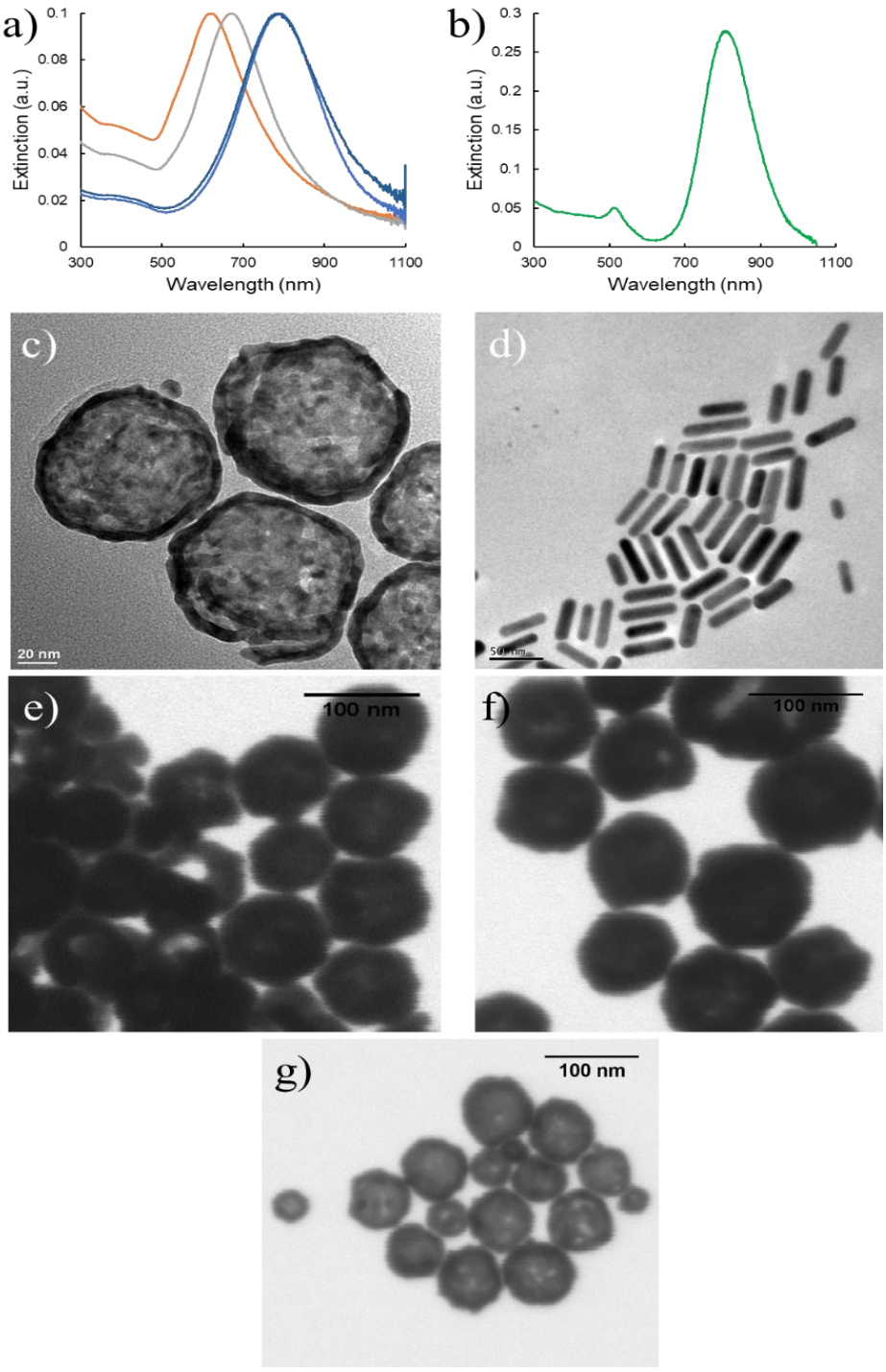

Figure 2.4.1. *UV-Vis spectra of HGNs a) and GNRs b). HR-TEM images of HGNs with peak SPR 790 nm c) and GNRs d). STEM images of HGNs with peak SPR 620 nm e), 680 nm f), and 786 nm g).*

Using the method from Orendorff *et al*.,[36] the molar extinction coefficients of the nanoparticle solutions were determined. The molar extinction coefficient of the GNRs at 820 nm was 2.72×10^{9} $M^{-1}cm^{-1}$, matching a previously reported value.[38] The HGN samples had molar extinction coefficient values ranging from 3.39×10^{10} $M^{-1}cm^{-1}$ to 1.42×10^{11} $M^{-1}cm^{-1}$, which is confirmed by a previously reported value within this range.[39] The integrated 2PPL intensity, molar extinction coefficient and extinction value at 820 nm were used to calculate the two-photon action cross-sections of the HGNs using Equation 3 in the experimental section, with the GNR sample used as a reference.[11] The largest two-photon action cross-section came from the HGNs with peak SPR at 790 nm, which was ~1.02×10^{6} GM, compared to 2.4×10^{4} GM for the GNR reference. A summary of two-photon action cross-section values measured is presented in **Table 2.4-1**.

The calculated molar extinction coefficient at peak SPR revealed that the GNRs in this study require ~40 and ~51 times the amount of gold nanoparticles to absorb/scatter the same number of photons as the HGNs with SPR band peak at 786 and 790 nm, respectively (**Table 2.4-1**). However, the HGNs with peak SPR 786 and 790 nm have ~25 and ~32 times more gold per particle than the GNRs, respectively. Therefore, translating to per unit mass of gold, it was determined that it takes 1 gram of the GNRs to absorb/scatter the same amount of light as ~0.63 gram of the thin shell HGNs with peak SPR at 786 and 790 nm. In contrast, 1 gram of GNRs matches the amount of light absorbed/scattered by ~5.0 grams and ~3.3 grams of the thick shell HGNs with peak SPR at 620 nm and 680 nm, respectively. These results may correspond to the different degrees of shell thickness effecting their absorption

properties, however, increase in absorption/scattering cross-section is proportional to volume and mass for most gold nanostructures including GNRs,[40,41] therefore, theoretical simulation is required to more accurately compare absorption properties. Nonetheless, in this study, comparing the HGNs with similar outer diameter, enhancements in absorption/scattering at their peak resonance wavelength when decreasing the volume and mass of gold was observed. The enhanced absorption/scattering of the thin shell HGNs compared to the thick shell HGNs with similar outer diameter can be explained in a manner similar to that for HGNs compared to solid gold nanoparticles.[42] Theoretical calculations and experimental results in our previous studies have revealed a strong dependence of shell thickness with absorption. It was discovered that molar extinction coefficients at peak resonance wavelength increases with decreasing shell thickness. Our research has shown up to a 2.4 increase in optical density and a significantly enhanced electric field when comparing a solid gold nanosphere with a HGN of the same diameter.[42] These results are confirmed in this study as well. Based on the average measurements of the distinctive HGNs' dimensions, the thin shell HGNs with peak SPR at 790 nm have approximately a ~1.5 times greater molar extinction coefficient at peak resonance wavelength as the thick shell HGNs with peak SPR at 620 nm (both with 83 nm outer diameter) and the thin shell HGNs with peak SPR at 786 nm have a ~1.4 times greater molar extinction coefficient at peak resonance wavelength as the thick shell HGNs with peak SPR at 680 nm (74 and 73 nm outer diameter, respectively). However, these results may be obscured from measurement error, as described in **Table 2.4-1**. By decreasing the mean free path of electrons by confining them in a thin shell, consequently, more electrons

are forced into a denser conduction band along with coalescing electron resonance. Electron confinement in HGNs can be fine-tuned towards a maximum threshold value, when any further decrease in shell thickness is less than the mean free path length of the conduction band electrons and surface scattering occurs.[42]

Regarding the 2PPL spectra, GNRs exhibited a broadband emission in the 400 nm to 650 nm region along with an anticipated red emission, which is impossible to measure due to the use of short pass filters to block the excitation laser, consistent with previous studies (**Figure 2.4.2a**).[10,11,34,43,44] Examining the HGN 2PPL spectra in **Figure 2.4.2b**, the 2PPL intensity increases with increasing emission wavelength, up to the cutoff wavelength of the short pass filter, indicating that the 2PPL is dominated by red emission, as seen in GNRs. Both the GNR and HGN 2PPL spectra exhibit broadband two-photon emission, ranging from approximately 370 nm to the 750 nm cutoff wavelength. As previously reported, ultrashort pulse laser excitation of gold nanostructures has demonstrated emission band broadening.[10,11,34,43,44] Several factors can contribute to this broadening, such as the uncertainty in wavelength or energy due to the fs laser pulses used (~140 fs). This uncertainty was calculated to be about 16 nm FWHM of the pulse laser excitation, calculated using Equation 1 in the experimental section. Additionally, hot electrons may contribute to the two-photon emission broadening. In a report by Huang *et al.*, light emission from GNRs was attributed to electronic Raman scattering and broadened by a high-temperature distribution of electronic excitations.[44] Based on this work, the contribution of electronic Raman scattering cannot be ruled out in our case. However, the PL lifetime of GNRs has been

reported to be on the 50 fs to 100 ps timescale,[45,46] much longer than the expected near-instantaneous electronic Raman scattering process. Therefore, if we assume the origin and lifetime of emission observed in HGNs are the same as that of GNRs, the emission is not likely primarily Raman scattering due to the long lifetime. Furthermore, an investigation of gold nanowires relates broad PL spectra to lattice temperature and the observed emission was attributed to plasmon induced thermal radiation.[47] On the other hand, previous work has demonstrated PL of bulk gold film at 10 K,[1] which would be unlikely to be from thermal radiation. Therefore, there may be multiple mechanisms in operation in the observed non-linear light emission of metal structures. In our case here, we attribute the emission to 2PPL but cannot completely rule out possible contributions from other mechanisms discussed above. The HGNs with SPR peaked at 786 nm and 790 nm displayed comparative 2PPL quantum yield to GNRs, 70% and 75%, respectively, while the HGNs with bluer SPR peaks at 620 nm and 680 nm demonstrated much weaker two-photon emission, 26% and 34%, respectively, of the GNR's 2PPL quantum yield, calculated using Equation 2 in the experimental section. The normalized integrated 2PPL intensity of each sample is summarized in **Table 2.4-1**. The PL quantum yield of GNRs with similar aspect ratio as this study and fs laser excitation was previously calculated to be 2×10^{-4}.[35] Therefore, the HGNs would have a quantum yield of 1.5×10^{-4}. Previous reports indicate that solid gold nanospheres have a 10^{-7}-10^{-6} quantum efficiency.[48,49] To our knowledge HGNs have the highest reported PL quantum yield of a spherical gold nanoparticle, with a strong dependence on shell thickness. Not only does the 2PPL intensity vary but also the 2PPL spectra shape varies for the distinctive HGNs measured. An emission band was observed near the cutoff

wavelength for the HGNs with SPR band peak at 620 nm. Moreover, the HGNs with higher SPR peak at 680 nm displayed a slight increase in 2PPL intensity as well as a more linear increase with increasing wavelength up to the cutoff wavelength, indicating stronger emission at longer wavelength. This trend continues in HGNs with red-shifted SPR peaks. The HGNs with peak SPR 786 nm and 790 nm demonstrated much higher 2PPL intensity, and additionally, a much sharper increase in 2PPL intensity at the cutoff wavelength, signifying that the emission continuously red-shifted correlating to the HGN SPR peak red-shift and/or has increased intensity.

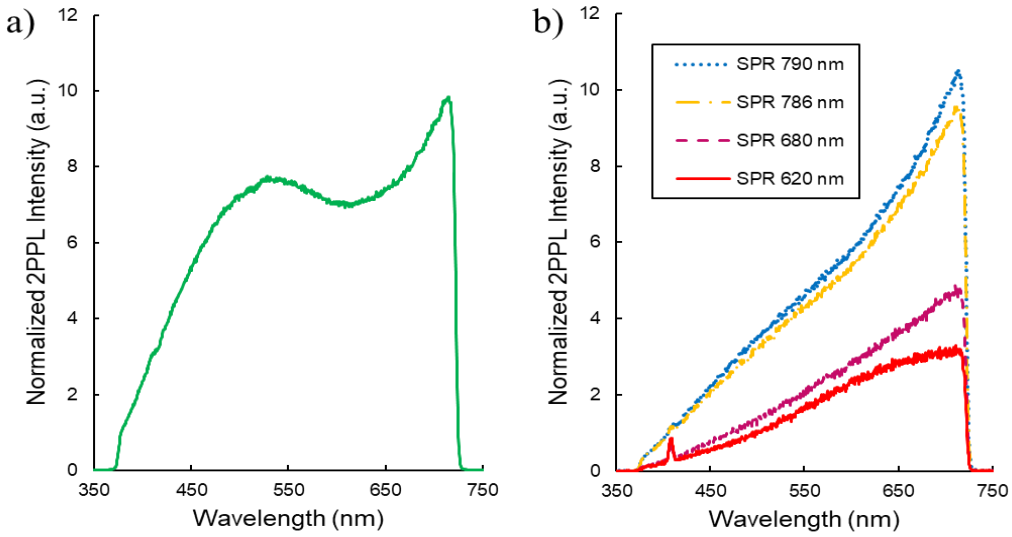

Figure 2.4.2. *The 2PPL spectra of GNRs a) and HGNs b) measured using an 820 nm excitation source from a femtosecond Ti:Sapphire laser. Individual spectra were normalized to the same optical density at 820 nm, using Equation 2 in the experimental section.*

The integrated 2PPL intensity together with molar extinction coefficient was used to calculate the HGN two-photon action cross-section (~1.02×10^6 GM at 820 nm). The large two-photon action cross-section from HGNs is strongly weighted on its ability to absorb photons, having ~0.75 times the quantum efficiency as GNRs but ~51 times the molar extinction coefficient at their peak SPR. For effective photothermal therapy, nanoparticles with large absorption efficiencies and low luminescence quantum yields are more prospective because they ensure a larger light-to-heat conversion efficiency.[50] In addition, HGNs have a much larger surface-to-volume ratio than most nanostructures, due to the inner and outer sphere, which may allow heat to transfer to the surroundings at an ultrafast rate. In a report by Knappenberger *et al*., an ultrafast electron-phonon coupling time of 300 ± 100 fs was observed for HGNs, while for solid spherical gold nanoparticles 770 ± 150 fs was measured.[51] GNRs were reported to have a 750 fs electron-phonon coupling time, similar to bulk gold and solid gold nanospheres.[52] Collectively, larger molar extinction coefficient and lower 2PPL quantum yield at the excitation wavelength as well as faster electron-phonon coupling times suggests fs laser excitation of HGNs should be highly effective for simultaneously generating large amounts of heat energy and 2PPL for theranostics.

For optimized nonlinear bioimaging of HeLa cells using HGNs, a 25×/1.05 NA water immersion objective was used to image fixed cells. HGNs bioconjugated with folic acid-PEG-thiol (HGN-FA) were observed to selectively target cancer cells (**Figure 2.4.3a-e**). HGN-FA signals were found in Channel 1 (420-460 nm), Channel 2 (495-540 nm), and Channel 4 (575-630 nm) of the multiphoton microscope's detection system, with strongest intensity from Channel 4 and weakest intensity in

Channel 1, while DAPI, a nucleic acid stain, was only detected in Channel 1 and 2. From Channel 4, several Z-scan images taken 1.775 μm apart in a single HeLa cell is shown in **Figure 2.4.3a**. From left to right, Z-scan stacks starting near the middle of the cell and ending towards the top of the cell present the extent of HGN-FA internalization. As shown, HGN-FAs (yellow) are highly concentrated throughout the cell but excluded from the cell nucleus region, indicative of a successful endocytosis process of HGN-FA. **Figure 2.4.3b** contains an overlay image of HGN-FA (yellow) and DAPI (magenta). This high resolution (0.38 μm) image unveils detailed contour features of the cancer cells, such as its structure and cell boundary. Cancer cells imaged with only HGN-FA is shown in **Figure 2.4.3c**. In **Figure 2.4.3c**, HGN-FA is represented by all colors observed in the Channel 1, 2 and 4 windows. A detailed outline of individual cells is observed, showing the promising potential of HGN-FA in two-photon imaging applications. To ensure that these detected light signals were not from FA linker or tissue, controls of FA linker and cells only were measured (**Figure 2.4.3d,e**). To obtain an image from these controls 750< gain as well as 79 mW and 88 mW of power were used, respectively, while the other images were taken with 0.1-1.0 mW and a 600-650 gain value.

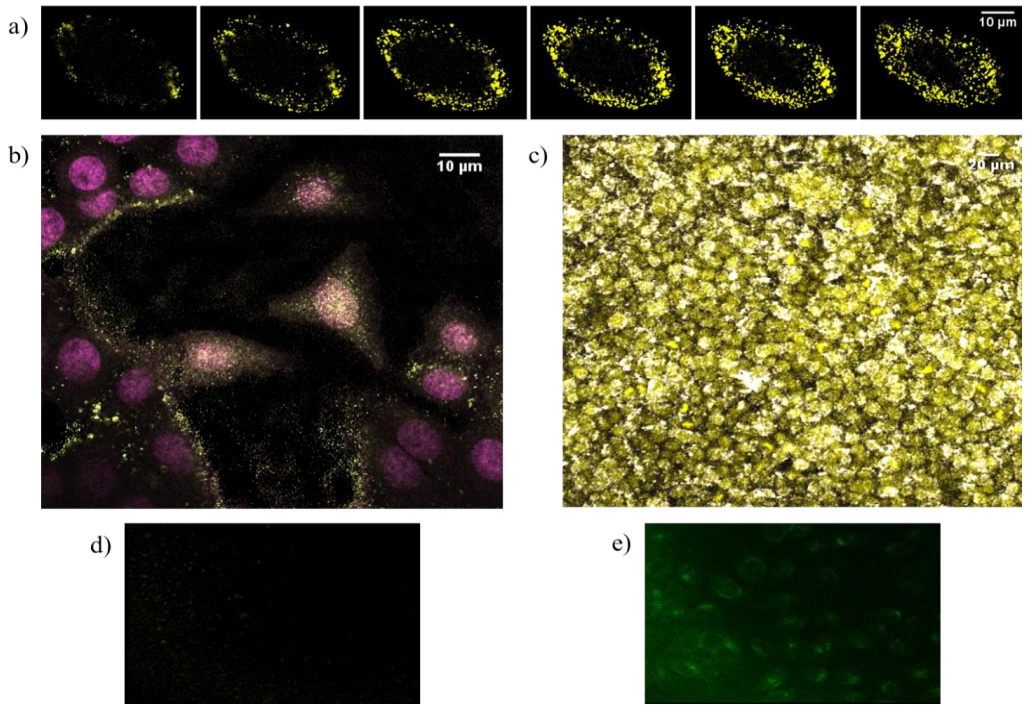

Figure 2.4.3. *Yellow color represents Channel 4 (575-630nm), green for Channel 2 (495-540 nm) and magenta for Channel 1 (420-460 nm). a) Z-scan images of HeLa cells taken 1.775 µm apart using HGN-FA (yellow). b) HeLa cell image using DAPI (magenta) and H GN-FA. c) Zoomed-out image of HeLa cells containing HGN-FA without DAPI, represented by overlap of Channel 1, Channel 2 and Channel 4. White color indicates similar intensity from all channels. d) FA linker with HeLa cells. e) HeLa cells only.*

In vitro cancer theranostics using HGN-FA were performed with a 10×/0.3 NA dry objective. An area 1269 µm by 1269 µm (1.61 mm^2) of HeLa cells incubated with HGN-FA was scanned three consecutive times during treatment. The focused NIR fs laser, penetrated a ~7 mm depth of HBSS buffer before reaching the cancer cells.

Figure 2.4.4a shows confocal microscope images of the treatment sites scanned as well as control experiments, and **Figure 2.4.4b** exemplifies cancer theranostics by multiphoton imaging during laser treatment. Large amounts of cell death occurred for cancer cells incubated with HGN-FA using 39 mW along with a correlated decrease in cell death using 32 mW and 25 mW (**Figure 2.4.4c**). No relevant cell death is observed in control experiments. Scanning three consecutive times at HeLa cells with internalized HGN-FA resulted in 81% ± 4.7 (39 mW), 34% ± 5.5 (32 mw), and 16% ± 3.5 (25 mW) cell death.

During treatment, HGN-FAs were exposed to the laser 27 μs at a time (total exposure time 81 μs) and cancer cells collectively on the millisecond timescale, calculations are shown in the experimental section. Since HGN-FAs were exposed to the laser only microseconds at a time, an ultra-fast heat generation mechanism occurred.[50] Typically, excitation of plasmonic gold nanoparticles by CW laser, producing high temperatures for short periods of time, precise treatment sites are obscured.[50] However, excitation by fs laser for brief periods of time, high temperatures are confined and sites of treatment are well-defined.[50] Baffou *et al*. theoretical calculations of fs-pulsed heating of gold nanoparticles confirms this heating confinement by discovering that under a pulsed illumination the temperature follows a $1/r^3$ spatial decrease in temperature whereas under CW illumination there is a $1/r$ spatial decrease.[53] To further supply evidence of this heat confinement, an image offset from the scanned area (**Figure 2.4.4d**) was captured, displaying an exact boundary of the treatment site. Concurrently, temperature confinement using a fs pulsed laser,

ultrafast electron-phonon coupling times from HGN's surface/volume effects,[51] and pinpoint precision sites of treatment from using a scanning microscope points toward a highly effective and safe treatment.

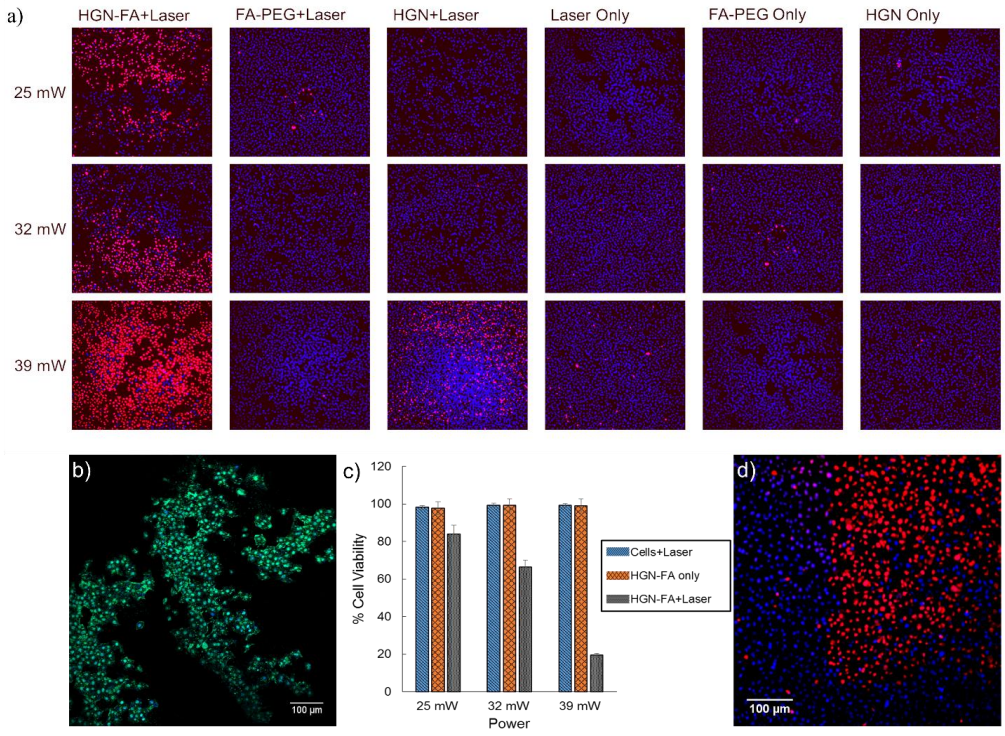

Figure 2.4.4. *a) Confocal fluorescence microscopy images of cancer cells under the following conditions: HGN-FA+Laser, FA-PEG+Laser, HGN+Laser, Laser Only, FA-PEG Only, HGN Only, at 25, 32, and 39 mW average power. Red color represents dead cells stained with PI (propidium iodide) and live cells are represented as blue stained with DAPI (4,6-Diamidino-2-Phenylindole, Dihydrochloride). b) Multiphoton microscopy image of cancer cells during treatment using HGN-FA (green) and DAPI (blue). c) Irradiation power dependent viability of HeLa cells treated with HGN-FA+Laser, Cells+Laser, and HGN-FA only. d) Offset image from the scanned area exemplifying the precision of using laser scanning multiphoton microscopy for cancer therapy.*

Insight into the repercussions from using this method for cancer treatment was assessed by detecting ROS (reactive oxygen species) and imaging the morphological differences between cells with and without HGN-FA after treatment. To ensure no ROS following laser treatment without HGN-FA, three scans at 39 mW were measured and the results show no evidence of ROS (**Figure 2.4.5a**). Consequently, as observed in treatment, comparing cancer cells with HGN-FA (**Figure 2.4.5b**) and without HGN-FA (**Figure 2.4.5d**), dense formations of multiprotein complexes caused by protein denaturation and successive protein aggregation were observed in cancer cells with HGN-FA. High ROS concentrations were additionally seen in cancer cells treated with HGN-FA compared to cancer without HGN-FA, **Figure 2.4.5c,e**, respectively. Higher magnified images show extensive amassed protein structures as well as widespread ROS and cell death, **Figure 2.4.5f,g**, respectively. Moreover, cavitating microbubbles from heat vaporization may have been generated. As depicted in **Figure 2.4.5h**, when using 39 mW for treatment a network of empty cavities was formed, corresponding to a remnant of microbubble formation. Excitation on the fs timescale for plasmonic heat generation in previous studies has also led to cavitating bubble formation.[54] The deciphering feature between the empty cavity formation and membrane blebbing was clear ROS detection in the cavitating bleb structures, as observed in **Figure 2.4.5i**. The network of unfilled cavities was only observed using 39 mW, while membrane blebbing occurred using 25 mW (mean power density of 2.4 W/cm^2 and 1.6 W/cm^2, respectively).

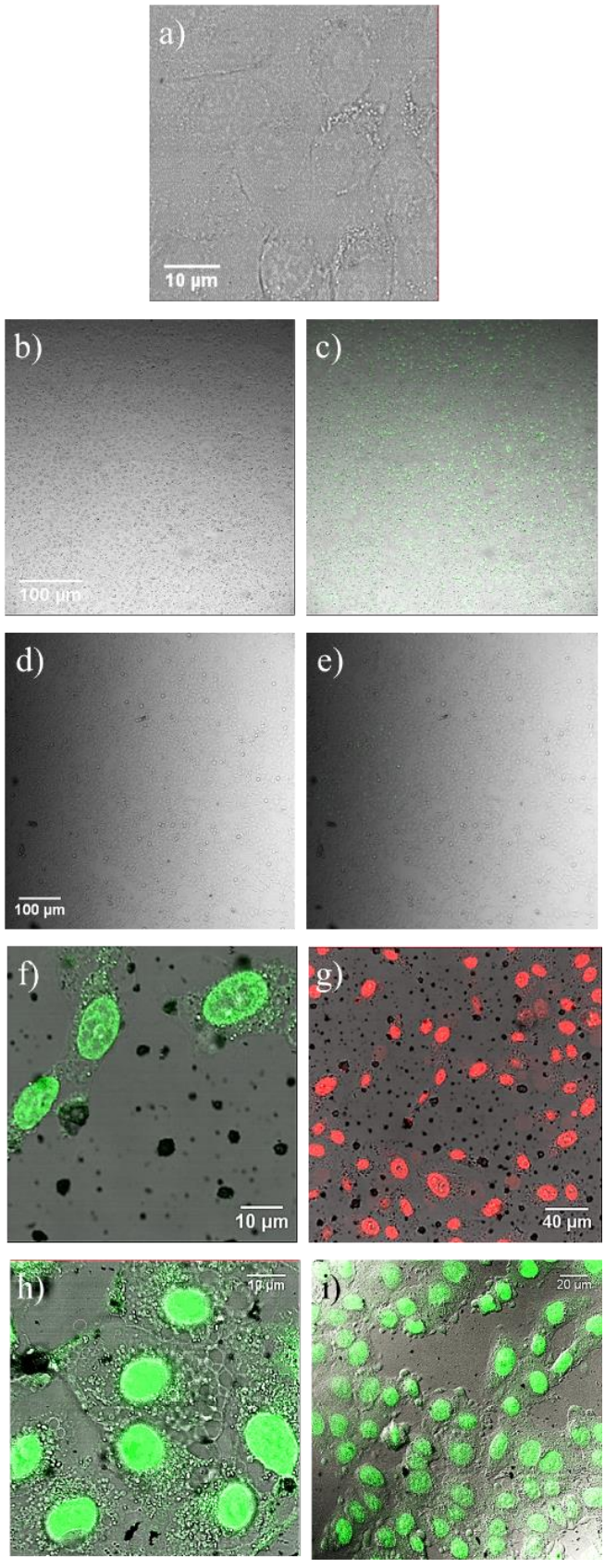
a)
10 µm
b)
100 µm
c)
d)
100 µm
e)
f)
10 µm
g)
40 µm
h)
10 µm
i)
20 µm

Figure 2.4.5. *Bright-field transmission images of HeLa cells after three scans with multiphoton microscope at 800 nm wavelength and 39 mW average power: a) without HGN-FA incubation; b) with HGN-FA incubation; c) overlay image of (b) with ROS detection; ; d) without HGN-FA; e) overlay image of (d) with ROS detection; f) zoomed-in region of (c) presenting protein aggregation; g) zoomed-out image of (f) revealing dead cells stained with PI red dye; h) different zoomed-in region of (c) displaying empty cavitating structures; i) using 25 mW average power, HeLa cell membrane blebbing and ROS.*

Comparing cancer photothermal therapy experiments using GNRs under similar conditions from previous studies,[16,17] the experimental heat efficiency produced by HGNs can be approximately quantified. Pioneering experiments by Tong *et al*.,[17] using GNRs and a multiphoton microscope for cancer imaging and treatment, showed that a mean power density of 48.6 W/cm^2 to treatment sites achieved membrane blebbing after a minimum individual GNR total laser exposure time of 0.76 ms. Later, this method was refocused by Li *et al*. using a circular polarized laser beam for discriminately exciting the longitudinal mode of the GNRs to achieve more effective therapy.[16] In their experiments, using almost identical conditions, a minimum average power density of 5.6 W/cm^2 and laser exposure time of 5.7 ms was used to accomplish cancer cell death. In this study using HGNs, a mean power density of 2.4 W/cm^2 (minimum 1.6 W/cm^2) and an individual HGN total laser exposure time of 81 μs was used, resulting in substantial cell death and morphological changes. Because of the extremely effective photothermal therapy demonstrated in this work using very low

mean power density and exceptionally short laser exposure time, HGNs show excellent promise for fs laser photothermal therapy.

2.5. Conclusions

In summary, evidence of 2PPL from HGNs was observed and confirmed using spectroscopy. The optical properties of HGNs were shown to have a strong dependence on shell thickness. Moreover, HGNs demonstrated an estimated 1.5×10^{-4} 2PPL quantum yield, which to our knowledge is higher than any spherical gold nanoparticles reported to date. Additionally, the thin shell HGNs with peak SPR at 790 nm were calculated to have a two-photon action cross-section of $\sim1.02\times10^{6}$ GM at 820 nm, which is higher than any previously reported value for GNRs. Since the HGNs have approximately three fourths the quantum yield of GNRs and much stronger molar extinction coefficient at peak resonance wavelength, they show great potential for theranostic applications. HGNs, coupled with multiphoton microscopy, administered a highly effective and discriminatory photothermal treatment of HeLa cervical cancer cells, using significantly less mean power density and a substantially shorter laser exposure time than previously reported analogous PTT using GNRs. In this report, HGNs have been proven to be highly promising for photothermal therapeutics as well as nonlinear bioimaging for targeting and subsequently treating cancer cells.

2.6. References

(1) Mooradian, A. Photoluminescence of Metals. *Phys. Rev. Lett.* **1969**, *22*, 185-187.

(2) Huang, X.; El-Sayed, M. A; Gold Nanoparticles: Optical Properties and Implementations in Cancer Diagnosis and Photothermal Therapy. *J. Adv. Res.* **2010**, *1*, 13-28.

(3) Arvizo, R. R.; Bhattacharyya, S.; Kudgus, R.; Giri, K.; Bhattacharya, R.; Mukherhee, P. Intrinsic Therapeutic Applications of Noble Metal Nanoparticles: Past, Present and Future. *Chem. Soc. Rev.* **2012,** *41*, 2943-2970.

(4) Xi, D.; Dong, S.; Meng, X.; Lu, Q.; Meng, L.; Ye, J. Gold Nanoparticles as Computerized Tomography (CT) Contrast Agents. *RSC Advances* **2012**, *2*, 12515-12524.

(5) Popovtzer, R.; Agrawal, A.; Kotov, N. A.; Popovtzer, A.; Balter, J.; Carey, T. E.; Kopelman, R. Targeted Gold Nanoparticles Enable Molecular CT Imaging of Cancer. *Nano Lett.* **2008**, *8*, 4593-4596.

(6) Resch-Genger, U.; Grabolle, M.; Cavaliere-Jaricot, S.; Nitschke, R.; Nann, T. Quantum Dots Versus Organic Dyes as Fluorescent Labels. *Nature Methods* **2008**, *5*, 763-775.

(7) Loumaigne, M.; Vasanthakumar, P.; Richard, A.; Débarre, A. Influence of Polarization and Wavelength on Two-Photon Excited Luminescence of Single Gold Nanospheres. *Phys. Chem. Chem. Phys.* **2011**, *13*, 11597-11606.

(8) Bickford, L.; Sun, J.; Fu, K.; Lewinski, N.; Nammalvar, V.; Chang, J.; Drezek, R. Enhanced Multi-Spectral Imaging of Live Breast Cancer Cells Using Immunotargeted Gold Nanoshells and Two-Photon Excitation Microscopy. *Nanotechnology* **2008**, *19*, 315102.

(9) Au, L.; Zhang, Q.; Cobley, C. M.; Gidding, M.; Schwartz, A. G.; Chen, J.; Xia, Y. Quantifying the Cellular Uptake of Antibody-Conjugated Au Nanocages by Two-Photon Microscopy and Inductively Coupled Plasma Mass Spectroscopy. *ACS Nano* **2010**, *4*, 35-42.

(10) Wang, H.; Huff, T. B.; Zweifel, D. A.; He, W.; Low, P. S.; Wei, A.; Cheng, J. *In vitro* and *in vivo* Two-Photon Luminescence Imaging of Single Gold Nanorods. *Proc. Natl. Acad. Sci. U.S.A.* **2005**, *102*, 15752-15756.

(11) Gao, N.; Chen, Y.; Li, L.; Guan, Z.; Zhao, T.; Zhou, N.; Yuan, P.; Yao, S. Q.; Xu, Q.-H. Shape-Dependent Two-Photon Photoluminescence of Single Gold Nanoparticles. *J. Phys. Chem. C* **2014**, *118*, 13904-13911.

(12) Mohamed, M. B.; Volkov, V.; Link, S.; El-Sayed, M. A. The Lightning' Gold Nanorods: Fluorescence Enhancement of Over a Million Compared to the Gold Metal. *Chem. Phys. Lett.* **2000**, *317*, 517-523.

(13) Imura, K.; Nagahara, T.; Okamoto, H. Near-Field Two-Photon-Induced Photoluminescence from Single Gold Nanorods and Imaging of Plasmon Modes. *J. Phys. Chem. B* **2005**, *109*, 13214-13220.

(14) Durr, N. J.; Larson, T.; Smith, D. K.; Korgel, B. A.; Sokolov, K.; Ben-Yakar, A. Two-Photon Luminescence Imaging of Cancer Cells using Molecularly Targeted Gold Nanorods. *Nano Lett.* **2007**, *7*, 941-945.

(15) Tong, L.; Wei, Q.; Wei, A.; Cheng, J. Gold Nanorods as Contrast Agents for Biological Imaging: Optical Properties, Surface Conjugation and Photothermal Effects. *Photochemistry and Photobiology* **2009**, *85*, 21-32.

(16) Li, J. L.; Day, D.; Gu, M. Ultra-Low Energy Threshold for Cancer Photothermal Therapy Using Transferrin-Conjugated Gold Nanorods. *Adv. Mater.* **2008**, *20*, 3866-3871.

(17) Tong, L.; Zhao, Y.; Huff, T. B.; Hansen, M. N.; Wei, A.; Cheng, J. Gold Nanorods Mediate Tumor Cell Death by Compromising Membrane Integrity. *Adv. Mater.* **2007**, *19*, 3136-3141.

(18) Debbage, P.; Jaschke, W. Molecular Imaging with Nanoparticles: Giant Roles for Dwarf Actors. *Histochem Cell Biol.* **2008,** *130*, 845–875.

(19) Park, K.; Lee, S.; Kang, E.; Kim, K.; Choi, K.; Kwon, I. C. New Generation of Multifunctional Nanoparticles for Cancer Imaging and Therapy. *Adv. Funct. Mater*. **2009,** *19*, 1553–1566.

(20) Frangioni, J. V. *In vivo* Near-infrared Fluorescence Imaging. *Current Opinion in Chemical Biology* **2003**, *7*, 626–634.

(21) Jacques, S. L. Optical Properties of Biological Tissues: A Review. *Physics in Medicine and Biology* **2013**, *58*, R37-R61.

(22) Henderson, T. A.; Morries, L. D. Near-Infrared Photonic Energy Penetration: Can Infrared Phototherapy Effectively Reach the Human Brain? *Neuropsychiatric Disease and Treatment* **2015**, *11*, 2191-2208.

(23) Liu, T.; Conde, J.; Lipiński, T.; Bednarkiewics, A.; Huang C. Revisiting the Classification of NIR-Absorbing/Emitting Nanomaterials for *in vivo* Bioapplication. *NPG Asia Materials* **2016**, *8*, e295.

(24) Keller, U. Recent Developments in Compact Ultrafast Lasers. *Nature* **2003**, *424*, 831-838.

(25) Rubart, M. Two-Photon Microscopy of Cells and Tissue. *Circ. Res.* **2004**, *95*, 1154-1166.

(26) Denk, W.; Strickler, J. H.; Webb, W. W. Two-Photon Laser Scanning Fluorescence Microscopy. *Science* **1990**, *248*, 73–76.

(27) Day, E. S.; Bickford, L. R.; Slater, J. H.; Riggall, N. S.; West, J. L. Antibody-Conjugated Gold-Gold Sulfide Nanoparticles as Multifunctional Agents for Imaging and Therapy of Breast Cancer. *International Journal of Nanomedicine* **2010,** *5*, 445-454.

(28) Schwartzberg, A. M.; Olson, T. Y.; Talley, C. E.; Zhang, J. Z. Synthesis, Characterization, and Tunable Optical Properties of Hollow Gold Nanospheres. *J. Phys. Chem. B* **2006**, *110*, 19935-19944.

(29) Adams, S.; Zhang, J. Z. Unique Optical Properties and Applications of Hollow Gold Nanospheres (HGNs). *Coordi. Chem. Rev.* **2016**, *320-321*, 18-37.

(30) Schwartzberg, A.; Olson, T. Y.; Zhang, J. Z.; Huser, T.; Talley, C. E. Improving Nanoprobes Using Surface-Enhanced Raman Scattering from 30-nm Hollow Gold Particles. *Anal. Chem.* **2006**, *78*, 4732-4736.

(31) Melancon, M. P.; Lu, W.; Yang, Z.; Zhang, R.; Cheng, Z.; Elliot, A. M.; Stafford, J.; Olson, T.; Zhang, J. Z.; Li, C. *In vitro* and *in vivo* Targeting of Hollow Gold Nanoshells Directed at Epidermal Growth Factor Receptors for Photothermal Ablation Therapy. *Mol. Cancer Ther.* **2008**, *7*, 1730-1739.

(32) Lu, W.; Xiong, C.; Zhang, G.; Huang, Q.; Zhang, R.; Zhang, J. Z.; Li, C. Targeted Photothermal Ablation of Murine Melanomas with Melanocyte-Stimulating

Hormone Analog-Conjugated Hollow Gold Nanospheres. *Clin. Cancer Res.* **2009**, *15*, 876-886.

(33) Adams, S.; Thai, D.; Mascona, X.; Schwartzberg, A. M.; Zhang J. Key Factors Affecting the Reproducibility of Synthesis and Growth Mechanism of Near-Infrared Absorbing Hollow Gold Nanospheres. *Chem. Mater*. **2014**, *23*, 6805–6810.

(34) Zhao, T.; Shen, X.; Li, L.; Guan, Z.; Gao, N.; Yuan, P.; Yao, S. Q.; Xu, Q.-H.; Xu, G. Q. Gold Nanorods as Dual Photo-Sensitizing and Imaging Agents for Two-Photon Photodynamic Therapy. *Nanoscale* **2012**, *4*, 7712-7719.

(35) Wu, X.; Yang, F.; Ming, T.; Xiong, R.; Wang, P.; Chen, J. Au Nanorods Can Be Used for Long-Term Cell Imaging? *Appl. Phys. Lett.* **2011**, *98*, 213704.

(36) Orendorff, C. J.; Murphy, C. J. Quantitation of Metal Content in the Silver-Assisted Growth of Gold Nanorods. *J. Phys. Chem. B* **2006**, *110*, 3990-3994.

(37) Oulianov, D. A.; Tomov, I. V.; Dvornikov, A. S.; Rentzepis, P. M. Observations on the Measurement of Two-Photon Absorption Cross-Section. *Optics Communications* **2001**, *191*, 235-243.

(38) Near, R. D.; Hayden, S. C.; Hunter, R. E.; Thackston, D.; El-Sayed, M. A. Rapid and Efficient Prediction of Optical Extinction Coefficients for Gold Nanospheres and Gold Nanorods. *J. Phys. Chem. C* **2013**, *117*, 23950-23955.

(39) Lu, W.; Zhang, G.; Zhang, R.; Flores II, L. G.; Huang, Q.; Gelovani, J. G.; Li, C. Tumor Site-Specific Silencing of NF-κB p65 by Targeted Hollow Gold Nanosphere-Mediated Photothermal Transfection. *Cancer Res.* **2010**, *70*, 3177-3188.

(40) Jain, P. K.; Kyeong, S. L.; El-Sayed, I. H.; El-Sayed, M. A. Calculated Absorption and Scattering Properties of Gold Nanoparticles of Different Size, Shape, and Composition: Applications in Biological Imaging and Biomedicine. *J. Phys. Chem. B* **2006**, *110*, 7238-7248.

(41) Fang, Y.; Chang, W.; Willingham, B.; Swanglap, P.; Dominguez-Medina, S.; Link, S. Plasmon Emission Quantum Yield of Single Gold Nanorods as a Function of Aspect Ratio. *ACS Nano* **2012**, *6*, 7177-7184.

(42) Wheeler, D.; Newhouse, R.; Wang, H.; Zou, S.; Zhang, J. Z. Optical Properties and Persistent Spectral Hole-Burning of Near Infrared-Absorbing Hollow Gold Nanospheres. *J. Phys. Chem. C*, **2010**, *114*, 18126-18133.

(43) Molinaro, C.; Harfouch, Y. E.; Palleau, E.; Eloi, F.; Marguet, S.; Douillard, L.; Charra, F.; Fiorini-Debuisschert, C. Two-Photon Luminescence of Single Colloidal Gold Nanorods: Revealing the Origin of Plasmon Relaxation in Small Nanocrystals. *J. Phys. Chem. C* **2016**, *120*, 23136-23143.

(44) Huang, J.; Wang, W.; Murphy, C. J.; Cahill, D. G. Resonant Secondary Light Emission from Plasmonic Au Nanostructures at High Temperatures Created by Pulsed-laser Excitation. *PNAS* **2014**, *111*, 906-911.

(45) Varnavski, O. P.; Mohamed, M. B.; El-Sayed, M. A.; Goodson III, T. Relative Enhancement of Ultrafast Emission in Gold Nanorods. *J. Phys. Chem. B* **2003**, *107*, 3101-3104.

(46) Zhang, Y.; Yu, J.; Birch, D. J. S.; Chen, Y. Gold Nanorods for Fluorescence Lifetime Imaging in Biology. *J. Biomedical Optics* **2010**, *15*, 020504.

(47) Ma, Z.; Yu, Y.; Shen, S.; Dai, H.; Yao, L.; Han, Y.; Wang, X.; Han, J.-B.; Li, L. Origin of the Avalanche-Like Photoluminescence from Metallic Nanowires. *Scientific Reports* **2016**, *6*, 18857.

(48) Gaiduk, A.; Yorulmaz, M.; Orrit, M. Correlated Absorption and Photoluminescence of Single Gold Nanoparticles. *ChemPhysChem* **2011**, *12*, 1536-1541.

(49) Dulkeith, E.; Niedereichholz, T.; Klar, T. A.; Feldmann, J. Plasmon Emission in Photoexcited Gold Nanoparticles. *Phys. Rev. B* **2004**, *70*, 205424.

(50) Jaque, D.; Maestro, L. M.; del Rosal, B.; Haro-Gonzalez, P.; Benayas, A.; Plaza, J. L.; Rodriguez, E. M.; Sole, J. G. Nanoparticles for Photothermal Therapies. *Nanoscale* **2014**, *6*, 9494-9530.

(51) Knappenberger, K. L. Jr; Schwartzberg, A. M.; Dowgiallo, A. M.; Lowman, C. A. Electronic Relaxation Dynamics in Isolated and Aggregated Hollow Gold Nanospheres. *J. Am. Chem. Soc.* **2009**, *131*, 13892–13893.

(52) Jiang, Y.; Wang, H.-Y.; Xie, L.-P.; Gao, B.-R.; Wang, L.; Zhang, X.-L.; Chen, Q.-D.; Yang, H.; Song, H.-W.; Sun, H.-B. Study of Electron-Phonon Coupling Dynamics in Au Nanorods by Transient Depolarization Measurements. *J. Phys. Chem. C* **2010**, *114*, 2913-2917.

(53) Baffou, G.; Rigneault, H. Femtosecond-Pulsed Optical Heating of Gold Nanoparticles. *Phys. Rev. B* **2011**, *84*, 035415.

(54) Kotaidis, V.; Plech, A. Cavitation Dynamics on the Nanoscale. *Appl. Phys. Lett.* **2005**, *87*, 213102.

Chapter 3. Dependence of Stability and Electronic and Optical Properties of Perovskite Quantum Dots on Capping Ligand Chain Length

3.1. Abstract

Methylammonium lead bromide ($MAPbBr_3$) perovskite quantum dots (PQDs) passivated with capping ligands with different chain length, including butylamine-valeric acid (BUTY-VA), octylamine-caprylic acid (OCTY-CA), and dodecylamine-lauric acid (DODE-LA), are investigated to determine an optimized capping layer thickness for maximizing both electronic and antimoisture properties of perovskite materials in optoelectronic devices. The photoluminescence quantum yield (PLQY) is observed to be chain length dependent, where the PLQY of BUTY-VA, OCTY-CA, and DODE-LA MAPbBr3 PQDs is 82% ± 4%, 68% ± 7%, and 18% ± 2%, respectively. Electrochemical impedance spectroscopy (EIS) measurements of each PQD film reveal that there is a slight increase in conductivity from reducing the capping ligand chain length from 8 carbon atoms (OCTY-CA) to 4 carbon atoms (BUTY-VA). Using the Butler-Volmer equation, the charge transfer factor β for BUTY-VA and OCTY-CA MAPbBr3 PQD films in a tetrabutylammonium hexafluorophosphate-dichloromethane electrolyte solution was calculated to be 0.36 and 0.31, respectively. From an Arrhenius analysis, the activation energy (E_a) for charge transport between the PQD film and the electrolyte was calculated to be 77 and 90 meV for BUTY-VA and OCTY-CA MAPbBr3 PQD films, respectively. Moreover, passivating PQDs with capping ligands

with 12 carbon atoms (DODE-LA) almost completely insulates the PQDs and diminishes charge transport. This is also observed in transient photocurrent density measurements. The results suggest that the inter-PQD distance in this solid film is too long for effective tunneling to occur. However, using BUTY-VA capping ligands to improve electronic properties of PQD solid film comes with a cost of stability.

3.2. Introduction

Organo-metal halide perovskite quantum dots (PQDs) based on the perovskite structure ABX_3 ($A = CH_3NH_3^+$ or Cs^+, $B = Pb^{2+}$, $X = Cl^-$, Br^-, or I^-) offer many potential advantages in optoelectronic devices, including solution-processability and low-cost as well as high photoluminescence quantum yield (PLQY) and absorption coefficient.[1-9] However, major hindrances for commercialization are their lack of charge transport and long-term stability.[10-30] The lack of charge transport is due to passivating the surface charges of the PQDs with long-chain aliphatic ligands with terminal ionic functional groups, such as ammonium, carboxylate, phosphonate, and thiolate ions, that generate an insulating shell around the PQD core.[31] One approach towards increasing charge transport and interdot electronic coupling is tuning the length of the capping ligands.[32-35] In a previous report, $CsPbI_3$ PQDs surface passivated with octylamine and octanoic acid were observed to increase photovoltaic (PV) performance by more than 4% compared to using longer chain ligands oleylamine and oleic acid for passivation.[36] In addition, it is reported that alkylamine capping ligands containing four carbon atoms can decrease the resistance of metallic nanoparticles by nearly 10,000-fold compared to passivating with ligands containing 18 carbon atoms.[37] Nonetheless, greater ligand

shell thickness may also enhance the stability of PQDs. It is shown in a previous report that passivating the surface of a QD with oligomeric alkyl phosphine ligands significantly increase stability compared to smaller monomeric ligands.[38] Therefore, there is a trade-off between enhancing the charge transport and stability properties of PQDs.

For QD film on an insulating substrate that is irradiated, dipole-dipole Förster energy transfer is the dominant mechanism of exciton diffusion as it does not require charges to tunnel or transfer between QDs.[39] Monochromatic QD-QD Förster resonance energy transfer (FRET) can occur in a QD population that contains even a narrow distribution of sizes.[40] This occurs from the large spectral overlap between the PL spectra of a slightly smaller donor QD and the absorption spectra of a marginally larger acceptor QD. However, in QD film on conductive substrate under an electrical load and irradiation, hopping or tunneling charge transport may be the dominant mechanisms in the QD film and at its interfaces. Within a film, QDs are typically spaced by their hydrocarbon capping ligands. The most commonly used hydrocarbon capping ligands for PQDs and other QDs contain 15-30 carbon atoms.[35] At this ligand size, PQDs can be spaced between 4.62 and 9.24 nm. As described in a previous report, the charge tunneling distance limit is $\leq$4.3 nm for PbS QD solid film using organic ligand spacers.[41] Therefore, it is imperative to investigate the advantages and disadvantages of using different chain length capping ligands for obtaining a desired compromise between improving electronic and stability properties of PQDs.

In this work, we investigated the electronic, optical and stability properties of PQDs passivated with ligands containing 4 [butylamine-valeric acid (BUTY-VA)], 8

[octylamine-caprylic acid (OCTY-CA)], and 12 [dodecylamine-lauric acid (DODE-LA)] carbon atoms using an alkylamine and carboxylic acid passivating combination. Electrochemical impedance spectroscopy and transient photocurrent density measurements reveal that there is a significant diminishment in electronic properties when the capping ligand chain length reaches 12 carbon atoms, while there is a relatively small improvement in conductivity and photocurrent density from using ligands containing 8 carbon atoms to 4 carbon atoms. Therefore, 12 carbon atom capping ligands may increase the interdot spacing near the charge tunneling distance limit in the PQD film as well as at its interfaces. However, in a stability test, PQDs passivated with ligands containing 4 carbon atoms is demonstrated to degrade much faster than PQDs with ligands containing 8 and 12 carbon atoms. Thus, it is shown that in order to maintain useful stability, a cost of charge transport efficiency may need to be paid.

3.3. Experimental Section

3.3.1. Materials

All chemicals were used without further purification, which include: toluene (spectroscopic grade, Fisher Scientific), N,N-Dimethylformamide (DMF) (spectroscopic grade, Fisher Scientific), $PbBr_2$ (99.99%, Alfa Aesar), CH_3NH_3Br (MABr) (Greatcellsolar), lauric acid (97%, Spectrum), dodecylamine (DODE) (Oakwood Chemical), n-octylamine (OCTY) (>98%, TCI), caprylic acid (>98%, TCI), butylamine (BUTY) (Oakwood Chemical) and valeric acid (VA) (99%, Alfa Aesar).

3.3.2. Synthesis of $CH_3NH_3PbBr_3$ PQDs

PQDs were synthesized using a solvent reprecipitation method under ambient conditions using a previously report method.[10] MABr (80 μmol, 9.0 mg) and $PbBr_2$ (0.20 mmol, 73 mg) were dissolved in 400 μL DMF. Next, VA (20 μL, 0.18 mmol) or CA (29 μL, 0.18 mmol) or LA (41 μL, 0.18 mmol) was added and dissolved. The carboxylic acid was added before the amine to ensure that MABr does not get deprotonated. Then, BUTY (8 μL, 0.081 mmol) or OCTY (13 μL, 0.081 mmol) or DODE (19 μL, 0.081 mmol) was added and dissolved. This precursor solution was then injected at a relatively fast rate using a borosilicate glass pipette into 5.0 mL toluene that was stirring at 1,600 rpm. The bright yellow PQD solution was purified by centrifugation at 5,500 rpm for 5 min (3 times), with the solid saved and the supernatant discarded. Next, the solid was re-dispersed in 7.0 mL toluene and filtered using loosely packed cotton-plug. Finally, the PQD solution was centrifugated again at 5,500 rpm and concentrated to 40 mg/mL. For PQD film preparation, 200 μL of the 40 mg/mL PQD solution was spin coated on a 1.0 cm^2 fluorine-doped tin oxide (FTO) substrate at 1,200 rpm for 45 seconds.

3.3.3. Spectroscopy and Microscopy Measurements

Absorption and photoluminescence (PL) spectra were measured using an Agilent Technologies Cary UV-vis and HORIBA Jobin Yvon Fluoromax-3, respectively. The PL quantum yield (PLQY) was calculated using fluorescein (95%) as a reference. FT-IR spectra were obtained using a PerkinElmer Spectrum One FT-IR

Spectrometer. Transmission electron microscopy images were obtained on a FEI monochromated F20 UT Tecnai.

3.3.4. Electroanalytical Measurements

The spectroelectrochemical setup consists of a three-electrode cell (counter, reference, and working) in 0.10 M Bu_4NPF_6/dichloromethane solution connected to a potentiostat/galvanostat (SI 1280B). The counter electrode was Pt wire and Ag/AgCl wire was used as a pseudoreference electrode. The electrochemical impedance spectroscopy (EIS) measurements were conducted in the frequency range of 1.0 MHz to 0.10 Hz at open circuit voltage. A xenon lamp at one sun illumination (100 mW/cm^2) was used to illuminate the film (1.0 cm^2). The lifetime of the charge transfer (τ_{rel}) was calculated using the following equation (1):[42]

$$\tau_{rel} = R_{CT} \times CPE$$

where *Rct* is the charge transport resistance obtained from the second x-intercept in the Nyquist plot, and *CPE* is the chemical-phase element obtained from the circuit fitting results. The effective tunneling barrier (α) was calculated using the equation (2):[41]

$$k_{ct} = k_0 e^{(-\alpha r)}$$

where k_{ct} is the rate of charge transfer calculated from τ_{rel} in equation (1), k_0 is the rate of charge transfer at zero distance, and r is the distance between charge donor and acceptor. The Butler-Volmer transfer factor (β) or charge transport coefficient is calculated from the equation (3):[43]

$$R_{CT} = R_{0,CT} e^{(\beta \frac{qV}{k_B T})}$$

where q is the elementary charge, $R_{0,CT}$ is the charge transport resistance at $V = 0$, V is the applied potential, k_B is Boltzmann constant, and T is the temperature. The activation energy (E_a) was calculated using the following Arrhenius equation (4):[44]

$$R_{CT} = R_{0,CT} e^{(\frac{-E_a}{k_B T})}$$

Transient photocurrent response (I-t curve) was measured in the same spectroelectrochemical setup as the EIS measurements. In off/on cycles, one sun illumination (100 mW/cm^2) was applied to the working electrode every 25 sec.

3.3.5. Testing of Stability of PQDs

The relative PL intensity of BUTY-VA, OCTY-CA, and DODE-LA $MAPbBr_3$ PQDs was measured every second for 1 hour.

3.4. Results and Discussions

Shown in **Figure 3.4.1(a-c)** is the UV-Vis absorption and PL spectra of BUTY-VA, OCTY-CA, and DODE-LA $MAPbBr_3$ PQDs, respectively. DODE-LA $MAPbBr_3$ PQDs are observed to have the narrowest emission bandwidth with a full-width-at-half-maximum (FWHM) of 21 nm, while OCTY-CA and BUTY-VA $MAPbBr_3$ PQDs have a FWHM at 24 and 27 nm, respectively. This indicates that the longer chain capping ligands forms more uniformly sized PQDs than shorter chain ligands. The PL peaks obtained were 519, 520, and 524 nm for BUTY-VA, OCTY-CA, and DODE-LA $MAPbBr_3$ PQDs, respectively. The same number of moles of each ligand was used to synthesize each PQD. Therefore, it is confirmed that shorter chain ligands facilitate

stability of smaller sized PQDs, while longer chain ligands are able to stabilize larger sized PQDs. In addition, a trend between PLQY and ligand chain length was observed. The PLQYs of BUTY-VA, OCTY-CA, and DODE-LA $MAPbBr_3$ PQDs are 82 ± 4, 68 ± 7, and 18 ± 2%, respectively. The higher PLQY from passivating with BTYA-VA may be due to less steric hindrance from the shorter alkyl chain. Higher PLQY from using shorter chain ligands has also been observed in previous reports.[36,44]

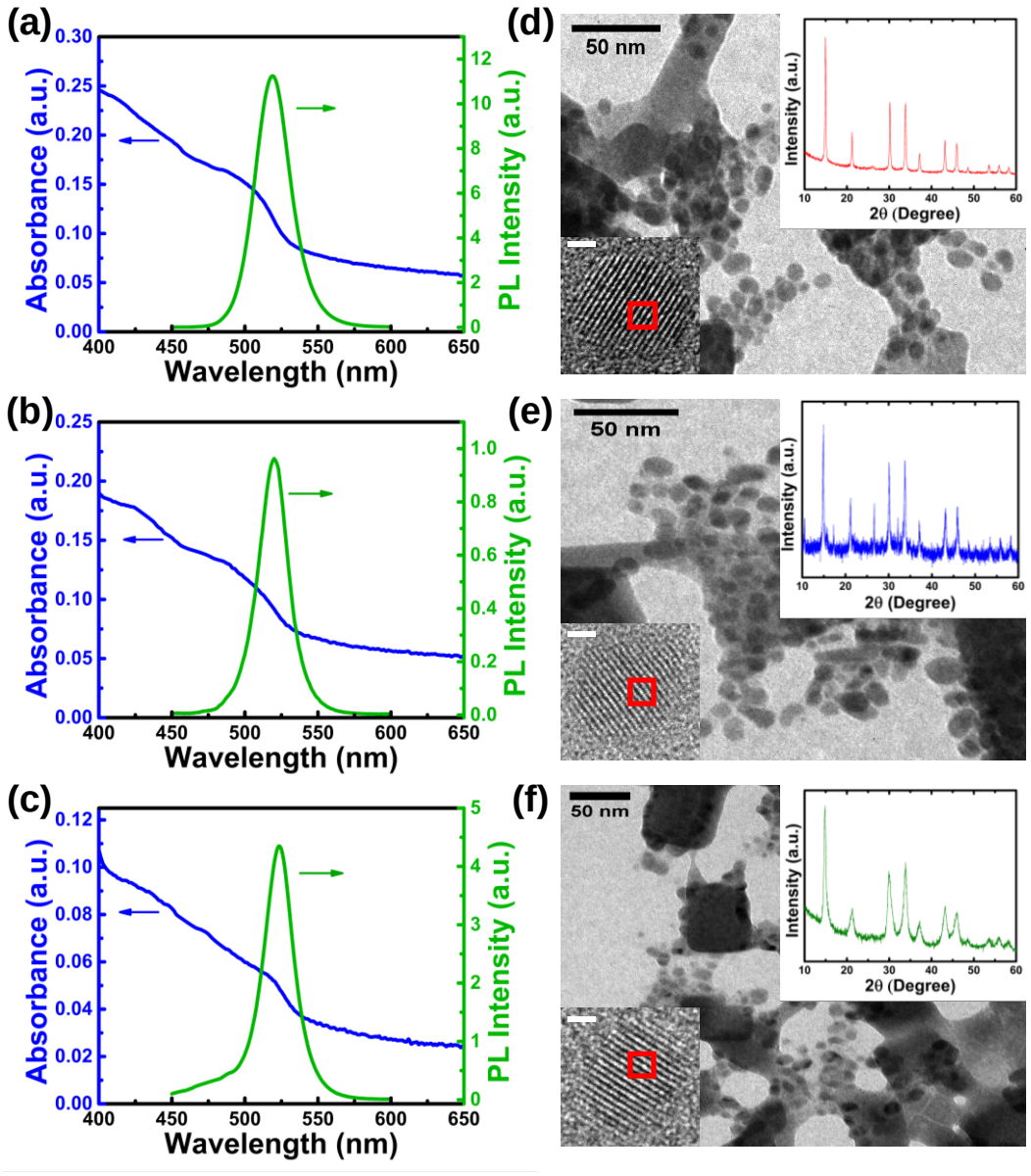

Figure 3.4.1. *UV-Vis absorption and PL spectra of (a) BUTY-VA, (b) OCTY-CA, and (c) DODE-LA $MAPbBr_3$ PQDs. HRTEM images of (d) BUTY-VA, (e) OCTY-CA, and (f) DODE-LA $MAPbBr_3$ PQDs. Inset shows lattice spacing image (red square is where measurement was made) and XRD.*

To determine size and shape characteristics, PQDs were imaged using high-resolution transmission electron microscopy (HRTEM), as shown in **Figure 3.4.1(d-f)**. The average diameter of BUTY-VA, OCTY-CA, and DODE-LA $MAPbBr_3$ PQDs is 7.2 ± 2.8, 8.5 ± 2.1, and 9.2 ± 1.5 nm, respectively. The size and standard deviation are consistent with their PL peak position and FWHM. Shown in the inset of each image is a HRTEM image that shows the lattice spacing. The lattice space for each PQD was measured to be 0.29 nm, indicating the presence of the (002) cubic crystal face of $MAPbBr_3$ perovskite.[46] Additionally, in the inset is the X-ray diffraction (XRD) of each respective PQD. For each PQD, there are XRD peaks at 14.8 º, 21.3 º, 30.0 º, 33.8 º, 37.2 º, 43.2 º, 45.9 º, 53.6 º, 55.9 º, and 58.2º, which are indicative to the crystal planes assigned to the cubic phase of $MAPbBr_3$ perovskite.[46] Moreover, it is observed that the peaks broaden from short to long chain length capping ligands, which indicates better crystal uniformity and less surface defects.

To investigate the ligand binding on the PQD surface, FT-IR was measured for each PQD, as shown in **Figure 3.4.2(a-c)**. Each of the PQD's FT-IR spectra contains similar peaks corresponding to N-H and C-H stretching at 3500-3000 cm^{-1} as well as N-H and C-H bending at 1600-1400 cm^{-1}. BUTY-VA PQDs have a strong peak at 3430 cm^{-1} that corresponds to N-H stretching in the crystal lattice. For OCTY-CA and DODE-LA PQDs, there is a weak peak at 3500 cm^{-1} and two strong peaks at 3185 and 3124 cm^{-1}, which confirms the presence of primary amine. This could indicate poor crystallinity within the lattice as well as residual unprotonated amine capping ligand. In addition, in the FT-IR spectra of OCTY-CA and DODE-LA PQDs, the N-H and C-H bending at 1578 and 1478 cm^{-1}, respectively, are sharp and strong. Whereas, in the

BUTY-VA spectra, these peaks are weaker and broader. These stronger and sharper peaks could indicate that there is more unbound capping ligand in the OCTY-CA and DODE-LA PQD samples, while the BUTY-VA PQD sample has more ligand bound to the perovskite lattice.[47-49]

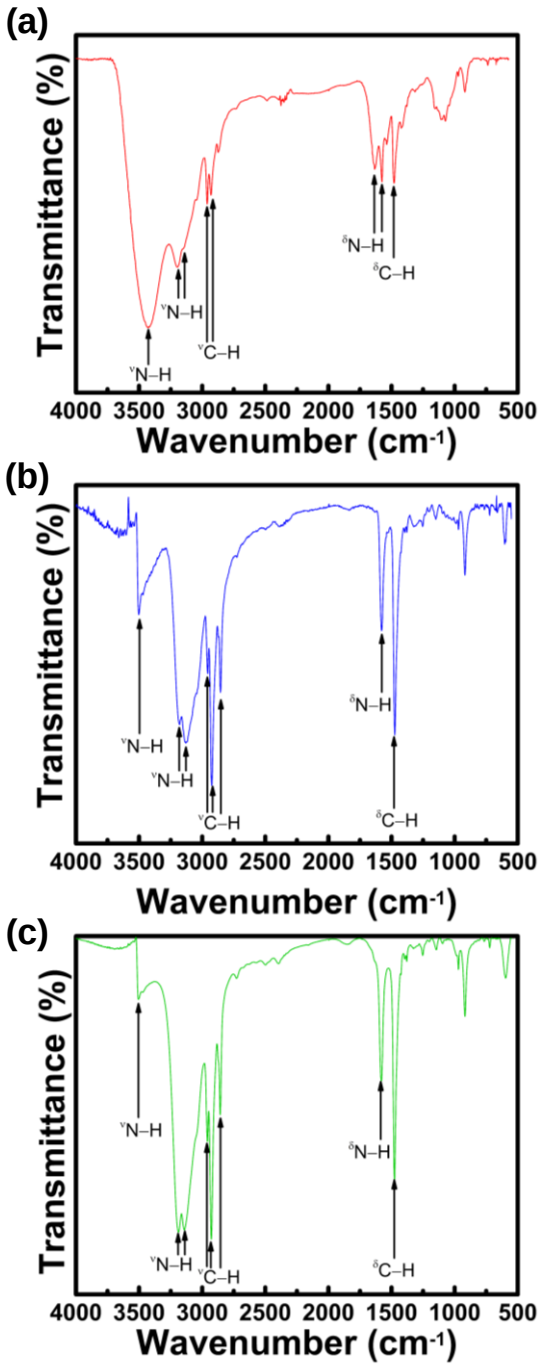

Figure 3.4.2. *FT-IR spectra of (a) BUTY-VA, (b) OCTY-CA, and (c) DODE-LA $MAPbBr_3$ PQDs.*

3.4.1. Electroanalytical Characterization

To study the effects of modifying the capping ligand chain length on the charge transport and conductivity properties, EIS was performed on BUTY-VA, OCTY-CA, and DODE-LA $MAPbBr_3$ PQD films on FTO substrate, as shown in **Figure 3.4.3**. As shown in the Nyquist spectra, the first x-intercept on the real axis corresponds to the series resistance (R_S). R_S is the resistance of charge transfer from the FTO substrate to the PQD film. The R_S is observed to be similar during illuminated and dark conditions for each PQD film. BUTY-VA $MAPbBr_3$ PQD film is observed to have an R_S of 33 Ω, while for OCTY-CA and DODE-LA $MAPbBr_3$ PQD films the R_S value is 37 and 51 Ω, respectively. Additionally, the second x-intercept on the real axis corresponds to the charge transport resistance (R_{CT}) and is the resistance of charge transfer between the PQD film and the electrolyte. Within the measured frequency range, the R_{CT} is not observed in dark conditions for OCTY-CA $MAPbBr_3$ PQD film and is also not observed in both illuminated and dark conditions for DODE-LA $MAPbBr_3$ PQD film. The R_{CT} in illuminated and dark conditions for BUTY-VA $MAPbBr_3$ PQD film is 47 and 55 Ω, respectively. Under illuminated conditions the R_{CT} for OCTY-CA $MAPbBr_3$ PQD film is observed to be 67 Ω. Both the R_S and R_{CT} values from the Nyquist spectra indicate that using BUTY-VA ligands can significantly improve the conductivity and charge transport of PQD films. The time constant of an RC circuit (τ_{rel}), representing the time required to charge the capacitor through a resistor that is parallel in a circuit or lifetime of charge transfer, is calculated to be 2.6 and 3.2 ms for illuminated BUTY-VA and OCTY-CA $MAPbBr_3$ PQD film, respectively.

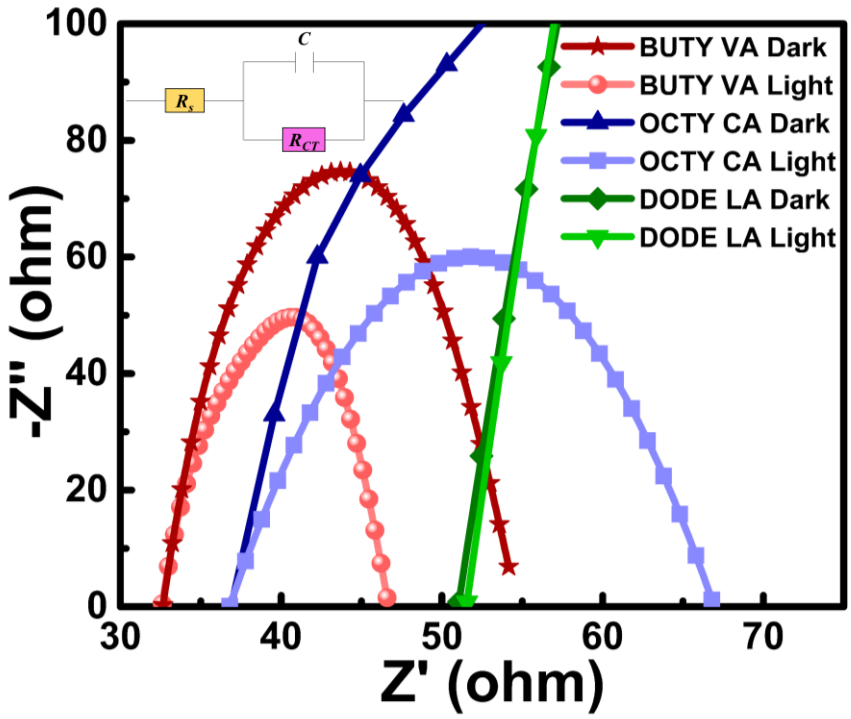

Figure 3.4.3. *Nyquist spectra of BUTY-VA, OCTY-CA, and DODE-LA $MAPbBr_3$ PQD films under 1 sun illumination (100 mW/cm^2) and dark conditions. Inset displays equivalent circuit.*

For investigating the amount of generated photocurrent density, the transient photocurrent response (I-t curve) was measured for each PQD film, as shown in **Figure 3.4.4**. For the DODE-LA $MAPbBr_3$ PQD film, the photocurrent density remained constant, but very low during the total time of the measurement at 0.0113 mA/cm^2. This average photocurrent density generated upon one sun (100 mW/cm^2) illumination has a signal-to-noise ratio of 1.5:1. Therefore, the photocurrent density of DODE-LA $MAPbBr_3$ PQD film is below a reliable detection limit. The average generated photocurrent density of OCTY-CA $MAPbBr_3$ PQD film is 0.057 mA/cm^2, while for

BUTY-VA $MAPbBr_3$ PQD film it is 0.090 mA/cm^2. Thus, increasing the capping ligand chain length from 4 carbon atoms to 8 carbon atoms decreases the photocurrent density by 37% and from 4 carbon atoms to 12 carbon atoms decreases the photocurrent density by 87%. However, BUTY-VA $MAPbBr_3$ PQD film's photocurrent density decreased the most from its initial to final measurement. BUTY-VA $MAPbBr_3$ PQD film's initial photocurrent density was at 0.128 mA/cm^2, but at the final measurement, from 425 to 450 seconds, the photocurrent density dropped to 0.066 mA/cm^2. This corresponds to a 48% decrease in photocurrent density, which is associated with BUTY-VA $MAPbBr_3$ PQD film's stability in the electrolyte and at open circuit voltage.

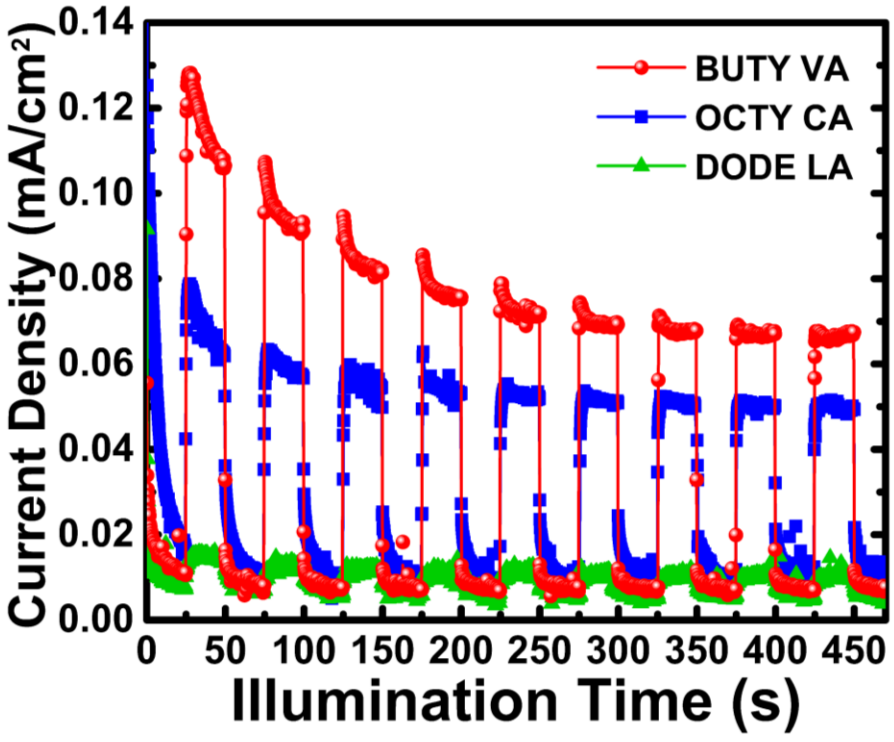

Figure 3.4.4. *Transient photocurrent response of BUTY-VA, OCTY-CA, and DODE-LA $MAPbBr_3$ PQD films.*

In contrast, the photocurrent density of the OCTY-CA $MAPbBr_3$ PQD film dropped by 26% from initial to final measurement. This may reflect towards greater stability properties from passivating with longer length ligands.

3.4.2. Stability of PQDs

The stability of BUTY-VA, OCTY-CA, and DODE-LA $MAPbBr_3$ PQDs was evaluated by measuring relative PL intensity for 1.1 h under air and dark conditions. As shown in **Figure 3.4.5a**, the relative PL intensity of the BUTY-VA $MAPbBr_3$ PQDs decreased to 47% after 1.1 h. In addition, the relative PL intensity for the OCTY-CA and DODE-LA $MAPbBr_3$ PQDs decreased to 76 and 79%, respectively. Interestingly, from the initial time to about 0.4 hours, the relative PL intensity of DODE-LA $MAPbBr_3$ PQDs decreased much faster than BUTY-VA and OCTY-CA $MAPbBr_3$ PQDs but then leveled off until the end of the experiment. This could be due to the formation of a stable size or species that DODE-LA ligands conform. PQDs are known to degrade by reacting with oxygen and water molecules in the air.[45] Consequently, these results indicate that increasing the capping ligand chain length from 4 carbon atoms to 8 or greater carbon atoms significantly improves the impermeability to oxygen and water molecules.

An additional stability test for each PQD was conducted in isopropanol solvent, as illustrated in **Figure 3.4.5b**. OCTY-CA $MAPbBr_3$ PQDs initially decreased in relative PL intensity at a slower rate than BUTY-VA and DODE-LA $MAPbBr_3$ PQDs but degraded to 16% in the final measurement. BUTY-VA $MAPbBr_3$ PQDs initially degraded at the fastest rate and ended with a relative PL intensity of 12%. DODE-LA

$MAPbBr_3$ PQDs also ended with the highest stability in this measurement as well with a relative PL intensity of 22%. However, as observed in air/dark stability test, DODE-LA $MAPbBr_3$ PQDs initially degraded faster than OCY-CA $MAPbBr_3$ PQDs. Therefore, it is possible that DODE-LA $MAPbBr_3$ PQDs conform to a more stable PQD overtime. Overall, these measurements confirm that stability is largely ligand length dependent. However, there is a much greater cost in stability from decreasing the ligand chain length from 8 carbon atoms to 4 carbon atoms compared to going from 12 carbon atoms to 8 carbon atoms.

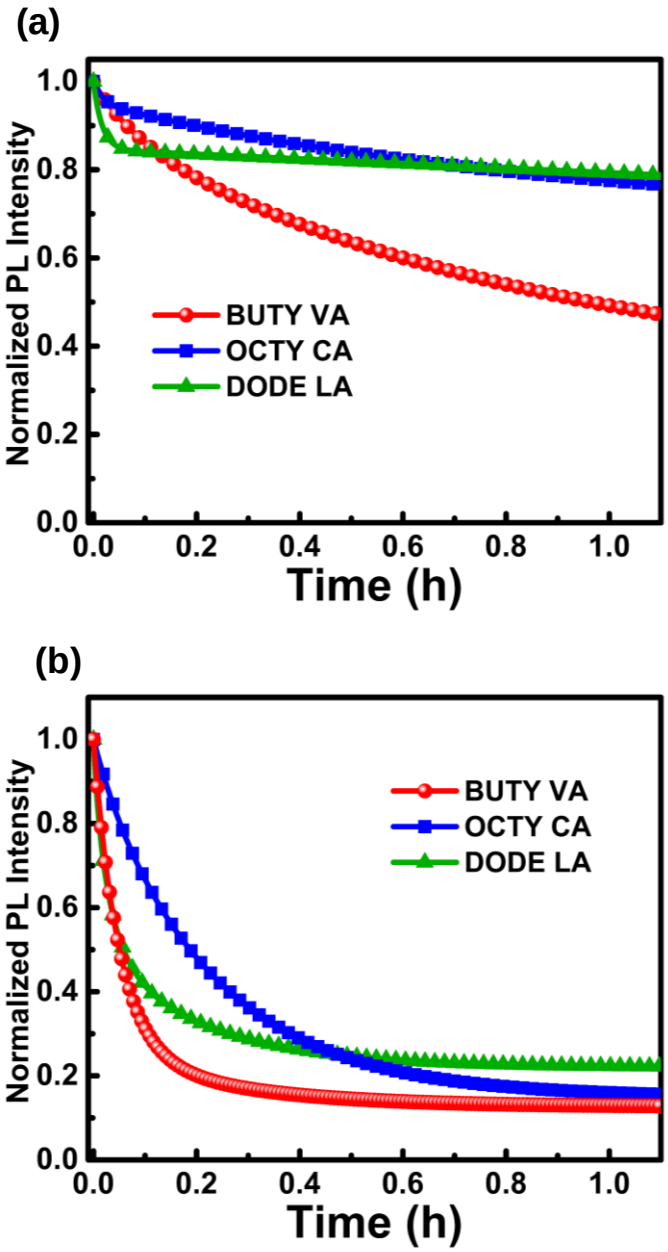

Figure 3.4.5. *The relative PL intensity versus time of BUTY-VA, OCTY-CA, and DODE-LA $MAPbBr_3$ PQDs under the conditions of (a) air and dark as well as (b) air, dark, and isopropanol solvent.*

3.4.3. Model of Charge Transport

Shown in **Figure 3.4.6** is a model to illustrate the charge transfer mechanisms in BUTY-VA, OCTY-CA, and DODE-LA $MAPbBr_3$ PQD films in an electrochemical cell. The space in which the ligands separate PQDs was estimated using C-C and C-N bond length. The surface to surface distance between PQDs passivated by DODE-LA ligands is up to 3.9 nm and the distance between the PQD surface and electrolyte at the interface is estimated to be 2.0 nm. The DODE-LA $MAPbBr_3$ PQD film did not show detectable charge transport in EIS measurements within the measured frequency range. This indicates that the inter-PQD distance is likely longer than what is needed for effective tunneling. The distance between PQDs passivated with OCTY-CA ligands is around 2.7 nm and the distance between the corresponding PQDs and electrolyte at the interfaces is around 1.3 nm. The inter-PQD distance for BUTY-VA passivated PQDs is about 1.5 nm and the PQD-electrolyte distance at the interfaces is around 0.7 nm. Based on these distances, the effective tunneling barrier, α, was calculated. For BUTY-VA and OCTY-CA $MAPbBr_3$ PQD films, the α value is about 0.035 $Å^{-1}$. In previous reports using gold electrodes for charge tunneling through an alkane barrier, α was found to be 0.35-1.0 $Å^{-1}$.[50-52] Due to low α value, similar to the α value of 0.028 $Å^{-1}$ for electron transfer in a porphyrin oligomer bridge,[53] the dominant charge transport mechanism may be charge tunneling rather than hopping. Additionally, in self-assembled conjugated molecular wires containing thiophene, the transition from tunneling to hopping has been reported to occur at 4 nm and greater.[54] Thus, we propose that charge tunneling is the dominant mechanism. The Butler-Volmer transfer factor (β) of charge tunneling at the PQD and electrolyte interface was calculated to be 0.36

and 0.31 for BUTY-VA and OCTY-CA $MAPbBr_3$ PQD film, respectively. Consistent with a previous report, CdSe QDs passivated with trioctylphosphine and oleic acid and linked by 3 to 2 carbon atom bifunctional linkers to a TiO_2 substrate were observed to have a β value of 0.38.[55] From the Butler-Volmer equation, an Arrhenius analysis was used to calculate the activation energy (E_a) for charge tunneling at the PQD and electrolyte interface. For BUTY-VA and OCTY-CA $MAPbBr_3$ PQD film, E_a is calculated to be 77 and 90 meV, respectively. These E_a values are similar for previously reported PbS QD films and CdTe/ZnTe QD films that contain hydrocarbon capping ligands, ranging from 34 to 127 meV.[56-59] Thus, decreasing the chain length of the PQD ligands from 8 carbon atoms to 4 carbon atoms enables 13 meV less energy for charge transport at the PQD film and electrolyte interface.

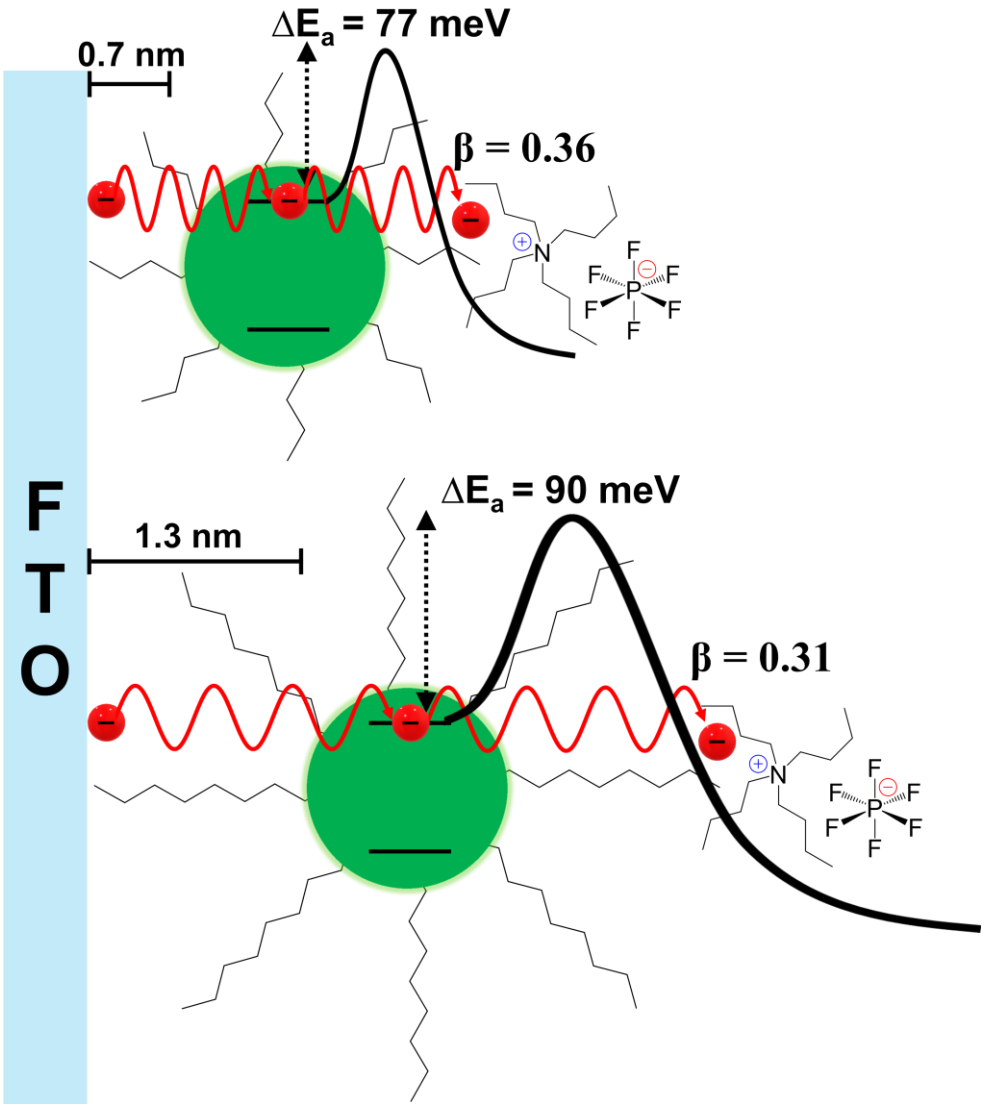

Figure 3.4.6. *Model of charge transport mechanisms in BUTY-VA and OCTY-CA MAPbBr$_3$ PQD film in an electrochemical cell. (β) is the Butler-Volmer transfer factor.*

3.5. Conclusions

In summary, conductivity, charge transport properties, photocurrent density, and stability of PQD films passivated with straight chain alkylamine and carboxylic acid ligands containing 4, 8 or 12 carbon atoms have been studied. EIS and transient photocurrent density measurements confirm that decreasing the ligand chain length can significantly increase the conductivity, charge transport, and photocurrent density of PQD solid film. The mechanism of charge transport is attributed primarily to tunneling based on the low distance dependent charge transfer decay α value of 0.035 $Å^{-1}$. Increasing the capping ligand chain length from 8 to 12 carbon atoms substantially diminishes the charge transport of PQD film compared to increasing the chain length from 4 to 8 carbon atoms. Hence, passivating PQDs with ligands containing 12 carbon atoms seems to increase the interdot spacing in PQD solid film and substantially decrease the probability of tunneling. A large difference in stability is found for the PQDs passivated with different chained length ligands, with the longer ones providing better stability than the shorter ones. On balance, passivating the surface of PQDs with a chain length of 8 carbon atoms (OCTY-CA ligand) can facilitate both electronic properties and stability of PQD solid film.

3.6. References

(1) P. Tonui, S. O. Oseni, G. Sharma, Q. Yan, and G. T. Mola, Renew. Sust. Energ. Rev. **91**, 1025 (2018).

(2) M. Istafaul Haque Ansari, A. Qurashi, and M. Khaja Nazeeruddin, J. Photoch. Photobio. C **35,** 1 (2018).

(3) Ho-Baillie, M. Zhang, C. F. J. Lau, F.-J. Ma, and S. Huang, Joule **3,** 938 (2019).

(4) U. Khan, Y. Zhinong, A. Ahmad Khan, A. Zulfiqar, and Q. Ullah Khan, Solar Energy **189,** 421 (2019).

(5) M. A. Green, and A. Ho-Baillie, ACS Energy Lett. **2**, 822 (2017).

(6) K. Jena, A. Kulkarni, and T. Miyasaka, Chem. Rev. **119**, 3036 (2019).

(7) Shi, L. Duan, Y. Zhao, J. Luo, and X. Zhang, Adv. Mater. 1806474 (2019).

(8) K. Wang, W. Siddique Subhani, Y. Wang, X. Zuo, H. Wang, L. Duan, and S. Liu, Adv. Mater. 1902037 (2019).

(9) Z. Shi, and A. H. Jayatissa, Materials **11**, 729 (2018).

(10) E. T. Vickers, T. A. Graham, A. H. Chowdhury, B. Bahrami, B. W. Dreskin, S. Lindley, S. Bonabi Naghadeh, Q. Qiao, and J. Z. Zhang, ACS Energy Lett. **3**, 2931 (2018).

(11) J. Dai, J. Xi, L. Li, J. Zhao, Y. Shi, W. Zhang, C. Ran, B. Jiao, X. Hou, X. Duan, and Z. Wu, Angew. Chem., Int. Ed. **57,** 5754 (2018).

(12) R. Kagan, and C. B. Murray, Nat. Nanotechnol. **10**, 1013 (2015).

(13) A. Hines, and P. V. Kamat, J. Phys. Chem. C **117**, 14418 (2013).

(14) A. Hines, and P. V. Kamat, ACS Appl. Mater. Interfaces **6,** 3041 (2014).

(15) Hoffman, J. B.; Alam, R.; Kamat, P. V. ACS Energy Lett. **2**, 391 (2017).

(16) H. J. Yun, J. Lim, A. S. Fuhr, N. S. Makarov, S. Keene, M. Law, J. M. Pietryga, and V. I. Klimov, ACS Nano **12**, 12587 (2018).

(17) Zheng, C. Bi, F. Huang, D. Binks, and J. Tian, ACS Appl. Mater. Interfaces **11**, 25410 (2019).

(18) P. N. Goswami, D. Mandal, and A. K. Rath, Nanoscale **10**, 1072 (2018).

(19) J. Xue, J.-W. Lee, Z. Dai, R. Wang, S. Nuryyeva, M. E. Liao, S.-Y. Chang, L. Meng, D. Meng, P. Sun, O. Lin, M. S. Goorsky, and Y. Yang, Joule **2**, 1866 (2018).

(20) Luo, S. Bonabi Naghadeh, and J. Z. Zhang, ChemNanoMat **3**, 456 (2017).

(21) S. Bonabi Naghadeh, B. Luo, G. Abdelmageed, Y.-C. Pu, C. Zhang, and J. Z. Zhang, J. Phys. Chem. C **122**, 15799 (2018).

(22) Niu, X. Guo, and L. Wang, J. Mater. Chem. A **3**, 8970 (2015).

(23) B. Luo, Y. C. Pu, S. A. Lindley, Y. Yang, L. Lu, Y. Li, X. Li, and J. Z. Zhang, Angew. Chem., Int. Ed. **55**, 8864 (2016).

(24) N. Marinova, M. Franckevicius, I. Matulaitiene, A. Devizis, G. Niaura, V. Gulbinas, and J. L. Delgado, ChemSusChem **10**, 3760 (2017).

(25) Abdelmageed, C. Mackeen, K. Hellier, L. Jewell, L. Seymour, M. Tingwald, F. Bridges, J. Z. Zhang, and S. Carter, Sol. Energy Mater. Sol. Cells **174**, 566 (2018).

(26) J. Pan, S. P. Sarmah, B. Murali, I. Dursun, W. Peng, M. R. Parida, J. Liu, L. Sinatra, N. Alyami, C. Zhao, E. Alarousu, T. K. Ng, B. S. Ooi, O. M. Bakr, and O. F. Mohammed, J. Phys. Chem. Lett. **6**, 5027 (2015).

(27) S. Huang, Z. Li, L. Kong, N. Zhu, A. Shan, and L. Li, J. Am. Chem. Soc. **138**, 5749 (2016).

(28) S. A. Veldhuis, Y. K. E. Tay, A. Bruno, S. S. H. Dintakurti, S. Bhaumik, S. K. Muduli, M. Li, N. Mathews, T. C. Sum, S. G. Mhaisalkar, Nano Lett. **17**, 7424 (2017).

(29) Abdelmageed, H. R. Sully, S. Bonabi Naghadeh, A. El-Hag Ali, S. A. Carter, J. Z. Zhang, ACS Appl. Energy Mater. **1**, 387 (2018).

(30) Y. Tan, Y. Zou, L. Wu, Q. Huang, D. Yang, M. Chen, M. Ban, C. Wu, T. Wu, S. Bai, T. Song, Q. Zhang, and B. Sun, ACS Appl. Mater. Interfaces **10**, 3784 (2018).

(31) F. Krieg, S. T. Ochsenbein, S. Yakunin, S. ten Brinck, P. Aellen, A. Süess, B. Clerc, D. Guggisberg, O. Nazarenko, Y. Shynkarenko, S. Kumar, C.-J. Shih, I. Infante, and M. V. Kovalenko, ACS Energy Lett. **3**, 641 (2018).

(32) M. A. Boles, D. Ling, T. Hyeon, and D. V. Talapin, Nat. Mater. **15**, 141 (2016).

(33) R. S. Dibbell, D. G. Youker, and D. F. Watson, J. Phys. Chem. C **113**, 18643 (2009).

(34) Zillner, S. Fengler, P. Niyamakom, F. Rauscher, K. Köhler, and T. Dittrich, J. Phys. Chem. C **116**, 16747 (2012).

(35) Dugay, P. Tan, M. Ibrahim, J. C. Garcia, L.-M. Lacroix, P.-F. Fazzini, G. Viau, and M. Respaud, Phys. Rev. B: Condens.

(36) Matter Mater. Phys. **89**, 041406 (2014).

(37) A. Chistyakov, M. A. Zvaigzne, V. R. Nikitenko, A. R. Tameev, I. L. Martynov, and O. V. Prezhdo, J. Phys. Chem. Lett. **8**, 4129 (2017).

(38) Chen, Q. Zhong, W. Chen, B. Sang, Y. Wang, T. Yang, Y. Liu, Y. Zhang, and H. Zhang, Adv. Funct. Mater. **29**, 1900991 (2019).

(39) Dugay, R. P. Tan, M. Ibrahim, C. Garcia, J. Carrey, L.-M. Lacroix, P.-F. Fazzini, G. Viau, and M. Respaud, Phys. Rev. B **89**, 041406(R) (2014).

(40) S. Kim, and M. G. Bawendi, J. Am. Chem. Soc. **125**, 14652 (2003).

(41) N. Kholmicheva, P. Moroz, H. Eckard, G. Jenson, and M. Zamkov, ACS Energy Lett. **2**, 154 (2017).

(42) F. Chou, and A. M. Dennis, Sensors **15**, 13288 (2015).

(43) Nakazawa, Y. Zhang, F. Liu, C. Ding, K. Hori, T. Toyoda, Y. Yao, Y. Zhou, S. Hayase, R. Wang, Z. Zou, Q. Shen, Nanoscale Horiz. **4**, 445 (2019).

(44) Y. C. Kim, K. H. Kim, D.-Y. Son, D.-N. Jeong, J.-Y. Seo, Y. S. Choi, I. T. Han, S. Y. Lee, and N. G. Park, Nature **550**, 87 (2017).

(45) B. F. Martinson, M. S. Goes, F. Fabregat-Santiago, J. Bisquert, M. J. Pellin, and J. T. Hupp, J. Phys. Chem. A **113**, 4015 (2009).

(46) S. Züfle, S. Altazin, A. Hofmann, L. Jäger, M. T. Neukom, W. Brütting, and B. Ruhstaller, J. Appl. Phys. **122**, 115502 (2017).

(47) K. Xu, E. T. Vickers, L. Rao, S. A. Lindley, A. C. Allen, B. Luo, X. Li, and J. Z. Zhang, Chem-Eur J. **25**, 5014 (2019).

(48) L. C. Schmidt, A. Pertegas, S. Gonzalez-Carrero, O. Malinkiewicz, S. Agouram, G. Minguez Espallargas, H. J. Bolink, R. E. Galian, and J. Perez-Prieto, J. Am. Chem. Soc. **136**, 850 (2014).

(49) J. K. Cooper, A. M. Franco, S. Gul, C. Corrado, J. Z. Zhang, Langmuir **27**, 8486 (2011).

(50) J. G. Son, E. Choi, Y. Piao, S. W. Han, T. G. Lee, Nanoscale **8,** 4573 (2016).

(51) J. L. Peters, K. H. W. van de Bos, S. Van Aert, B. Goris, S. Bals, D. Vanmaekelbergh, Chem. Mater. **29,** 4122 (2017).

(52) W. Wang, T. Lee, and M. A. Reed, J. Phys. Chem. B **108**, 18398 (2004).

(53) K. Wang, and B. Xu, Phys. Chem. Chem. Phys. **18**, 9569, (2016).

(54) Y. Qi, I. Ratera, J. Y. Park, P. D. Ashby, S. Y. Quek, J. B. Neaton, and M. Salmeron, Langmuir **24**, 2219 (2008).

(55) G. Gatty, A. Kahnt, L. J. Esdaile, M. Hutin, H. L. Anderson, and B. Albinsson, J. Phys. Chem. B **119**,

(56) 7598 (2015).

(57) E. Smith, S. O. Odoh, S. Ghosh, S. Ghosh, L. Gagliardi, C. J. Cramer, and C. D. Frisbie, J. Am. Chem. Soc. **137**, 15732 (2015).

(58) Mora-Seró, S. Giménez, T. Moehl, F. Fabregat-Santiago, T. Lana-Villareal, R. Gómez, and J. Bisquert, Nanotechnology **19**, 424007 (2008).

(59) J. Zhang, J. Tolentino, E. R. Smith, J. Zhang, M. C. Beard, A. J. Nozik, M. Law, and J. C. Johnson, J. Phys. Chem. C **118**, 16228 (2014).

(60) R. H. Gilmore, S. W. Winslow, E. M. Y. Lee, M. N. Ashner, K. G. Yager, A. P. Willard, and W. A. Tisdale, ACS Nano **12**, 7741 (2018).

(61) T. Nowozin, A. Wiengarten, L. Bonato, D. Bimberg, W.-H. Lin, S.-Y. Lin, M. N. Ajour, K. Daqrouq, and A. S. Balamesh, J. Nanotechnol. **2013**, 302647 (2013).

(62) H. S. Lee, K. H. Lee, J. C. Choi, and H. L. Park, Appl. Phys. Lett. **81**, 3720 (2002).

Chapter 4. Improving Charge Carrier Delocalization in Perovskite Quantum Dots by Surface Passivation with Conductive Aromatic Ligands

4.1. Abstract

Long-chain saturated hydrocarbons and alkoxysilanes are ligands that are commonly used to passivate perovskite quantum dots (PQDs) to enhance their stability and optical properties. However, the insulating nature of these capping ligands creates an electronic energy barrier and impedes interparticle electronic coupling, thereby limiting device applications. One strategy to solve this problem is to use short conductive aromatic ligands that allow delocalization of the electronic wave function from the PQDs, which, in turn, facilitates charge transport between PQDs by lowering the energy barrier. This is demonstrated with methylammonium lead bromide ($MAPbBr_3$) QDs prepared using benzylamine (BZA) and benzoic acid (BA) capping ligands. Optimized BZA-BA-$MAPbBr_3$ QDs are highly stable and show very high photoluminescence (PL) quantum yield (QY) (86%). More importantly, the BZA-BA-$MAPbBr_3$ QD film exhibits higher conductivity, carrier lifetime and more efficient charge extraction compared to PQDs with insulating ligands, as indicated by electrochemical measurements and transient photocurrent and photovoltage spectroscopy.

4.2. Introduction

Semiconductor quantum dots (QDs) are highly valued materials for optoelectronic applications because of their novel optical and electronic properties.[1-9] This is partly due to strong quantum confinement in the nanometer size regime.[10-12] In addition, their low-cost solution processing is a major advantage for device fabrication. Semiconductor QDs based on organo-metal halide perovskites with the formula $APbX_3$ (A = methylammonium (MA) or cesium, X = Cl, Br, I) have recently shown great promise for light-emitting diode (LED) and photovoltaic (PV) applications. However, one of the most important challenges hindering their practical use is instability in the presence of oxygen, moisture, temperature, and UV light.[13-22]

One approach for stabilizing the perovskite quantum dots (PQDs) is to use molecular ligands to passivate the surface, such as long alkyl chains and alkoxysilanes, that enhance optical properties and improve stability due to their hydrophobicity and steric hinderance towards infiltrating water and oxygen molecules.[8,9,17,20-29] However, these capping ligands are insulators and present energy barriers that obstruct charge carrier transport within the PQD solids. This not only inhibits charge transport at the interface of PQDs and conductive contact layers but also impedes PQD electronic coupling in solid film. In consequence, it is challenging to fabricate PQD films with enough light absorption and sufficient charge transport to compete with unprotected perovskite polycrystalline film or inorganic capped QDs.[30-35] A major focus towards increasing charge transport and interdot electronic coupling is tuning the length of the capping ligands.[36-40] This has led to the use of short ligands that contain multiple functional groups to passivate diverse defect sites and decrease the distance between QDs towards increasing charge transport in molecular electronic junctions.[41-47] In

addition, bifunctional aromatic capping ligands have been used as an effective tool for linking conductive contact film with QDs at their interfacial region as well as strengthening the coupling between QDs in solid film.[36,37,46,48-55] Furthermore, surface passivation of colloidal PQDs with conjugated aromatic capping ligands are previously reported, however, the conjugated ligands are used in conjunction with oleic acid.[56] Therefore, surface passivation of colloidal PQDs with exclusively conjugated capping ligands has yet to be established.

The problem of concurrently preventing moisture penetration and improving charge transport can be solved by introducing hydrophobic capping ligands with conductive properties. This enables water-resistivity as well as lower charge-resistivity in a PQD solid. Prospective capping ligands with hydrophobicity and conductive properties include aromatic, alkene, and alkyne compounds with an unhindered positive or negative terminal ion that will interact strongly with the ions of the perovskite lattice. Aromatic compounds are especially promising due to the special stability from its resonance delocalization of π-electrons. Coupled with stability, addition of electron donating and withdrawing groups to the aromatic system enables fine-tuning of its electronic structure and energy level alignment, which is essential for solar cell and LED device fabrication. Benzylamine has been previously used to passivate crystalline perovskite for solar cells.[57,58] Wang *et al.* surface-passivated formamidinium lead iodide ($FAPbI_3$) films with aniline, benzylamine, and phenethylamine and observed that benzylamine has the optimal steric arrangement in conjunction with the perovskite surface to block moisture and enhance stability.

Moreover, Zhou *et al.* observed highly efficient surface passivation of defect regions that suppressed thermal photoinduced degradation.

Herein, we introduce for the first time colloidal $MAPbBr_3$ QDs with only short conductive aromatic capping ligands. $MAPbBr_3$ QDs were successfully synthesized using benzylamine (BZA) and benzoic acid (BA) capping ligands. In the optimal synthesis, BZA-BA-$MAPbBr_3$ QDs are observed to have a high photoluminescence quantum yield (PLQY) of 86 ± 5 % (vs. fluorescein, 95%), indicative of a well-passivated surface. Moreover, transient photovoltage (TPV) and transient photocurrent (TPC) spectroscopy as well as electroanalytical measurements, such as electrochemical impedance spectroscopy (EIS) and cyclic voltammetry (CV), have provided evidence that BZA-BA-$MAPbBr_3$ QDs in solid film possesses highly desirable electrical properties compared to PQDs passivated with the commonly used insulating long alkyl chains and alkoxysilanes.

4.3. Experimental Section

4.3.1. Materials

All chemicals were used without further purification, which include: toluene (spectroscopic grade, Fisher Scientific), DMF (spectroscopic grade, Fisher Scientific), oleic acid (97%, Alfa Aesar), (3-aminopropyl)triethoxysilane (99%, Sigma-Aldrich), $PbBr_2$ (99.99%, Alfa Aesar), PbI_2 (99.99%, Alfa Aesar), MABr (greatcellsolar), MAI (greatcellsolar), benzylamine (99%, TCI) and benzoic acid (99%, Sigma-Aldrich).

4.3.2. BZA-BA-MAPbBr$_3$ QD Synthesis

$CH_3NH_3PbBr_3$ QDs were synthesized using a solvent reprecipitation method under ambient conditions. CH_3NH_3Br (80 µmol, 9.0 mg), $PbBr_2$ (0.20 mmol, 73 mg), benzoic acid (0.74 mmol, 90 mg), and 400 μL DMF was added to a borosilicate vial and the solution was sonicated until all solid dissolved. Then, benzylamine (0.10 mmol, 11 μL) was added, and the solution was sonicated again for 20 sec. 100 μL precursor solution was added at a medium rate to 5.0 mL toluene. The PQD solution was centrifuged at 4,000 rpm for 2 minutes and the brightly fluorescent liquid extracted. The liquid was further purified using cotton-plug filtration.

4.3.3. APTES-OA-MAPbBr$_3$ QD Synthesis

$CH_3NH_3PbBr_3$ QDs were synthesized using a solvent reprecipitation method under ambient conditions. CH_3NH_3Br (80 µmol, 9.0 mg), $PbBr_2$ (0.20 mmol, 73 mg), and 400 μL DMF were added to a borosilicate vial and the solution was sonicated until all solid dissolved. APTES (85 µmol, 20 µL) and OA (0.32 mmol, 100 μL) were then added and sonicated again until dissolved. 100 μL precursor solution was added at a medium rate to 5.0 mL toluene. The PQD solution was centrifuged at 4,000 rpm for 2 minutes and the brightly fluorescent liquid extracted. The liquid was further purified using cotton-plug filtration.

4.3.4. OCTA-OA-MAPbBr$_3$ QD Synthesis

$CH_3NH_3PbBr_3$ QDs were synthesized using a solvent reprecipitation method under ambient conditions. CH_3NH_3Br (80 µmol, 9.0 mg), $PbBr_2$ (0.20 mmol, 73 mg),

and 400 μL DMF were added to a borosilicate vial and the solution was sonicated until all solid dissolved. OCTA (91 µmol, 15 µL) and OA (0.32 mmol, 100 μL) were then added and sonicated again until dissolved. 100 μL precursor solution was added at a medium rate to 5.0 mL toluene. The PQD solution was centrifuged at 4,000 rpm for 2 minutes and the brightly fluorescent liquid extracted. The liquid was further purified using cotton-plug filtration.

4.3.5. UV-Vis Spectroscopy

Absorption spectra were measured with an Agilent Technologies Cary 60 UV-Vis spectrophotometer. UV-Vis absorption spectra of BZA-BA-$MAPbBr_3$, APTES-OA-$MAPbBr_3$, and OCTA-OA-$MAPbBr_3$ QD films are displayed in **Figure 4.3.1**.

4.3.6. Fluorescence Spectroscopy

Fluorescence spectra were measured using a HORIBA Jobin Yvon Fluoromax-3 spectrofluorometer. Fluorescence spectra of BZA-BA-$MAPbBr_3$, APTES-OA-$MAPbBr_3$, and OCTA-OA-$MAPbBr_3$ QD films are displayed in **Figure 4.3.1**.

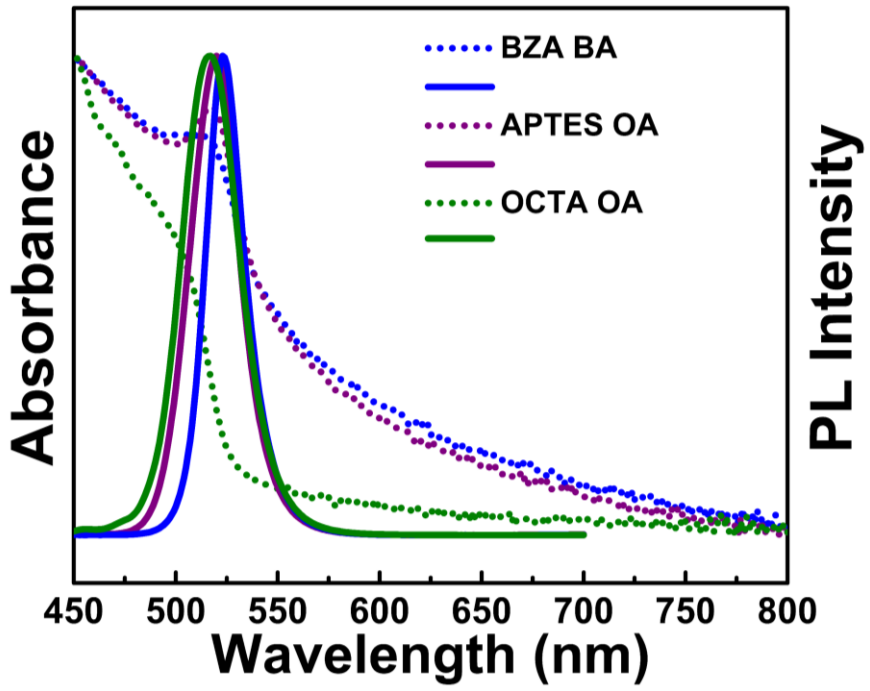

Figure 4.3.1. *UV-Vis and Fluorescence spectra of PQD films used in the EIS, CV, TPC, and TPV measurements. Dotted lines are Absorbance and solid lines*

4.3.7. X-Ray Diffraction Spectroscopy

XRD (Rigaku Americas Miniflex Plus powder diffractometer) analysis was used to obtain the crystalline phase at a voltage of 40 kV and current of 30 mA. The scanning angle range was 10–60° (2θ) with a rate of 3° min^{-1}.

4.3.8. Fourier-Transform Infrared Spectroscopy

FTIR spectra were obtained using a PerkinElmer Spectrum One FT-IR Spectrometer. **Figure 4.3.2** depicts the FTIR spectra of BZA free ligand, BZA-BA-$MAPbBr_3$ QDs, and $MAPbBr_3$ bulk in the 900-600 cm^{-1} range.

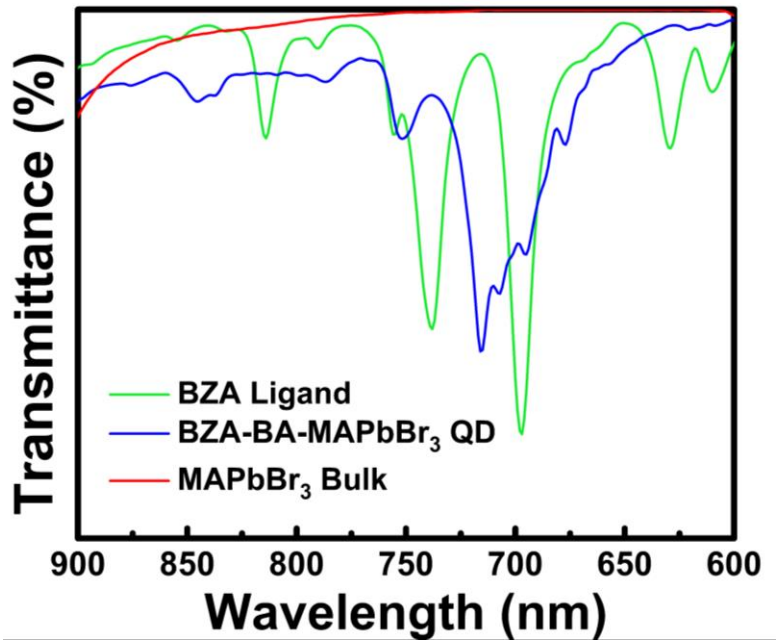

Figure 4.3.2. *FTIR spectra of BZA ligand, BZA-BA-$MAPbBr_3$ QD, and $MAPbBr_3$ bulk in the mono-substituted aromatic C-H bending region.*

4.3.9. Time-Correlated Single Photon Counting Spectroscopy

Time-resolved PL were taken at room temperature using a 200 MHz Ti:Sapphire laser (790-820 nm) with an output of 350 mW, which passed through a Conoptics pulse picker that was set to select 500 kHz pulse train and a BiBO crystal to generate a second harmonic pulse. The second harmonic pulse was centered at 405 nm (4.0 μJ) was used to excite the sample. The sample's emission was collected 90° using an ID100 avalanche photodiode. The instrument response function was determined to be 50 ps. Prepatterned ITO slides were cleaned by sonication in alconox solution (10% conc), deionized water, 2-propanol, and ethanol, respectively, for 15 min at 60 °C, and

then dried using compressed N_2 gas. Afterward, a TiO_2 sol−gel dense layer and mp-TiO_2 nanoparticles layer were each spin coated, respectively. Each TiO_2 layer was dried at 125 °C for 1 h and then sintered at 450 °C for 30 min in air. The TiO_2 sol−gel was prepared by mixing $Ti(OC_2H_5)_4$ with anhydrous ethanol, HCl, and deionized water as discussed in a previous study.[1] Films were fabricated by dripping concentrated (~30 OD at peak) PQD solution at 4,000 rpm onto ITO-TiO_2 substrate until an even and noticeable bright green film generated. PQD films were annealed at 70 ºC for exactly 2 minutes.

4.3.10. Electrochemical Impedance Spectroscopy Measurement

FTO substrates were first sonicated with liquinox solution for 10 minutes and rinsed with DI water, followed by sonication with DI water for 10 minutes and washed with isopropanol, followed by sonication with isopropanol for 10 minutes and washed with ethanol, and finally sonicated with ethanol for 10 minutes and dried with N_2. Next, the PQDs were spin-coated at 4,000 rpm. Films were fabricated by dripping concentrated (~30 OD at peak) PQD solution onto FTO substrate until an even and noticeable bright green film generated. BZA-BA-$MAPbBr_3$ QDs were spin-coated with more concentrated (~60 OD at peak) PQD solution in order to cast a thicker film than APTES-OA-$MAPbBr_3$ and OCTA-OA-$MAPbBr_3$ QDs. Films were annealed on a hot plate for 2 minutes at 70 °C. Film thickness was confirmed by imaging the cross-section using scanning electron microscopy (SEM). The spectroelectrochemical setup consists of a three-electrode cell (counter, reference, and working) in 0.10 M Bu_4NPF_6/dichloromethane solution connected to a potentiostat/galvanostat.[2] The

counter electrode was Pt wire and Ag/AgCl wire as pseudoreference electrode. The measurements were conducted in the frequency range of 1.0 MHz to 0.10 Hz at open circuit voltage. The lifetime of the charge transfer was calculated using the following Eq. (1):[3]

$$\tau = R_{ct} \times CPE$$

where τ is the lifetime, R_{ct} is the charge transport resistance obtained from the second x-intercept in the Nyquist plot (Figure 4), and *CPE* is the chemical capacitance described as a constant phase element obtained from the circuit fitting results. The charge mobility (μ) was calculated using Eq. (2):[4]

$$\mu = \frac{{L_d}^2 q}{kT\tau}$$

where L_d is the diffusion length obtained from a previous report,[5] q is electrical charge, k is Boltzmann constant, T is temperature, and τ is lifetime obtained from Eq. (1).

4.3.11. Cyclic Voltammetry Measurement

Cyclic voltammetry measurements were conducted under similar conditions as the EIS measurements. A ferrocene solution was placed in the working electrode cell (blank FTO substrate as the electrode) to determine a reference oxidation/reduction peak. The HOMO energy levels were calculated using the following Eq. (3):[6]

$$E_{HOMO} = -4.80 - E_{ox}$$

The band-gap was determined by calculating the λ_{onset} of the absorption spectra. The LUMO energy level was determined by Eq. (4):

$$E_{LUMO} = E_{HOMO} + E_g$$

4.3.12. Transient Photovoltage and Photocurrent Measurements

Agilent 5500 conductive atomic force microscopy (AFM) was used to measure local Transient photovoltage (TPV) and Transient photocurrent (TPC) decays in contact mode. A platinum/iridium coated silicon conductive tip (Budget Sensors ContE-G;force constant of 0.20 N/m; resonance frequency of 14 kHz) was placed on the surface of film and transient data were acquired by Agilent MSOX4154A oscilloscope. An Agilent Breakout Box (N9447A) was connected to oscilloscope for receiving signal from the AFM controller. Oscilloscope input impedance of 1.0 MΩ for TPV and 50 Ω for TPC were the parameters for collecting transient decays. A green laser pulse with 532 nm wavelength generated by MGL-I-532 DPSS was applied to excite charge carrier. A mono-exponential decay equation is used to calculate the carrier lifetime and transport time of the film Eq. (5):

$$X(t) = X_0 e^{-\frac{t}{\tau}}$$

4.3.13. References

(1) Arango, A. C.; Johnson, L. R.; Bliznyuk, V. N.; Schlesinger, Z.; Carter, S. A.; Hörhold, H. H. Efficient Titanium Oxide/Conjugated Polymer Photovoltaics for Solar Energy Conversion. *Adv. Mater.* **2000**, *12*, 1689−1692.

(2) Samu, G. F.; Scheidt, R. A.; Kamat, P. V.; Janáky, C. Electrochemistry and Spectroelectrochemistry of Lead Halide Perovskite Films: Materials Science Aspects and Boundary Conditions. *Chem. Mater.* **2018**, *30*, 561-569.

(3) Kim, Y. C.; Kim, K. H.; Son, D.-Y.; Jeong, D.-N.; Seo, J.-Y.; Choi, Y. S.; Han, I. T.; Lee, S. Y.; Park, N. G. Printable Organometallic Perovskite Enables Large-area, Low-dose X-ray Imaging. *Nature* **2017**, *550*, 87-91.

(4) Hodes, G.; Kamat, P. V. Understanding the Implication of Carrier Diffusion Length in Photovoltaic Cells. *J. Phys. Chem. Lett.* **2015**, *6*, 4090-4092.

(5) Zhumekenov, A. A.; Saidaminov, M. I.; Haque, M. A.; Alarousu, E.; Sarmah, S. P.; Murali, B.; Dursun, I. D.; Miao, X.-H.; Abdelhady, A. L.; Wu, T. et al. Formamidinium Lead Halide Perovskite Crystals with Unprecedented Long Carrier Dynamics and Diffusion Length. *ACS Energy Lett.* **2016**, *1*, 32-37.

(6) Zhang, W.; Zhu, R.; Ke, L.; Liu, X.; Liu, B.; Ramakrishna, S. Anatase Mesoporous TiO_2 Nanofibers with High Surface Area for Solid-state Dye-sensitized Solar Cells. *Small* **2010**, *6*, 2176-2182.

4.4. Results and Discussion

Methylammonium lead bromide quantum dots ($MAPbBr_3$) QDs were synthesized following a previously reported procedure.[20,59] A precursor solution consisting of $PbBr_2$, MABr, benzylamine (BZA), and benzoic acid (BA) dissolved in N,N-dimethylformamide (DMF) was injected into toluene. The colloidal BZA-BA-$MAPbBr_3$ QD solution was then purified using centrifugation and cotton-plug filtration. Optimization of PQDs with the highest quantum yield (QY) was determined by adjusting BZA and BA concentrations discretely. Detailed information about the synthesis is in the experimental section. The highest relative QY obtained from BZA-BA-$MAPbBr_3$ QDs is 86% (vs. fluorescein, 95%). The UV-Vis absorption and

photoluminescence (PL) spectra of BZA-BA-$MAPbBr_3$ QDs are displayed in **Figure 4.4.1a**. As shown, the BZA-BA-$MAPbBr_3$ QDs exhibited a strong absorption peak at 520 nm and slight stokes shift in PL at 525 nm. The full-width half-maximum (FWHM) of the PL band from these PQDs is 27 nm. $MAPbBr_3$ QDs containing the insulating capping ligands (3-aminopropyl)triethoxysilane (APTES) and oleic acid (OA) as well as octylamine (OCTA) and OA were also synthesized according to the literature in order to compare with the BZA-BA-$MAPbBr_3$ QDs.[20,60] **Figure 4.4.1b,c** correspond to the UV-Vis absorption and PL spectra of the APTES-OA-$MAPbBr_3$ and OCTA-OA-$MAPbBr_3$ QDs, respectively. The APTES-OA-$MAPbBr_3$ QDs have a sharp exciton absorption peak at 520 nm and PL peak at 523 nm, while the OCTA-OA-$MAPbBr_3$ QDs have a much broader absorption band centered at 496 nm and PL peak at 514 nm. The FWHM of the PL band from APTES-OA-$MAPbBr_3$ QDs is 25 nm, while OCTA-OA-$MAPbBr_3$ QDs is 33 nm. The PLQY (vs. fluorescein, 95%) was calculated to be 46% and 71% for APTES-OA-$MAPbBr_3$ and OCTA-OA- $MAPbBr_3$ QDs, respectively, which is very similar to previously reported values.[20,56,60] In comparison, the PLQY values for the PQDs passivated with insulating ligands are lower than the PQDs with BZA/BA aromatic capping ligands, which is at 86%. We suggest that the difference in PLQY is less determined by the difference in the effect of spatial quantum confinement due to the different ligands or particle size, but more related to the density of trap states of the PQDs that is critically influenced by the effectiveness of passivation by the ligands.

To determine the size and shape of the PQDs, transmission electron microscopy (TEM) measurements were conducted, with images shown in **Figure 4.4.1d,e,f**. The

average diameter of the BZA-BA-$MAPbBr_3$, APTES-OA-$MAPbBr_3$ and OCTA-OA-$MAPbBr_3$ QDs are 6.3 ± 1.2 nm, 6.8 ± 1.1 nm, and 3.8 ± 0.9 nm, respectively. High-resolution TEM (HRTEM) was used to determine the lattice spacing of BZA-BA-$MAPbBr_3$ QDs. As shown in the lower left inset of Figure 1d, a lattice space of 0.28 nm was observed. This is an indication that the (002) crystal face of cubic $CH_3NH_3PbBr_3$ exists within the crystal lattice structure.[61] For further verification of the perovskite cubic phase presence, X-ray diffraction (XRD) was used to determine the QD crystal structure, as displayed in the upper left inset of Figure 1d. XRD peaks at 14.82°, 21.21°, 26.65°, 30.08°, 33.76°, 37.05°, 43.14°, 45.89°, 48.49°, 53.48°, 55.89°, and 58.24° indicates crystal planes assigned to the cubic phase of $MAPbBr_3$ perovskite, confirming its formation.[61]

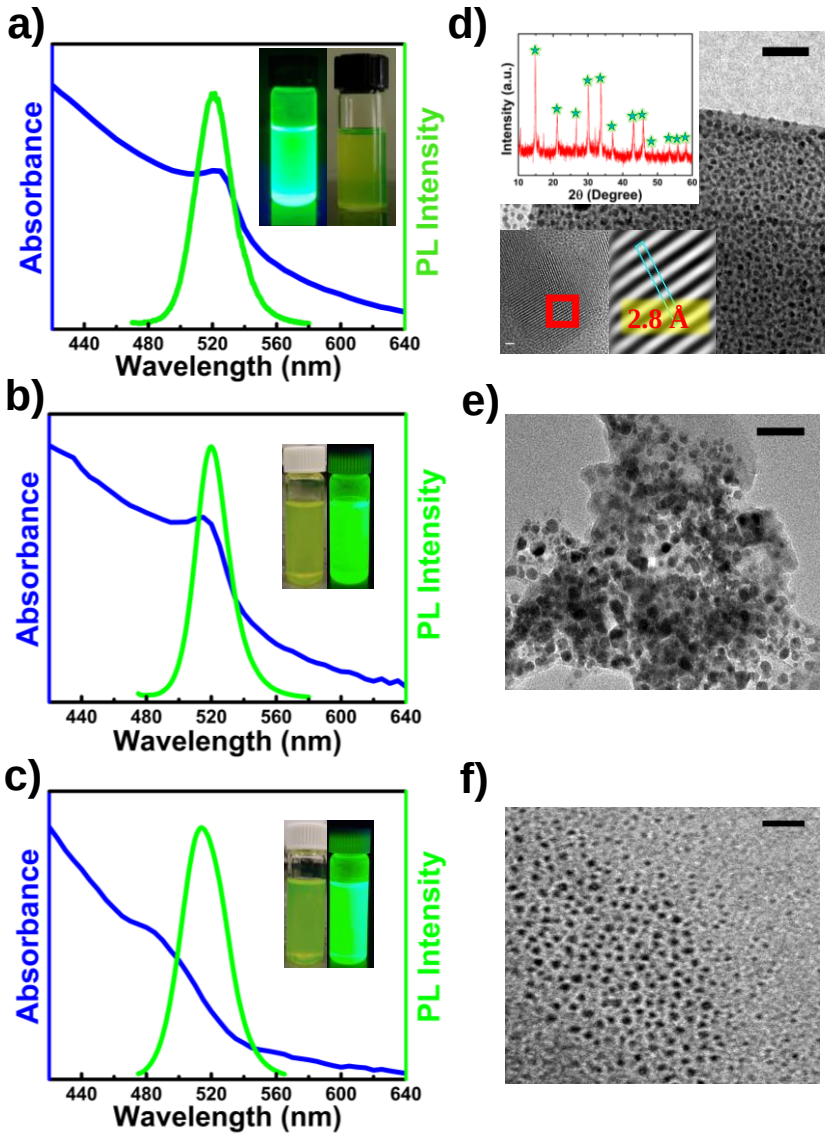

Figure 4.4.1. *UV-Vis absorption and PL spectra of (a) BZA-BA-MAPbBr$_3$, (b) APTES-OA-MAPbBr$_3$ and (c) OCTA-OA-MAPbBr$_3$ QDs. Inset is digital photograph of respective QD solution. (d) TEM image of BZA-BA-MAPbBr$_3$ QDs (scale bar 50 nm), lower left inset is HRTEM image with lattice spacing (scale bar 1 nm), and upper right inset is XRD with symbols assigned to the cubic phase. (e) TEM image of APTES-OA-MAPbBr$_3$ (scale bar 50 nm) and (f) OCTA-OA-MAPbBr$_3$ QDs (scale bar 20 nm).*

To elucidate the organic surface layer of the PQDs, FTIR spectroscopy was employed to probe its capping ligand composition. For BZA-BA-$MAPbBr_3$ QDs, a weak peak at 3398 cm^{-1} is observed, indicating the presence of primary N-H stretching, as shown in **Figure 4.4.2a**. As presented in **Figure 4.4.2b,c**, stronger N–H stretching from BZA free ligand and $MAPbBr_3$ bulk occurs at 3291 cm^{-1} and 3478 cm^{-1}, respectively. In the 3100-3000 cm^{-1} region, where aromatic C–H stretching occurs, three peaks at 3064, 3056, and 3028 cm^{-1} are observed for BZA-BA-$MAPbBr_3$ QDs, while three sharper peaks at 3085, 3065, and 3032 cm^{-1} are observed in BZA free ligand. This shift in aromatic C–H stretching from BZA free ligand to BZA-BA-$MAPbBr_3$ QDs provides evidence of ligand binding and change in vibrational modes from the unbound to bound states of the benzylamine molecule on the perovskite crystal lattice. Only one very strong and broad peak is observed for $MAPbBr_3$ bulk in this region, which corresponds to an ammonium salt. In addition, several aromatic C=C stretching and amine N–H bending are expected to be in the 1700-1500 cm^{-1} for BZA-BA-$MAPbBr_3$ QDs, BZA free ligand, and $MAPbBr_3$ bulk, however, the region is too complex to distinguish. The most evident peaks for the presence of mono-substituted aromatic compounds are in the 770-730 cm^{-1} and 720-680 cm^{-1} region, where strong aromatic C-H bending peaks at 752 cm^{-1} and 715 cm^{-1} are detected for BZA-BA-$MAPbBr_3$ QDs and peaks at 738 cm^{-1} and 697 cm^{-1} for BZA free ligand. Further detail in this region is illustrated in Figure S2. The $MAPbBr_3$ bulk contains no peaks in this region. In addition to the shift, as in the aromatic C-H stretching, the two aromatic C-H bending peaks are much broader in the BZA-BA-$MAPbBr_3$ QD FTIR spectra compared to BZA free ligand, which may reflect upon a change in vibrational modes,

lifetime of vibrational states, and/or higher variety of vibrational modes from being bound in inhomogeneous positions on the $MAPbBr_3$ crystal lattice.

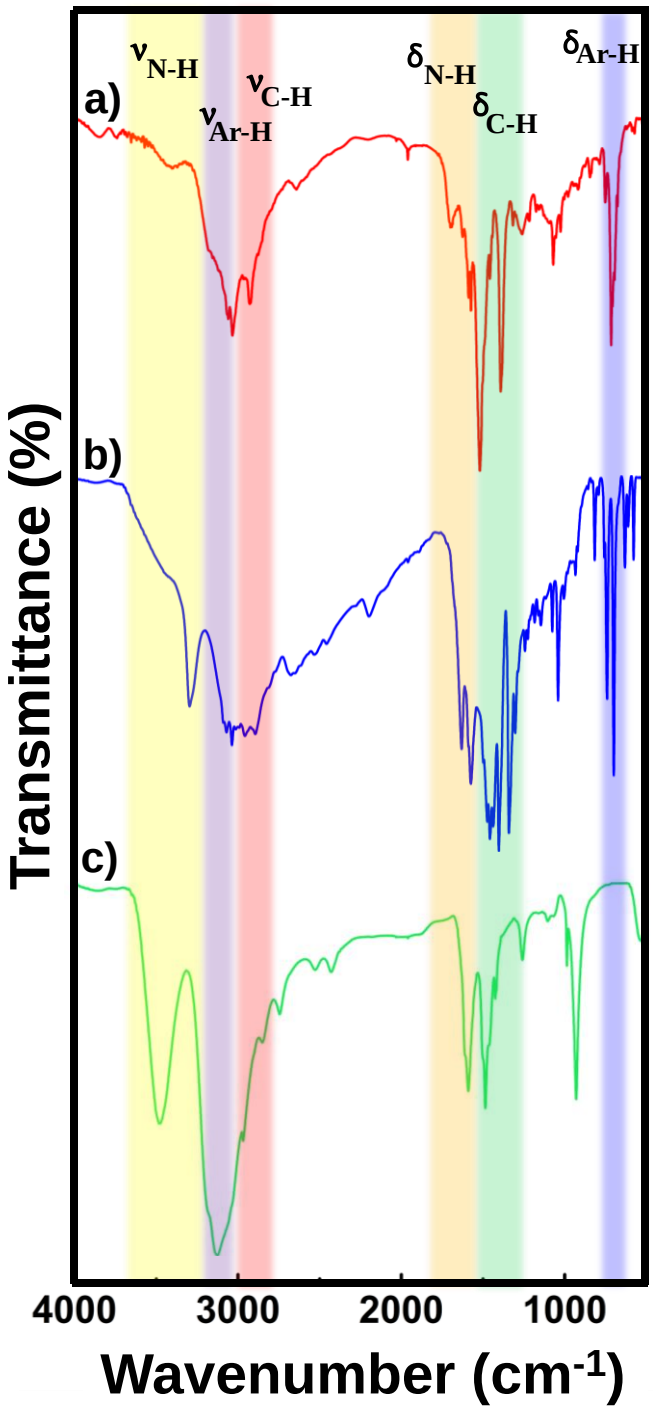

Figure 4.4.2. *FT-IR spectra of (a) BZA-BA-$MAPbBr_3$ QDs, (b) BZA free ligand, and (c) $MAPbBr_3$ bulk.*

To investigate photogenerated charge carrier dynamics, time-correlated single photon counting (TCSPC) was used to measure the fluorescence lifetime of $MAPbBr_3$ QD solid film, as shown in **Figure 4.4.3**. Detail of the measurement is described in the experimental section. The fluorescence decays were fitted using a double exponential function:

$$L = A_1 \exp(-t/\tau_1) + A_2 \exp(-t/\tau_2)$$

The $MAPbBr_3$ QDs were casted into a solid film on insulating borosilicate glass as well as TiO_2 as a compact/mesoporous electron transporting material on conductive indium tin oxide (ITO) substrate to determine whether there is quenching of photogenerated free carriers due to charge collection. Depopulation of photogenerated carriers as a result of charge collection from the conductive substrate is elucidated in the observed change in rate and amplitude of the fast and slow decay components derived from the fitted double exponential function.[62-64] A shorter lifetime and larger amplitude of the fast component reflects effective extraction of photogenerated charge carriers. As shown in **Figure 4.4.3a**, the BZA-BA-$MAPbBr_3$ QD sample casted on the insulating borosilicate glass contains a fast decay component (τ_1) of 2.92 ns that contributes 48% to the total amplitude and a slow component (τ_2) of 21.9 ns with 52% contribution. While on the ITO-TiO_2 substrate, the fast component is 0.64 ns with 79% of the total amplitude and the slow component is 11.3 ns with a 21% total amplitude. The decrease in photogenerated charge carrier lifetime is indicative of more effective charge transfer and transport. For the APTES-OA-$MAPbBr_3$ QDs, as presented in **Figure 4.4.3b**, the fast decay component became slightly shorter from 1.24 ns on borosilicate to 0.77 ns on ITO-TiO_2 substrate, while the lifetime of the slow component remained almost the

same. In addition, the fast component becomes more dominant in relative amplitude, which may indicate increased quenching or charge transport of photogenerated free carriers. The OCTA-OA-$MAPbBr_3$ QDs, as shown in **Figure 4.4.3c**, follows a similar trend observed in the APTES-OA-$MAPbBr_3$ QDs. The lifetime of the fast decay slightly decreased from 1.41 ns on borosilicate to 0.51 ns on ITO-TiO_2, while the longer lifetime did not change significantly. The following equation was used to calculate the average photogenerated charge carrier lifetime of the $MAPbBr_3$ QDs:

$$\langle \tau \rangle = \frac{A_1 {\tau_1}^2 + A_2 {\tau_2}^2}{A_1 \tau_1 + A_2 \tau_2}$$

The average lifetime of the $MAPbBr_3$ QDs on conductive ITO-TiO_2 and insulating borosilicate glass was used to determine the electron transfer rate constant (K_{et}) from the equation:[65-67]

$$K_{et} = \frac{1}{\tau_{(PQD+TiO_2)}} - \frac{1}{\tau_{(PQD)}}$$

where $\tau_{(PQD+TiO2)}$ and $\tau_{(PQD)}$ are the fluorescence decay on ITO-TiO_2 and borosilicate substrate, respectively. For BZA-BA-$MAPbBr_3$, APTES-OA-$MAPbBr_3$, and OCTA-OA-$MAPbBr_3$ QDs, the electron injection rate constants are calculated to be 55.7, 4.35, and 1.99 μs^{-1}, respectively. Accordingly, passivating $MAPbBr_3$ QDs with BZA and BA compared to APTES and OA as well as OCTA and OA has improved the electron injection rate by more than 6-fold and 2-fold, respectively.

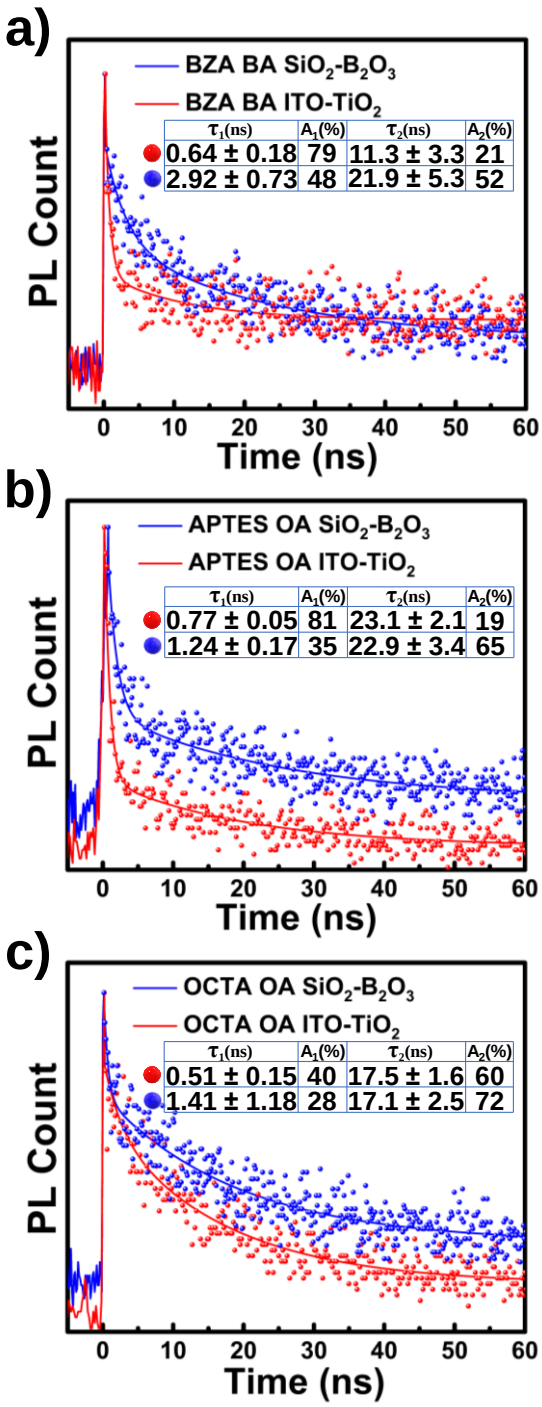

Figure 4.4.3. *Time-resolved PL spectra of (a) BZA-BA-$MAPbBr_3$, (b) APTES-OA-$MAPbBr_3$, and (c) OCTA-OA-$MAPbBr_3$ QDs on SiO_2-B_2O_3 and ITO-TiO_2.*

For further characterization, the charge transport properties of the PQDs passivated with conductive aromatic ligands were examined by electrochemical impedance spectroscopy (EIS). The EIS measurements were carried out on fluorine doped tin oxide (FTO) glass with films of $MAPbBr_3$ QDs and taken in the frequency range between 1 MHz and 0.1 Hz at open circuit voltage. Further detail of the EIS measurement is found in the experimental section. **Figure 4.4.4a** shows the Nyquist spectra of the different PQD films with the equivalent circuit in the inset, and **Figure 4.4.4b** displays the film thickness of each PQD used in EIS measurements. Increasing the thickness-to-surface area ratio will increase the impedance of the film.[68] Even with a thicker film (1.64 μm), BZA-BA-$MAPbBr_3$ QDs are observed to have a lower impedance compared to APTES-OA-$MAPbBr_3$ (542 nm) and OCTA-OA-$MAPbBr_3$ (792 nm) QD films. This supports the conclusion that the films composed of PQDs with conjugated ligands are more conductive. In the Nyquist spectra, the first intercept of the semicircle on the real axis from **Figure 4.4.4a** corresponds to the series resistance (R_s). Compared to the other two PQD solid films, APTES-OA-$MAPbBr_3$ and OCTA-OA-$MAPbBr_3$, with R_s values of 35.0 Ω and 36.8 Ω, respectively, the BZA-BA-$MAPbBr_3$ QD solid film has less series resistance with a R_s value of 28.6 Ω. The mechanism in the EIS measurement is reduction of PQD film from electron transport in the FTO working electrode, therefore, the R_s is highly dependent on the interaction between the PQD film and FTO substrate. The conductive aromatic capping ligands with sp^2 bond hybridization and electron delocalization, allows sufficient electron cloud overlap with the PQD core, which can explain the lower series resistance compared to the other PQD films with insulating capping ligands. The second intercept

in the Nyquist spectra represents the charge transfer (R_{CT}) ability of the material, which is heavily dependent on the interaction of the electrolyte used in the measurement. Tetra-n-butylammonium hexafluorophosphate (Bu_4NPF_6) electrolyte was used in a similar spectroelectrochemical setup previously reported for PQDs.[69] This electrolyte contains hydrophobic butyl-alkyl groups that interact favorably with the hydrophobic ligands, such as OCTA, APTES, OA, BZA, and BA through London dispersion forces. In addition, the hydrophobic electrolyte disfavors the polar FTO glass. As a result, the charge transfer from the FTO to the electrolyte is a much slower process with an R_{CT} of 102 Ω. BZA-BA-$MAPbBr_3$ QD film not only has the lowest R_s but also the lowest R_{CT} at 61.0 Ω, compared to APTES-OA-$MAPbBr_3$ QD film at 87.6 Ω and OCTA-OA-$MAPbBr_3$ QD film at 66.9 Ω. To qualitatively compare the BZA-BA-$MAPbBr_3$, APTES-OA-$MAPbBr_3$, and OCTA-OA-$MAPbBr_3$ QD films, the lifetime of the charge transfer was calculated to be 0.6, 4.4, and 3.2 ms, respectively.[70] In addition, the charge mobility (μ) was calculated using the above lifetimes and the diffusion length (L_d) of a previously reported $MAPbBr_3$ film,[71,72] which turn out to be 0.01197, 0.001640, and 0.002258 $cm^2\ V^{-1}\ s^{-1}$ for the three samples, respectively (details in the experimental section). Overall, these measurements and calculations have provided evidence that the conductive aromatic ligands enhance the conductivity and charge transport of the QD film.

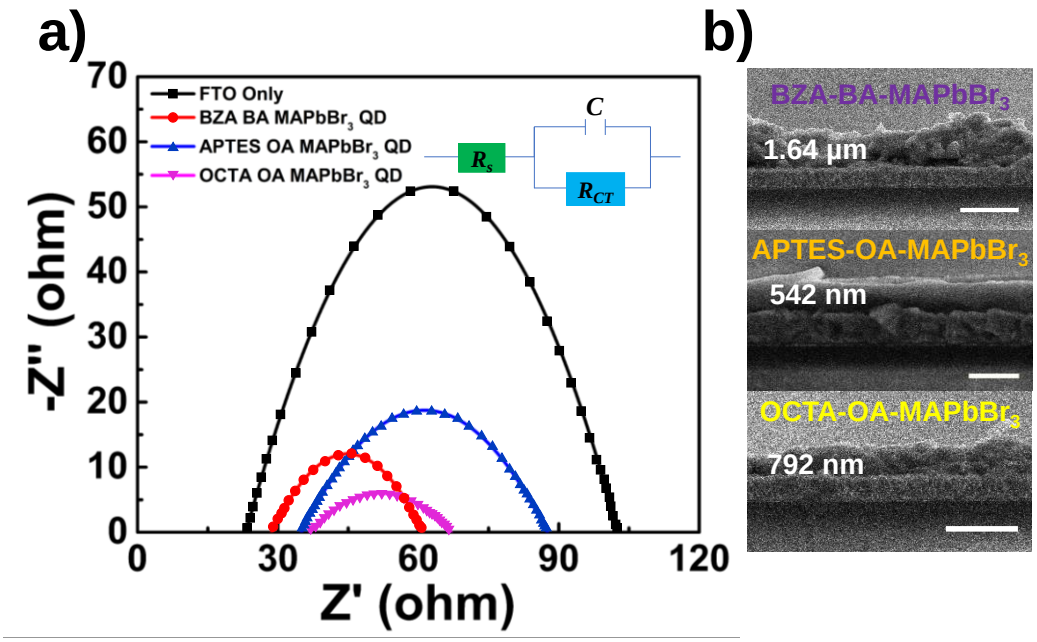

Figure 4.4.4. *(a) Electrochemical impedance responses of FTO without film deposited, BZA-BA-MAPbBr$_3$, APTES-OA-MAPbBr$_3$, and OCTA-OA-MAPbBr$_3$ QD film deposited. (b) Cross-sectional SEM images of the different QD film deposits used for EIS measurements. Scale bars represent 2, 1, and 1 μm, respectively.*

To substantiate PQD film reduction in the EIS measurements and examine the redox activity of the BZA-BA-MAPbBr$_3$, APTES-OA-MAPbBr$_3$, and OCTA-OA-MAPbBr$_3$ QD films, cyclic voltammetry (CV) measurements were conducted. As shown in **Figure 4.4.5**, only minor change in current density is observed with FTO substrate as the electrode compared to CV measurements with PQD film deposit. In addition, the positive and negative potential sweeps show the current density increases higher in BZA-BA-MAPbBr$_3$ QD film, as depicted in **Figure 4.4.5a**, compared to the

APTES-OA-$MAPbBr_3$ and OCTA-OA-$MAPbBr_3$ QD films shown in **Figure 4.4.5b,c,** respectively. Comparing area under the curve, which is the power per active surface area of electrode, BZA-BA-$MAPbBr_3$ QD film is 1.6 and 2.7 times higher than APTES-OA-$MAPbBr_3$ and OCTA-OA-$MAPbBr_3$ QD film, respectively.

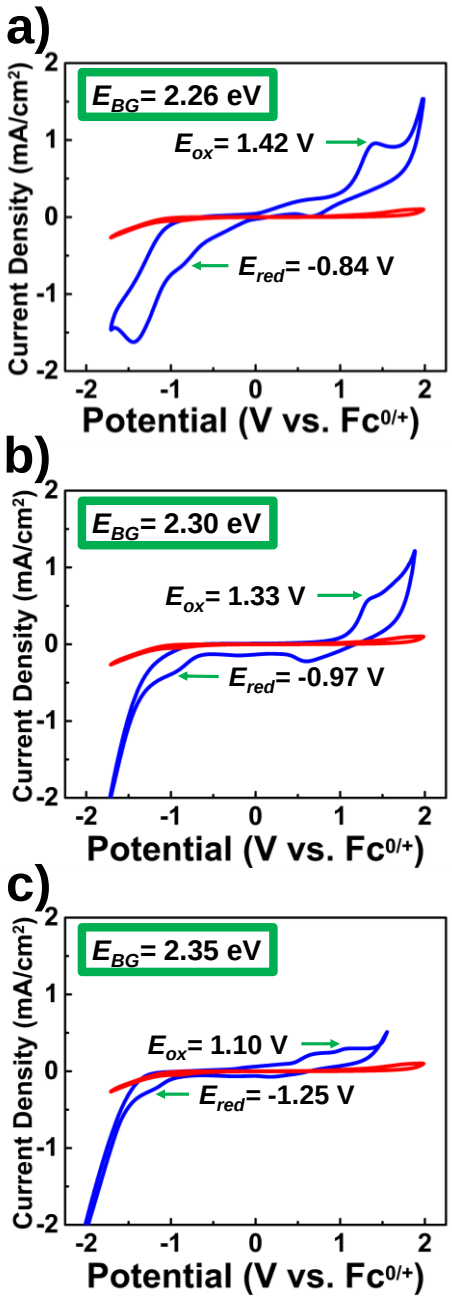

Figure 4.4.5. *Cyclic voltammograms of (a) BZA-BA-MAPbBr$_3$, (b) APTES-OA-MAPbBr$_3$, and (c) OCTA-OA-MAPbBr$_3$ QD film. FTO electrode with QD film deposit is represented by the blue line and FTO without QD film is in red.*

From specific oxidation and reduction peaks in the CV diagram, bandgap energy values are calculated to be 2.26, 2.30, and 2.35 eV, for BZA-BA-$MAPbBr_3$, APTES-OA-$MAPbBr_3$, and OCTA-OA-$MAPbBr_3$ QD films, respectively. These values are in good agreement based on the bandgap energies calculated from the UV-Vis absorption spectra (**Figure 4.3.1**), which are 2.25, 2.33, and 2.32 eV, respectively. Using the oxidation and reduction peaks corresponding to the band energies referenced to an internal standard (ferrocene/ferrocenium), the HOMO and LUMO energy levels were calculated. For OCTA-OA-$MAPbBr_3$ QDs the energy levels are -3.55 eV LUMO and -5.90 eV HOMO. For BZA-BA-$MAPbBr_3$ QDs the LUMO energy level is lower at -3.96 eV as well as the HOMO energy level at -6.22 eV. This result could be due to an inductive effect, where the more electronegative sp^2 carbon atoms in the ligands are drawing more electron density away from the perovskite lattice, and thus, lowering the LUMO energy level. Furthermore, APTES-OA-$MAPbBr_3$ QDs may have the same effect as the APTES ligand has electronegative oxygen atoms. The calculated HOMO energy level for these PQDs is -6.13 eV and the LUMO is -3.83 eV. Considering the work function of FTO substrate, which has been reported to be between -5.0 and -4.4 eV,[73] the BZA-BA-$MAPbBr_3$ QDs have a more favorable LUMO energy level for electron transport than OCTA-OA-$MAPbBr_3$ QDs. However, APTES-OA-$MAPbBr_3$ QDs have a very similar LUMO to BZA-BA-$MAPbBr_3$ QDs and yet still show a paralleled performance with OCTA-OA-$MAPbBr_3$ QDs in EIS and CV measurements. Therefore, it is concluded that the energy level alignment in the PQD films with the FTO substrate did not significantly impact these electrochemical measurements,

although, to some extent favors BZA-BA-$MAPbBr_3$ and APTES-OA-$MAPbBr_3$ QDs over OCTA-OA-$MAPbBr_3$ QDs.

To provide further evidence of improved electrical properties from PQDs passivated with conductive aromatic ligands, local transient photocurrent (TPC) and transient photovoltage (TPV) decays were measured using conductive atomic force microscopy (AFM). Details of the TPC and TPV measurements are in the experimental section. As shown from the AFM topography images in **Figure 4.4.6a,b,c**, a 100 nm by 100 nm area identified as the red square with similar film thickness was measured for BZA-BA-$MAPbBr_3$, APTES-OA-$MAPbBr_3$, and OCTA-OA-$MAPbBr_3$ QD solid film on FTO substrate. The charge transport time, recorded from TPC, corresponds directly to the conductivity and charge mobility of the material. TPC decay curves are displayed in **Figure 4.4.6d**. Charge transport lifetimes of 1.52, 2.15, and 1.97 μs were measured for BZA-BA-$MAPbBr_3$, APTES-OA-$MAPbBr_3$, and OCTA-OA-$MAPbBr_3$ QD films, respectively. Therefore, BZA-BA-$MAPbBr_3$ QDs outperforms the PQDs with insulating capping ligands since charges are able to travel faster through the PQD layer between the two electrodes. To analyze the charge recombination behavior of the PQD solid films, the charge carrier lifetime was measured by TPV. A longer charge carrier lifetime signifies a slower rate of recombination, and therefore, more efficient charge extraction. The TPV decay curves, as depicted in **Figure 4.4.6e**, translate to 2.92, 2.43, and 2.28 μs charge carrier lifetimes for BZA-BA-$MAPbBr_3$, APTES-OA-$MAPbBr_3$, and OCTA-OA-$MAPbBr_3$ QDs, respectively. BZA-BA-$MAPbBr_3$ QDs not only have a faster charge transport time but also a slower charge carrier lifetime, which is desired for device applications that rely on efficient charge transport and extraction.

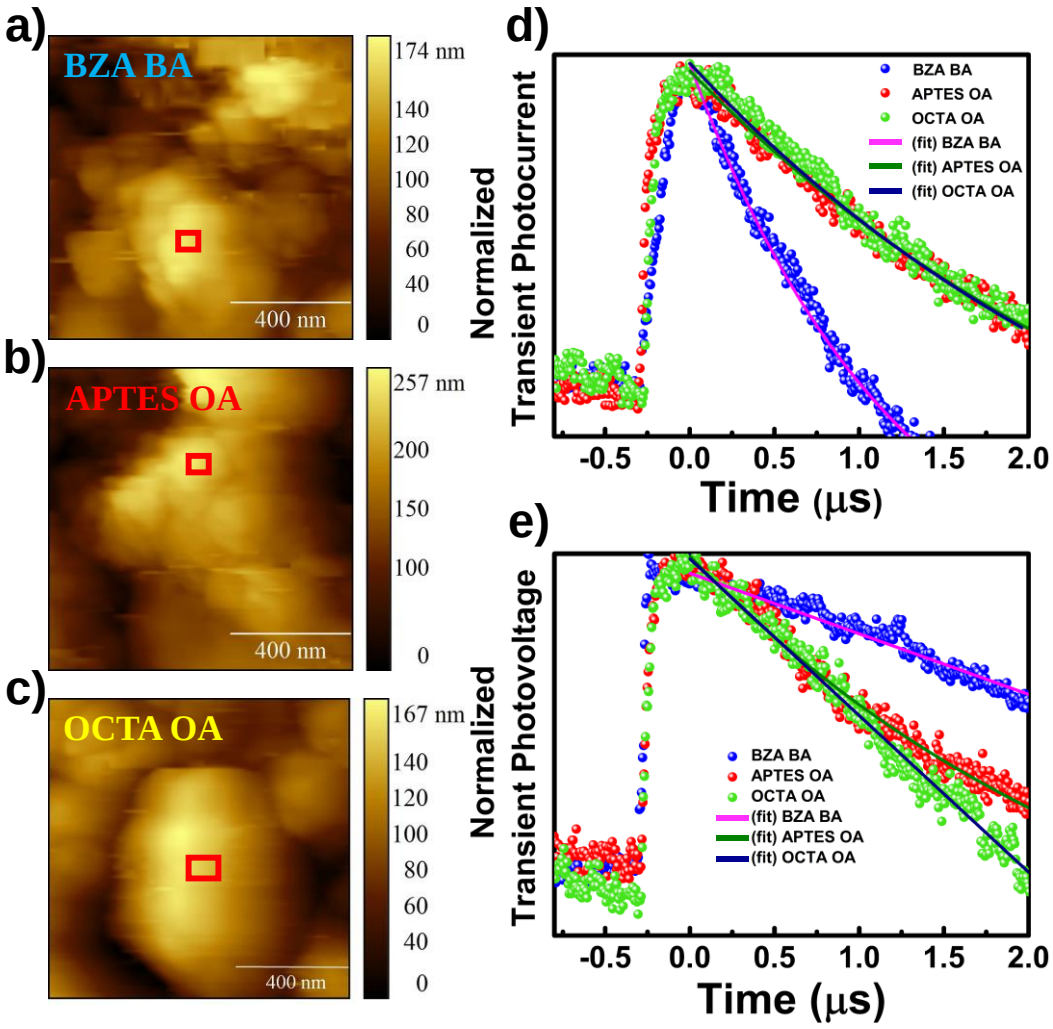

Figure 4.4.6. *AFM topography images of (a) BZA-BA-MAPbBr$_3$, (b) APTES-OA-MAPbBr$_3$, and (c) OCTA-OA-MAPbBr$_3$ PQD films. Red square indicates area measured. (d) Normalized TPC decay curve and (e) normalized TPV decay curve from the corresponding PQDs.*

4.5. Conclusion

In summary, we report the synthesis and characterization of MAPbBr$_3$ QDs surface-passivated with conductive aromatic capping ligands, benzylamine and

benzoic acid. The BZA-BA-$MAPbBr_3$ QDs are observed to have a high PLQY of 86%. In addition, compared to PQDs with insulating capping ligands, BZA-BA-$MAPbBr_3$ QDs demonstrated higher conductivity based on EIS and TPC measurements, and longer charge carrier lifetime based on TPV measurements. Furthermore, using cyclic voltammetry, it is shown BZA-BA-$MAPbBr_3$ QD film generates much greater current density than APTES-OA-$MAPbBr_3$ and OCTA-OA-$MAPbBr_3$ QD film. The combination of high PLQY of the colloidal PQDs in solution, which usually correlates to lower trap density,[74-77] and improved electrical/electronic properties of the PQD film is desirable for potential optoelectronic device applications.

4.6. References

(1) Kamat, P. V. Meeting the Clean Energy Demand: Nanostructure Architectures for Solar Energy Conversion. *J. Phys. Chem. C* **2007**, *111*, 2834-2860.

(2) Kamat, P. V. Quantum Dot Solar Cells. Semiconductor Nanocrystals as Light Harvesters. *J. Phys. Chem. C* **2008**, *112*, 18737-18753.

(3) Kamat, P. V. Quantum Dot Solar Cells. The *Next Big Thing* in Photovoltaics. *J. Phys. Chem. Lett.* **2013**, *4*, 908-918.

(4) Murray, C. B.; Kagan, C. R. Charge Transport in Strongly Coupled Quantum Dot Solids. *Nat. Nanotechnol.* **2015**, *10*, 1013-1026.

(5) Carey, G. H.; Abdelhady, A. L.; Ning, Z.; Thon, S. M.; Bakr, O. M.; Sargent, E. H. Colloidal Quantum Dot Solar Cells. *Chem. Rev.* **2015**, *115*, 12732-12763.

(6) Sogabe, T.; Shen, Q.; Yamaguchi, K. Recent Progress on Quantum Dot Solar Cells: A Review. *J. of Photonics for Energy* **2016**, *6*, 040901.

(7) Voznyy, O. V.; Sutherland, B. R.; Ip, A. H.; Zhitomirsky, D.; Sargent, E. H. Engineering Charge Transport by Heterostructuring Solution-processed Semiconductors. *Nat. Rev. Mater.* **2017**, *2*, 17026.

(8) Luo, B.; Bonabi Naghadeh, S.; Zhang, J. Z. Lead Halide Perovskite Nanocrystals: Stability, Surface Passivation, and Structural Control. *ChemNanoMat* **2017**, *3*, 456-465.

(9) Bonabi Naghadeh, S.; Luo, B.; Abdelmageed, G.; Pu, Y.-C.; Zhang, C.; Zhang, J. Z. Photophysical Properties and Improved Stability of Organic–Inorganic Perovskite by Surface Passivation. *J. Chem. C* **2018**, *122*, 15799-15818.

(10) Brus, L. E. Electron–electron and Electron-hole Interactions in Small Semiconductor Crystallites: The Size Dependence of the Lowest Excited Electronic State. *J. Chem. Phys.* **1984**, *80*, 4403-4409.

(11) Ekimov, A. I.; Efros, A. L.; Onushchenko, A. A. Quantum Size Effect in Semiconductor Microcrystals. *Solid State Commun.* **1985**, *56*, 921-924.

(12) Weller, H. Quantized Semiconductor Particles: A Novel State of Matter for Materials Science. *Adv. Mater.* **1993**, *5*, 88–95.

(13) Aristidou, N.; Sanchez-Molina, I.; Chotchuangchutchaval, T.; Brown, M.; Martinez, L.; Rath, T.; Haque, S. A. The Role of Oxygen in the Degradation of Methylammonium Lead Trihalide Perovskite Photoactive Layers. *Angew. Chem. Int. Ed.* **2015**, *54*, 8208-8212.

(14) Mosconi, E.; Azpiroz, J. M.; De Angelis, F. *Ab Initio* Molecular Dynamics Simulations of Methylammonium Lead Iodide Perovskite Degradation by Water. *Chem. Mater.* **2015**, *27*, 4885-4892.

(15) Christians, J. A.; Miranda Herrera, P. A.; Kamat, P. V. Transformation of the Excited State and Photovoltaic Efficiency of $CH_3NH_3PbI_3$ Perovskite upon Controlled Exposure to Humidified Air. *J. Am. Chem. Soc.* **2015**, *137*, 1530-1538.

(16) Yang, J.; Siempelkamp, B. D.; Mosconi, E.; De Angelis, F.; Kelly, T. L. Origin of the Thermal Instability in $CH_3NH_3PbI_3$ Thin Films Deposited on ZnO. *Chem. Mater.* **2015**, *27*, 4229−4236.

(17) Niu, G.; Guo, X.; Wang, L. Review of Recent Progress in Chemical Stability of Perovskite Solar Cells. *J. Mater. Chem. A* **2015**, *3*, 8970−8980.

(18) Zhao, J.; Cai, B.; Luo, Z.; Dong, Y.; Zhang, Y.; Xu, H.; Hong, B.; Yang, Y.; Li, L.; Zhang, W.; et al. Investigation of the Hydrolysis of Perovskite Organometallic Halide $CH_3NH_3PbI_3$ in Humidity Environment. *Sci. Rep.* **2016**, *6*, 21976.

(19) Abdelmageed, G.; Jewell, L.; Hellier, K.; Seymour, L.; Luo, B.; Bridges, F.; Zhang, J. Z.; Carter, S. Mechanisms for Light Induced Degradation in $MAPbI_3$ Perovskite Thin Films and Solar Cells. *Appl. Phys. Lett.* **2016**, *109*, 233905.

(20) Luo, B.; Pu, Y. C.; Lindley, S. A.; Yang, Y.; Lu, L.; Li, Y.; Li, X.; Zhang, J. Z. Organolead Halide Perovskite Nanocrystals: Branched Capping Ligands Control Crystal Size and Stability. *Angew. Chem., Int. Ed.* **2016**, *55*, 8864−8868.

(21) Marinova, N.; Franckevičius, M.; Matulaitienė, I.; Devižis, A.; Niaura, G.; Gulbinas, V.; Delgado, J. L. Hindered Amine Light Stabilizers Increase the Stability of Methylammonium Lead Iodide Perovskite against Light and Oxygen. *ChemSusChem* **2017**, *10*, 3760− 3764.

(22) Abdelmageed, G.; Mackeen, C.; Hellier, K.; Jewell, L.; Seymour, L.; Tingwald, M.; Bridges, F.; Zhang, J. Z.; Carter, S. Effect of Temperature on Light Induced

Degradation in Methylammonium Lead Iodide Perovskite Thin Films and Solar Cells. *Sol. Energy Mater. Sol. Cells* **2018**, *174*, 566−571.

(23) Hines, D. A.; Kamat, P. V. Recent Advances in Quantum Dot Surface Chemistry. *ACS Appl. Mater. Interfaces* **2014**, *6*, 3041-3057.

(24) Pan, J.; Sarmah, S. P.; Murali, B.; Dursun, I.; Peng, W.; Parida, M. R.; Liu, J.; Sinatra, L.; Alyami, N.; Zhao, C.; et al. Air-Stable Surface-Passivated Perovskite Quantum Dots for Ultra-Robust, Single- and Two-Photon-Induced Amplified Spontaneous Emission. *J. Phys. Chem. Lett.* **2015,** *6*, 5027-5033.

(25) Huang, S.; Li, Z.; Kong, L.; Zhu, N.; Shan, A.; Li, L. Enhancing the Stability of $CH_3NH_3PbBr_3$ Quantum Dots by Embedding in Silica Spheres Derived from Tetramethyl Orthosilicate in "Waterless" Toluene. *J. Am. Chem. Soc.* **2016**, *138*, 5749-5752.

(26) Veldhuis, S. A.; Tay, Y. K. E.; Bruno, A.; Dintakurti, S. S. H.; Bhaumik, S.; Muduli, S. K.; Li, M.; Mathews, N.; Sum, T. C.; Mhaisalkar, S. G. Benzyl Alcohol-Treated $CH_3NH_3PbBr_3$ Nanocrystals Exhibiting High Luminescence, Stability, and Ultralow Amplified Spontaneous Emission Thresholds. *Nano Lett.* **2017**, *17*, 7424-7432.

(27) Abdelmageed, G.; Sully, H. R.; Bonabi Naghadeh, S.; Ali, A. E.-H.; Carter, S. A.; Zhang, J. Z. Improved Stability of Organometal Halide Perovskite Films and Solar Cells toward Humidity via Surface Passivation with Oleic Acid. *ACS Appl. Energy Mater.* **2018**, *1*, 387-392.

(28) Tan, Y.; Zou, Y.; Wu, L.; Huang, Q.; Yang, D.; Chen, M.; Ban, M.; Wu, C.; Wu, T.; Bai, S.; et al. Highly Luminescent and Stable Perovskite Nanocrystals with

Octylphosphonic Acid as a Ligand for Efficient Light-Emitting Diodes. *ACS Appl. Mater. Interfaces* **2018**, *10*, 3784-3792.

(29) Krieg, F.; Ochsenbein, S. T.; Yakunin, S.; ten Brinck, S.; Aellen, P.; Süess, A.; Clerc, B.; Guggisberg, D.; Nazarenko, O.; Shynkarenko, Y.; et al. Colloidal $CsPbX_3$ (X = Cl, Br, I) Nanocrystals 2.0: Zwitterionic Capping Ligands for Improved Durability and Stability. *ACS Energy Lett.* **2018**, *3*, 641-646.

(30) Kovalenko, M. V.; Scheele, M.; Talapin, D. V. Colloidal Nanocrystals with Molecular Metal Chalcogenide Surface Ligands. *Science* **2009**, *324*, 1417−1420.

(31) Liu, D.; Gangishetty, M. K.; Kelly, T. L. Effect of $CH_3NH_3PbI_3$ Thickness on Device Efficiency in Planar Heterojunction Perovskite Solar Cells. *J. Mater. Chem. A* **2014**, *2*, 19873-19881.

(32) Lan, X.; Voznyy, O.; García de Arquer, F. P.; Liu, M.; Xu, J.; Proppe, A. H.; Walters, G.; Fam, F.; Tan, H.; Liu, M.; et al. 10.6% Certified Colloidal Quantum Dot Solar Cells via Solvent-Polarity-Engineered Halide Passivation. *Nano Lett.* **2016**, *16*, 4630-4634.

(33) Yang, Z.; Fan, J. Z.; Proppe, A. H.; García de Arquer, F. P.; Rossouw, D.; Voznyy, O.; Lan, X.; Liu, M.; Walters, G.; Quintero-Bermudez, R.; et al. Mixed-quantum-dot Solar Cells. *Nat. Commun.* **2017**, *8*, 1325.

(34) Karani, A.; Yang, L.; Bai, S.; Futscher, M. H.; Snaith, H. J.; Ehrler, B.; Greenham, N. C.; Di, D. Perovskite/Colloidal Quantum Dot Tandem Solar Cells: Theoretical Modeling and Monolithic Structure. *ACS Energy Lett.* **2018**, *3*, 869-874.

(35) Zhang, X.; Zhang, J.; Phuyal, D.; Du, J.; Tian, L.; Öberg, V. A.; Johansson, M. B.; Cappel, U. B.; Karis, O.; Liu, J.; et al. Inorganic $CsPbI_3$ Perovskite Coating on

PbS Quantum Dot for Highly Efficient and Stable Infrared Light Converting Solar Cells. *Adv. Energy Mater.* **2018**, *8*, 1702049.

(36) Dibbell, R. S.; Youker, D. G.; Watson, D. F. Excited-State Electron Transfer from CdS Quantum Dots to TiO_2 Nanoparticles via Molecular Linkers with Phenylene Bridges. *J. Phys. Chem C* **2009**, *113*, 18643-18651.

(37) Zillner, E.; Fengler, S.; Niyamakom, P.; Rauscher, F.; Köhler, K.; Dittrich, T. Role of Ligand Exchange at CdSe Quantum Dot Layers for Charge Separation. *J. Phys. Chem. C* **2012**, *116*, 16747-16754.

(38) Dugay, J.; Tan, P.; Ibrahim, M.; Garcia, J. C.; Lacroix, L.-M.; Fazzini P.-F.; Viau, G.; Respaud, M. Charge Transport and Interdot Coupling Tuned by the Tunnel Barrier Length in Assemblies of Nanoparticles Surrounded by Organic Ligands. *Phys. Rev. B* **2014**, *89*, 041406.

(39) Chistyakov, A. A.; Zvaigzne, M. A.; Nikitenko, V. R.; Tameev, A. R.; Martynov, I. L.; Prezhdo, O. V. Optoelectronic Properties of Semiconductor Quantum Dot Solids for Photovoltaic Applications. *Phys. Chem. Lett.* **2017**, *8*, 4129-4139.

(40) Hoffman, J. B.; Alam, R.; Kamat, P. V. Why Surface Chemistry Matters for QD−QD Resonance Energy Transfer. *ACS Energy Lett.* **2017**, *2*, 391-396.

(41) Jeong, K. S.; Tang, J.; Liu, H.; Kim, J.; Schaefer, A. W.; Kemp, K.; Levina, L.; Wang, X.; Hoogland, S.; Debnath, R.; et al. Enhanced Mobility-Lifetime Products in PbS Colloidal Quantum Dot Photovoltaics. *ACS Nano*, **2011**, *6*, 89-99.

(42) Chang, L. Y.; Lunt, R. R.; Brown, P. R.; Bulovic, V.; Bawendi, M. G. Low-Temperature Solution-Processed Solar Cells Based on PbS Colloidal Quantum Dot/CdS Heterojunctions. *Nano Lett.* **2013**, *13*, 994–999.

(43) Dai, M.-Q.; Yung, L.-Y. L. Ethylenediamine-Assisted Ligand Exchange and Phase Transfer of Oleophilic Quantum Dots: Stripping of Original Ligands and Preservation of Photoluminescence. *Chem. Mater*. **2013**, *25*, 2193–2201.

(44) Hines, D. A.; Kamat, P. V. Quantum Dot Surface Chemistry: Ligand Effects and Electron Transfer Reactions. *J. Phys. Chem. C* **2013**, *117*, 14418-14426.

(45) Crisp, R. W.; Kroupa, D. M.; Marshall, A. R.; Miller, E. M.; Zhang, J.; Beard, M. C.; Luther, J. M. Metal Halide Solid-state Surface Treatment for High Efficiency PbS and PbSe QD Solar Cells. *Sci. Rep*. **2015**, *5*, 9945.

(46) Cohen, E.; Gdor, I.; Romero, E.; Yochelis, S.; van Grondelle, R.; Paltiel, Y. Achieving Exciton Delocalization in Quantum Dot Aggregates Using Organic Linker Molecules. *J. Phys. Chem. Lett.* **2017**, *8*, 1014-1018.

(47) Wheeler, L. M.; Sanehira, E. M.; Marshall, A. R.; Schulz, P.; Suri, M.; Anderson, N. C.; Christians, J. A.; Nordlund, D.; Sokaras, D.; Kroll, T.; et al. Targeted Ligand-Exchange Chemistry on Cesium Lead Halide Perovskite Quantum Dots for High-Efficiency Photovoltaics. *J. Am. Chem. Soc.* **2018**, *140*, 10504-10513.

(48) Sharma, S. N.; Pillai, Z. S.; Kamat, P. V. Photoinduced Charge Transfer between CdSe Quantum Dots and *p*-Phenylenediamine. *J. Phys. Chem. B* **2003**, *107*, 10088-10093.

(49) Liu, I.-S.; Lo, H.-H.; Chien, C.-T.; Lin, Y.-Y.; Chen, C.-W.; Chen, Y.-F.; Su, W.-F.; Liou, S.-C. Enhancing Photoluminescence Quenching and Photoelectric Properties of CdSe Quantum Dots with Hole Accepting Ligands. *J. Mater. Chem.* **2008**, *18*, 675-682.

(50) Knowles, K. E.; Tice, D. B.; McArthur, E. A.; Solomon, G. C.; Weiss, E. A. Chemical Control of the Photoluminescence of CdSe Quantum Dot–Organic Complexes with a Series of Para-Substituted Aniline Ligands. *J. Am. Chem. Soc.* **2010**, *132*, 1041-1050.

(51) Donakowski, M. D.; Godbe, J. M.; Sknepnek, R.; Knowles, K. E.; Olvera de la Cruz, M.; Weiss, E. A. A Quantitative Description of the Binding Equilibria of para-Substituted Aniline Ligands and CdSe Quantum Dots. *J. Phys. Chem. C* **2010**, *114*, 22526-22534.

(52) Tan, Y.; Jin, S.; Hamers, R. J. Influence of Hole-Sequestering Ligands on the Photostability of CdSe Quantum Dots. *J. Phys. Chem. C* **2013**, *117*, 313-320.

(53) Frederick, M. T.; Amin, V. A.; Swenson, N. K.; Ho, A. Y.; Weiss, E. A. Control of Exciton Confinement in Quantum Dot–Organic Complexes through Energetic Alignment of Interfacial Orbitals. *Nano Lett.* **2013**, *13*, 287-292.

(54) Zuo, L.; Chen, Q.; De Marco, N.; Hsieh, Y.-T.; Chen, H.; Sun, P.; Chang, S.-Y.; Zhao, H.; Dong, S.; Yang, Y. Tailoring the Interfacial Chemical Interaction for High-Efficiency Perovskite Solar Cells. *Nano Lett.* **2017**, *17*, 269-275.

(55) Pu, Y.-C.; Ma, H.; Sajben, N.; Xia, G.; Zhang, J.; Li, Y.; Zhang, J. Z. Dependence of Interfacial Charge Transfer on Bifunctional Aromatic Molecular Linkers in CdSe Quantum Dot Sensitized TiO_2 Photoelectrodes. *ACS Appl. Energy Mater.* **2018**, *1*, 2907-2917.

(56) Dai, J.; Xi, J.; Li, L.; Zhao, J.; Shi, Y.; Zhang, W.; Ran, C.; Jiao, B.; Hou, X.; Duan, X.; et al. Charge Transport between Coupling Colloidal Perovskite Quantum

Dots Assisted by Functional Conjugated Ligands. *Angew. Chem., Int. Ed.* **2018**, *57*, 5754-5758.

(57) Wang, F.; Geng, W.; Zhou, Y.; Fang, H.-H.; Tong, C.-J.; Loi, M. A.; Liu, L.-M. Phenylalkylamine Passivation of Organolead Halide Perovskites Enabling High-Efficiency and Air-Stable Photovoltaic Cells. *Adv. Mater.* **2016**, *28*, 9986-9992.

(58) Zhou, Y.; Wang, F.; Cao, Y.; Wang, J.-P.; Fang, H.-H.; Loi, M. A.; Zhao, N.; Wong, C.-P. Benzylamine-Treated Wide-Bandgap Perovskite with High Thermal-Photostability and Photovoltaic Performance. *Adv. Energy Mater.* **2017**, *7*, 1701048.

(59) Luo, B.; Bonabi Naghadeh, S.; Allen, A.; Li, X.; Zhang, J. Z. Peptide-Passivated Lead Halide Perovskite Nanocrystals Based on Synergistic Effect between Amino and Carboxylic Functional Groups. *Adv. Funct. Mater.* **2017**, *27*, 1604018.

(60) Zhang, F.; Zhong, H.; Chen, C.; Wu, X.; Hu, X.; Huang, X.; Han, X.; Zou, B.; Dong, Y. Brightly Luminescent and Color-Tunable Colloidal $CH_3NH_3PbX_3$ (X = Br, I, Cl) Quantum Dots: Potential Alternatives for Display Technology. *ACS Nano* **2015**, *9*, 4533-4542.

(61) Schmidt, L. C.; Pertegas, A.; Gonzalez-Carrero, S.; Malinkiewicz, O.; Agouram, S.; Minguez Espallargas, G.; Bolink, H. J.; Galian, R. E.; Perez-Prieto, J. Nontemplate Synthesis of $CH_3NH_3PbBr_3$ Perovskite Nanoparticles. *J. Am. Chem. Soc.* **2014**, *136*, 850-853.

(62) Yeo, J. S.; Kang, R.; Lee, S.; Jeon, Y. J.; Myoung, N.; Lee, C. L.; Kim, D. Y.; Yun, J. M.; Seo, Y. H.; Kim, S. S.; et al. Highly Efficient and Stable Planar

Perovskite Solar Cells with Reduced Graphene Oxide Nanosheets as Electrode Interlayer. *Nano Energy* **2015**, *12*, 96-104.

(63) Liang, P. W.; Liao, C. Y.; Chueh, C. C.; Zuo, F.; Williams, S. T.; Xin, X. K.; Lin, J.; Jen, A. K. Additive Enhanced Crystallization of Solution – Processed Perovskite for Highly Efficient Planar – Heterojunction Solar Cells. *Adv. Mater.* **2014**, *26*, 3748-3754.

(64) Li, H.; Tao, L.; Huang, F.; Sun, Q.; Zhao, X.; Han, J.; Shen, Y.; Wang, M. Enhancing Efficiency of Perovskite Solar Cells via Surface Passivation with Graphene Oxide Interlayer. *ACS Appl. Mater. Interfaces* **2017**, *9*, 38967-38976.

(65) Ning, Z.; Tian, H.; Qin, H.; Zhang, Q.; Ågren, H.; Sun, L.; Fu, Y. Wave-Function Engineering of CdSe/CdS Core/Shell Quantum Dots for Enhanced Electron Transfer to a TiO_2 Substrate. *J. Phys. Chem. C* **2010**, *114*, 15184-15189.

(66) Kongkanand, A.; Tvrdy, K.; Takechi, K.; Kuno, M.; Kamat, P. V. Quantum Dot Solar Cells. Tuning Photoresponse through Size and Shape Control of CdSe-TiO_2 Architecture. *J. Am. Soc.* **2008**, *130*, 4007-4015.

(67) Jamshidi, A.; Yuan, C.; Chmyrov, V.; Widengren, J.; Sun, L.; Ågren, H. Efficiency Enhanced Collodial Mn-Doped Type II Core/Shell ZnSe/CdS Quantum Dot Sensitized Hybrid Solar Cells. *Journal of Nanomaterials* **2015**, *2015*,921903.

(68) Saif, A. A.; Poopalan, P. Effect of the Film Thickness on the Impedance Behavior of Sol-Gel $Ba_{0.6}Sr_{0.4}TiO_3$ Thin Films. *Physica B* **2011**, *406*, 1283-1288.

(69) Samu, G. F.; Scheidt, R. A.; Kamat, P. V.; Janáky, C. Electrochemistry and Spectroelectrochemistry of Lead Halide Perovskite Films: Materials Science Aspects and Boundary Conditions. *Chem. Mater.* **2018**, *30*, 561-569.

(70) Kim, Y. C.; Kim, K. H.; Son, D.-Y.; Jeong, D.-N.; Seo, J.-Y.; Choi, Y. S.; Han, I. T.; Lee, S. Y.; Park, N. G. Printable Organometallic Perovskite Enables Large-area, Low-dose X-ray Imaging. *Nature* **2017**, *550*, 87-91.

(71) Zhumekenov, A. A.; Saidaminov, M. I.; Haque, M. A.; Alarousu, E.; Sarmah, S. P.; Murali, B.; Dursun, I. D.; Miao, X.-H.; Abdelhady, A. L.; Wu, T. et al. Formamidinium Lead Halide Perovskite Crystals with Unprecedented Long Carrier Dynamics and Diffusion Length. *ACS Energy Lett.* **2016**, *1*, 32-37.

(72) Hodes, G.; Kamat, P. V. Understanding the Implication of Carrier Diffusion Length in Photovoltaic Cells. *J. Phys. Chem. Lett.* **2015**, *6*, 4090-4092.

(73) Helander, M. G.; Greiner, M. T.; Wang, Z. B.; Tang, W. M. Work Function of Fluorine Doped Tin Oxide. *J. Vac. Sci. Technol. A* **2011**, *29*, 011019.

(74) Miller, O. D.; Yablonovitch, E.; Kurtz, S. R. Strong Internal and External Luminescence as Solar Cells Approach the Shockley–Queisser Limit. *IEEE J. Photovoltaics* **2012,** *2*, 303-311.

(75) Saidaminov, M. I.; Almutlaq, J.; Sarmah, S.; Dursun, I.; Zhumekenov, A. A.; Begum, R.; Pan, J.; Cho, N.; Mohammed, O. F.; Bakr, O. M. Pure Cs_4PbBr_6: Highly Luminescent Zero-Dimensional Perovskite Solids. *ACS Energy Lett.* **2016**, *1*, 840-845.

(76) Sutter-Fella, C. M.; Li, Y.; Amani, M.; Ager, J. W.; Toma, F. M.; Yablonovitch, E.; Sharp, I. D.; Javey, A. High Photoluminescence Quantum Yield in Band Gap Tunable Bromide Containing Mixed Halide Perovskites. *Nano Lett.* **2016**, *16*, 800-806.

(77) Braly, I. L.; deQuilettes, D. W.; Pazos-Outón, L. M.; Burke, S.; Ziffer, M. E.; Ginger, D. S.; Hillhouse, H. W. Hybrid Perovskite Films Approaching the Radiative Limit with over 90% Photoluminescence Quantum Efficiency. *Nat. Photon.* **2018**, *12*, 355-361.

Chapter 5. Enhancing Charge Carrier Delocalization in Perovskite Quantum Dot Solids with Energetically Aligned Conjugated Capping Ligands

5.1. Abstract

Compared to bulk perovskites, charge transport in perovskite quantum dot (PQD) solids is limited. To address this issue, energetically aligned capping ligands were used to prepare methylammonium lead bromide ($MAPbBr_3$) PQDs towards enhancing surface charge carrier density in PQD solids. Trans-cinnamic acid (TCA) and its derivates, functionalized with electron-donating or electron-withdrawing groups to modulate energy levels, are used as passivating exciton-delocalizing ligands (EDLs) to decrease the energy gap with respect to the PQD core. 3,3-diphenylpropylamine (DPPA) ligand is shown to stabilize EDLs on the PQD surface through π-π stacking intermolecular interaction, mitigating charge trapping and non-radiative decay. Passivation using EDLs in combination with DPPA increases the photoluminescence (PL) quantum yield (QY) (90%), photoconductivity, extraction, mobility, transport time, and lifetime of charge carriers in PQD solids. Prototype PQD-based light-emitting diodes (LEDs) were demonstrated with a low turn-on voltage of 2.5 V.

5.2. Introduction

Semiconductor QDs based on organo-metal halide perovskites (OMHP) with the formula ABX_3 (A = methylammonium (MA^+), B = Pb^{2+}, X = Cl^-, Br^-, I^-) show great

promise for optoelectronic applications because of their size-tunable bandgap, facile solution-based synthesis and potential low-cost fabrication.[1-9] Compared to other semiconductors, OMHPs show a high tolerance for defects and long exciton lifetimes, which enable fabrication of highly efficient devices.[10-17]

For device applications such as photovoltaic (PV) or light-emitting diode (LED), electronic inter-PQD coupling is critical for effective charge transport through PQD solid film. However, this has been a major limiting factor since most ligands used to stabilize PQDs are insulating.[18] Such ligands present a large potential barrier for charge transfer between PQDs in solid film.[19-23] For example, $CsPbI_3$ PQDs synthesized with insulating oleylamine and oleic acid capping ligands were fabricated into solar cells with optimal PQD film thickness near 200 nm.[24] Films with greater thickness resulted in a decrease of performance mainly due to lack of photocurrent and charge transport. The state-of-the-art perovskite solar cells based on bulk film have optimal film thicknesses between 400-800 nm.[25-28] Therefore, PQD films need to be thick enough for sufficient light absorption and, at the same time, maintain effective charge transport.

To improve charge transport, one approach is to incorporate conjugated capping ligands to enable delocalization of charge carriers from the QD to its ligands. This allows greater access of charge carriers at interfacial regions. In a previous report, using hole accepting aromatic ligands for CdSe QDs resulted in a 10-fold improvement in short circuit current density (I_{sc}) compared to passivating with long-chain hydrocarbon ligands.[29] This method was extended to the hole-delocalizing ligand phenyldithiocarbamate (PTC) for CdSe QDs.[30-33] Conjugating PTC to CdSe QDs

causes a bathochromic shift in the absorption spectrum, which signifies an extension in charge carrier delocalization volume and follows the quantum confinement effect. This QD-ligand coupling is attributed to energetic alignment between the highest occupied molecular orbitals (HOMO) of PTC and the highest density-of-states in the valence band-edge of CdSe QDs. In other studies, the effect of PbS QD surface modification on exciton delocalization was investigated using trans-cinnamic acid (TCA) derivatives as capping ligands.[34-36] Functionalizing the TCA molecule with electron withdrawing or electron donating groups profoundly affects the band-edge positions, bandgap, and optical absorption enhancement of PbS QDs. Furthermore, energetic alignment between the orbitals of exciton-delocalizing ligands (EDLs) and the band-edges of QDs can affect charge carrier cooling, which is sensitive to the ligand binding configuration.[37] Therefore, in addition to energetic alignment, specific EDL binding on the QD surface can significantly affect QD-QD electronic coupling and thereby charge transport in QD solids.

Using EDLs to increase QD-QD electronic coupling has also been reported for $MAPbBr_3$ PQDs. An LED device fabricated using $MAPbBr_3$ PQDs passivated with EDLs resulted in 22-fold higher conductivity and carrier mobility than $MAPbBr_3$ PQDs with long alkyl-chain capping ligands.[22] Additionally, in our previous work, $MAPbBr_3$ PQDs passivated with EDLs were observed to have higher conductivity and charge mobility along with longer excitonic recombination lifetime and faster charge transport time.[23] However, to achieve greater QD-QD electronic coupling for PQD solids, it is critical to energetically align the related molecular orbitals of the ligands with the band-edges of the PQD core.

In this work, $MAPbBr_3$ PQDs were synthesized by surface passivating with valeric acid (VA), TCA, trans-4-(trifluoromethyl) cinnamic acid (TFCA), trans-2,3,4,5,6-pentafluorocinnamic acid (PFCA), and trans-4-methoxycinnamic acid (MOCA) to vary their energy levels with respect to the band-edges of the PQD core as well as butylamine (BTYA) and 3,3-diphenylpropylamine (DPPA) to stabilize the conjugated carboxylate ions and/or alter their binding geometry on the PQD surface. Optical and photoelectrochemical as well as time-resolved optical and electrical measurements have confirmed that conjugated ligands with HOMO and/or lowest unoccupied molecular orbital (LUMO) closest to the band-edges of the $MAPbBr_3$ PQDs increases charge delocalization on the PQD surface when passivated in combination with DPPA. DPPA's π-π stacking intermolecular interaction in conjunction with TCA, TFCA, or MOCA, generates PQD solid films with enhanced optical and electronic properties as well as produces bright electroluminescent LED devices with low turn-on voltages.

5.3. Experimental Section

5.3.1. Materials

All chemicals were used without further purification, which include: toluene (spectroscopic grade, Fisher Scientific), N,N-Dimethylformamide (DMF) (spectroscopic grade, Fisher Scientific), $PbBr_2$ (99.99%, Alfa Aesar), MABr (Greatcellsolar), butylamine (BTYA) (99%, Oakwood Chemical), 3,3-diphenylpropylamine (DPPA) (98%, Combi-block), valeric acid (VA) (99%, Alfa

Aesar), trans-cinnamic acid (TCA) (99%, Alfa Aesar), trans-4-(trifluoromethyl) cinnamic acid (TFCA) (99%, Oakwood Chemical), trans-2,3,4,5,6-pentafluorocinnamic acid (PFCA) (99%, Oakwood Chemical), trans-4-methoxycinnamic acid (MOCA) (99%, TCI), and oleic acid (OA) (97%, Alfa Aesar).

5.3.2. Spectroscopy and Microscopy

Absorption spectra were measured with an Agilent Technologies Cary 60 UV-Vis spectrophotometer. Fluorescence spectra were measured using a HORIBA Jobin Yvon Fluoromax-3 spectrofluorometer. Transmission electron microscopy images were obtained using a FEI monochromated F20 UT Tecnai. Scanning electron microscopy image was obtained using a FEI Quanta 3D Dual beam microscope.

5.3.3. Absolute PLQY

Newport 819C-SF-4 Integrating Sphere with an optical setup consists of two mirrors, the integrating sphere, a focusing lens and collimating lens, an optical fiber, a 450 nm short pass filter, a 470 nm long pass filter, a PicoQuant PDM series single photon avalanche diode (SPAD) for detection and a Coherent 405 nm continuous wave diode laser for excitation. Silicon wafers (with and without samples on them) were glued to clean glass slides, which are then placed into the holder at one end of the integrating sphere. The laser light is incident on the sample and reflects inside the integrating sphere, transmitting through the optical fiber where it is collimated and refocused onto a SPAD. The filters are switched out to measure the laser counts being absorbed/emitted from the sample. Next, the calibration slide (silicon wafer + blank

glass slide) is placed into the holder and the laser is turned on to measure the amount of counts reflected off the calibration slide. Then, we measure the counts absorbed by the sample by replacing the calibration slide with a sample slide, along with the short pass filter. Once these counts are recorded, the emission is measured by switching out the short pass filter with the high pass filter. **Figure 5.3.1** is a diagram of the measurement.

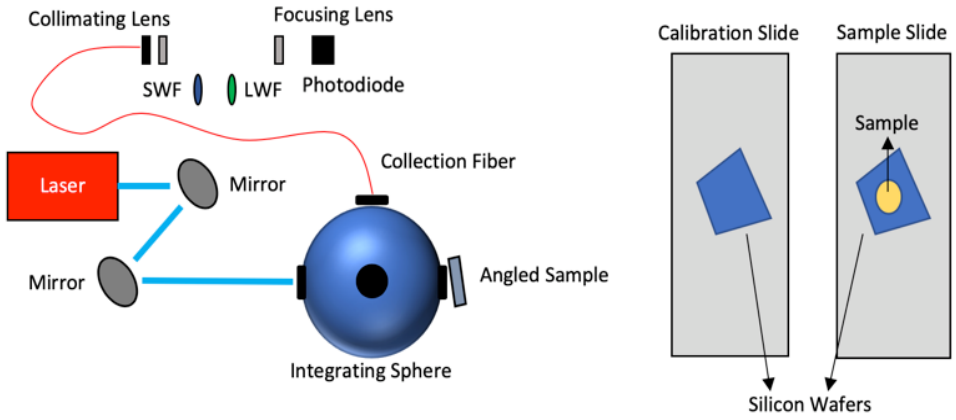

Figure 5.3.1. *Diagram of integrated sphere for measuring absolute PLQY.*

5.3.4. BTYA-VA,-TCA,-TFCA,-PFCA, and -MOCA $MAPbBr_3$ Synthesis

$MAPbBr_3$ PQDs were synthesized using a solvent reprecipitation method under ambient conditions. CH_3NH_3Br (80 mol, 9.0 mg), $PbBr_2$ (0.20 mmol, 73 mg), and VA (0.16 mmol, 16 µL), TCA (0.16 mmol, 24 mg), TFCA (0.16 mmol, 35 mg), PFCA (0.16 mmol, 38 mg), or MOCA (0.16 mmol, 29 mg) and 400 µL DMF was added to a borosilicate 7.0 mL vial and the solution was sonicated and heated until all solid dissolved. Next, BTYA (81 µmol, 8.0 µL) was added to the solution and sonicated for 30 sec. 100 µL of the precursor solution was injected at a fast rate to 5.0 mL toluene

stirring at 1,600 rpm in a 7.0 mL borosilicate vial. The bright yellow PQD solution was purified first by centrifugation at 5,500 rpm for 5 min. (3 times), collecting the solid and discarding supernatant. Then, the solid was re-dispersed in 7.0 mL toluene and filtered using a loosely packed cotton-plug. Finally, the PQD solution was centrifugated again at 5,500 rpm and liquid was discarded. Films (borosilicate glass) were prepared using 100 μL of a 40 mg/mL PQD in toluene solution and spin coating at 1,000 rpm for 60 sec.

5.3.5. DPPA-VA,-TCA,-TFCA,-PFCA, and -MOCA $MAPbBr_3$ Synthesis

$MAPbBr_3$ PQDs were synthesized using a solvent reprecipitation method under ambient conditions. CH_3NH_3Br (80 μmol, 9.0 mg), $PbBr_2$ (0.20 mmol, 73 mg), and VA (0.40 mmol, 40 μL), TCA (0.40 mmol, 59 mg), TFCA (0.34 mmol, 73 mg), PFCA (0.29 mmol, 68 mg), or MOCA (0.34 mmol, 60 mg) and 400 μL DMF was added to a borosilicate 7.0 mL vial and the solution was sonicated and heated until all solid dissolved. Next, DPPA (0.17 mmol, 35 μL) was added to the solution and sonicated for 30 sec. 100 μL of the precursor solution was injected at a fast rate to 5.0 mL toluene stirring at 1,600 rpm in a 7.0 mL borosilicate vial. The bright yellow PQD solution was purified first by centrifugation at 5,500 rpm for 5 min. (three times), collecting the solid and discarding supernatant. Then, the solid was re-dispersed in 7.0 mL toluene and filtered using a loosely packed cotton-plug. Finally, the PQD solution was centrifugated again at 5,500 rpm and liquid was discarded. Films (borosilicate glass) were prepared using 100 μL of a 40 mg/mL PQD in toluene solution and spin coating at 1,000 rpm for 60 sec.

5.3.6. BTYA-OA and DPPA-OA MSC Synthesis

$MAPbBr_3$ MSCs were synthesized using a solvent reprecipitation method under ambient conditions. CH_3NH_3Br (80 μmol, 9.0 mg), $PbBr_2$ (0.20 mmol, 73 mg), and 400 μL DMF was added to a borosilicate 7.0 mL vial and the solution was sonicated and heated until all solid dissolved. Next, DPPA (1.5 mmol, 300 μL) or BTYA (2.0 mmol, 200 μL) was added to the solution and sonicated for 30 sec. Then, OA (1.0 mmol, 250 μL) was added to the solution and sonicated for 30 sec. 100 μL of the precursor solution was injected at a fast rate to 5.0 mL toluene stirring at 1,600 rpm in a 7.0 mL borosilicate vial. The clear MSC solution was then diluted in toluene, 1.0 mL toluene was added to 2.0 mL MSC solution. The MSC (2:1) solution produces bright blue photoluminescence under a UV lamp.

5.3.7. Fourier Transform-Infrared Spectroscopy

FT-IR spectra were obtained using a PerkinElmer Spectrum One FT-IR Spectrometer. FT-IR spectra of each $MAPbBr_3$ PQD with identifying TCA, TFCA, PFCA, or MOCA peaks are displayed in **Figure 5.3.2.** In the range 900 to 600 cm^{-1} several monosubstituted aromatic C-H is observed for each $MAPbBr_3$ PQD. In the range 1700 to 1525 cm^{-1} a new C=O stretching is observed for each $MAPbBr_3$ QD except for DPPA-TFCA and DPPA-PFCA, however, from 1500 to 900 cm^{-1} C-F stretching is observed in the FT-IR spectra of these $MAPbBr_3$ PQDs.

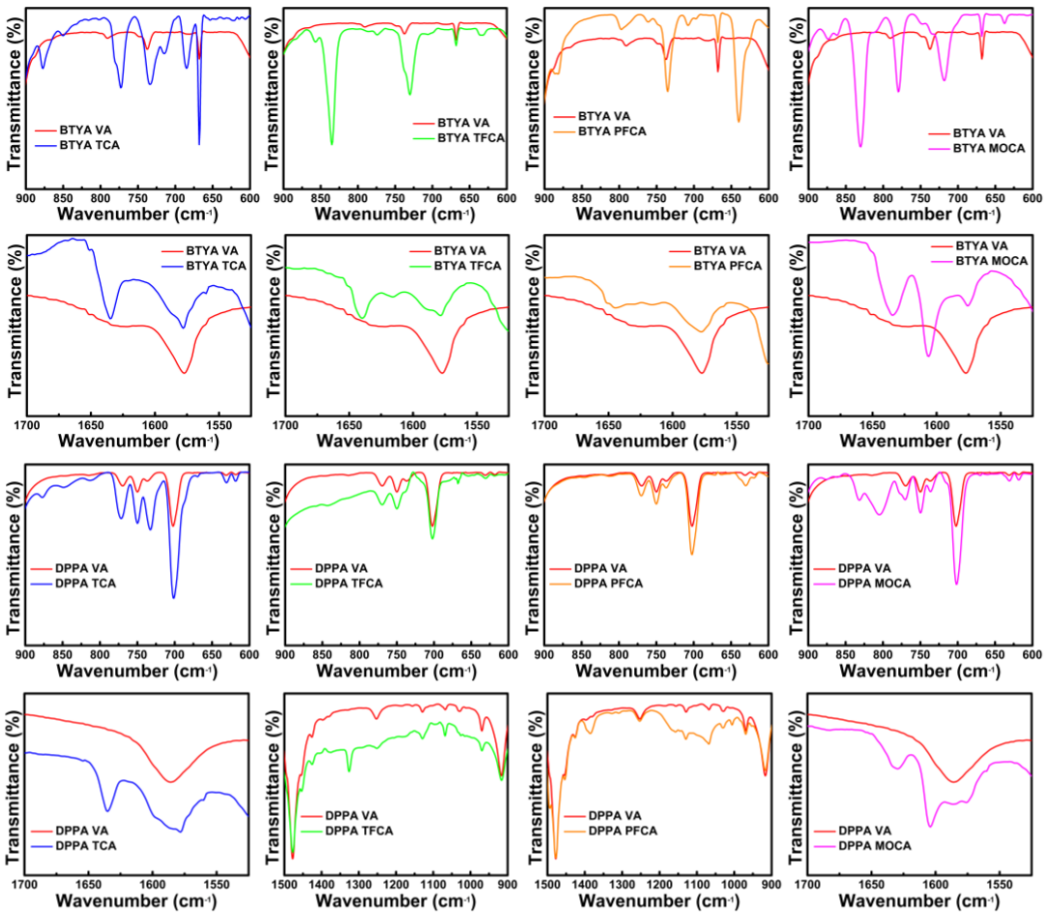

Figure 5.3.2. *FT-IR spectra of each $MAPbBr_3$ PQD in ranges with characteristic TCA, TFCA, PFCA, or MOCA peaks.*

5.3.8. Ligand Exchange of BTYA-OA and DPPA-OA MSCs with TCA

5.0 mL of the MSC (2:1) solution (BTYA-OA or DPPA-OA) was added to a 7.0 mL borosilicate vial containing a magnetic stir bar and TCA (2.0 mmol, 296 mg). The ligand exchange solution was set to stir (1,000 rpm) in the refrigerator (5 ºC) for 24 hours. As a control, 5.0 mL of MSC (2:1) solution (BTYA-OA or DPPA-OA)

without TCA was set to stir (1,000 rpm) in the refrigerator (5 ºC) for 24 hours. The sizes of the MSCs were estimated using the Brus equation:[1]

$$E_{g(MSC)} = E_{g(bulk)} + \frac{h^2\pi^2}{8r^2}\left(\frac{1}{m_e} + \frac{1}{m_h}\right) - \frac{1.8e^2}{4\pi\varepsilon\varepsilon_0 r}$$

where $E_{g(MSC)}$ is the bandgap of the MSC [BTYA-OA, before ligand exchange ($E_{g(MSC)} = 2.92\ eV$) and after ligand exchange ($E_{g(MSC)} = 2.89\ eV$) ; DPPA-OA, before ligand exchange ($E_{g(MSC)} = 3.00\ eV$) and after ligand exchange ($E_{g(MSC)} = 2.81\ eV$)], $E_{g(bulk)}$ is the bandgap of the bulk material (2.30 eV),[2] h is Planck's constant, r is the radius, m_e is the effective mass of the electron, m_h is the effective mass of the hole, e is electronic charge, ε is the relative permittivity, and ε_0 is permittivity of vacuum. Using this relation and the size (r) and the $MAPbBr_3$ PQD bandgap ($E_{g(PQD)}$) from a previous report ($r = 1.55\ nm, E_{g(PQD)} = 2.64\ eV$),[3] the effective mass of the electron and hole can be calculated ($\left(\frac{1}{m_e} + \frac{1}{m_h}\right) = 2.37 \times 10^{30}\ kg^{-1}$), which is then used to calculated the size of BTYA-OA and DPPA-OA MSCs before and after ligand exchange.

5.3.9. Time-Correlated Single Photon Counting Spectroscopy

Time-resolved PL (TRPL) were taken at room temperature using a 200 MHz Ti:Sapphire laser (790-820 nm) with an output of 350 mW, which passed through a Conoptics pulse picker that was set to select 500 kHz pulse train and a BiBO crystal to generate a second harmonic pulse. The second harmonic pulse was centered at 405 nm (4.0 μJ) was used to excite the sample. The sample's emission was collected 90° using

an ID100 avalanche photodiode. The instrument response function was determined to be 50 ps. The time-resolved PL (TRPL) lifetimes were fitted using the following double-exponential function:

$$L = A_1 e^{(-\frac{t}{\tau_1})} + A_2 e^{(-\frac{t}{\tau_2})}$$

where A_1 and A_2 are the amplitude of the fast and slow decay components, and τ_1 and τ_2 are the lifetime of the fast and slow decay components, respectively. The slow decay component is mostly contributed to PL emission from the exciton as it is mostly associated with the longer timescale. Additionally, since non-radiative transitions occur on a much faster timescale than radiative transitions, a shorter fast component with higher amplitude may indicate that vibrational relaxation is the dominate mechanism. The average lifetime ($\langle\tau\rangle$) of photogenerated charge carriers was calculated using the following equation:

$$\langle\tau\rangle = \frac{A_1{\tau_1}^2 + A_2{\tau_2}^2}{A_1\tau_1 + A_2\tau_2}$$

The radiative decay rate (τ_r) was calculated using the equation:

$$\tau_r = \frac{\langle\tau\rangle}{PLQY}$$

and the non-radiative decay rate (τ_{nr}) was calculated using the equation:

$$\tau_{nr} = \frac{\langle\tau\rangle}{1 - \frac{\langle\tau\rangle}{\tau_r}}$$

Shown in **Table 5.3-1** is a summary of the calculated non-radiative and radiative lifetimes of each $MAPbBr_3$ PQD.

Table 5.3-1 *Non-radiative and radiative lifetimes of each $MAPbBr_3$ PQD calculated using absolute PLQY.*

$MAPbBr_3$ PQD	**τ_r(ns)**	**τ_{nr}(ns)**
BTYA-VA	124.7	27.8
BTYA-TCA	16.5	17.8
BTYA-TFCA	66.8	27.9
BTYA-PFCA	154	29.7
BTYA-MOCA	91.5	16.5
DPPA-VA	116	65.8
DPPA-TCA	29.1	248
DPPA-TFCA	74.9	64.6
DPPA-PFCA	62.1	53.3
DPPA-MOCA	38.8	53.0

5.3.10. Calculation of Relevant Energy Levels for the Ligands

The bandgap and band edge positions of the PQD core are assumed to be similar to that of bulk film and are obtained from a previous report (E_{HOMO} = -3.3 eV, E_{LUMO} = -5.6 eV).[2] The HOMO and LUMO energy levels for TCA (E_{HOMO} = -3.2 eV, E_{LUMO} = -6.3 eV), TFCA (E_{HOMO} = -3.8 eV, E_{LUMO} = -6.9 eV), PFCA (E_{HOMO} = -4.3 eV, E_{LUMO} = -7.5 eV), and MOCA (E_{HOMO} = -3.1 eV, E_{LUMO} = -6.1 eV) were calculated using Materials Studio DMol[3] version 2017 with Density Functional Theory Electronic Structure Program (B3LYP density functional method).[4] These calculated energy levels are compared to values from previous reports: TCA (E_{HOMO} = -3.0 eV, E_{LUMO} = -6.1 eV), TFCA (E_{HOMO} = -3.4 eV, E_{LUMO} = -6.5 eV), PFCA (E_{HOMO} = -3.0 eV, E_{LUMO} = -7.6 eV), and MOCA (E_{HOMO} = -3.1 eV, E_{LUMO} = -6.1 eV).[5,6] **Figure 5.3.3** summarizes energy levels of PQD core compared to TCA, TFCA, PFCA, and MOCA ligands.

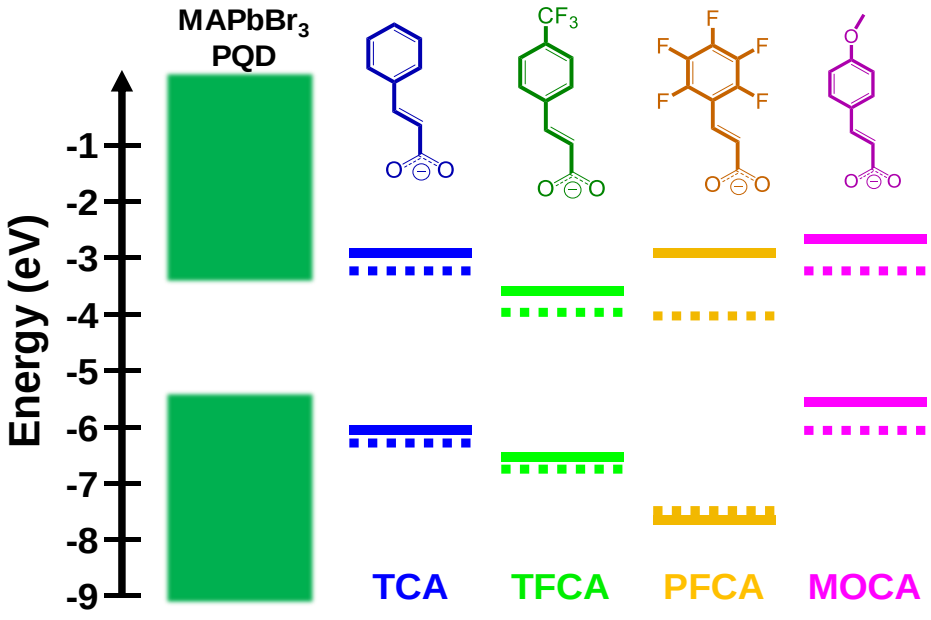

Figure 5.3.3. *Diagram of energy levels between PQD core and ligands TCA, TFCA, PFCA, and MOCA. Solid lines are values from references 5 and 6, and dashed lines are calculated results from this work.*

5.3.11. Electrochemical Impedance Spectroscopy

FTO substrates were first sonicated with liquinox solution for 10 minutes and rinsed with DI water, followed by sonication with DI water for 10 minutes and washed with isopropanol, followed by sonication with isopropanol for 10 minutes and washed with ethanol, and finally sonicated with ethanol for 10 minutes and dried with N_2. Next, the PQDs were spin-coated using 100 µL of 40 mg/mL PQD solution at 1,000 rpm for 60 sec. Films were annealed on a hot plate for 2 minutes at 70 °C. EIS was conducted similar to a previous report.[7] The spectroelectrochemical setup consists of a three-electrode cell (counter, reference, and working) in 0.10 M Bu_4NPF_6/dichloromethane

solution connected to a potentiostat/galvanostat (SI 1280B). The counter electrode was Pt wire and Ag/AgCl wire as pseudoreference electrode. The measurements were conducted in the frequency range of 1.0 MHz to 0.10 Hz at open circuit voltage. A xenon lamp irradiated film (1.0 cm^2) at 1 sun illumination (100 mW/cm^2). The lifetime of the charge transfer (τ_{rel}) was calculated using the following equation:[8]

$$\tau_{rel} = R_{CT} \times CPE$$

where *Rct* is the charge transport resistance obtained from the second x-intercept in the Nyquist plot (Figure 4), and *CPE* is the chemical-phase element obtained from the circuit fitting results.

5.3.12. Photoelectrochemical Measurements

Transient photocurrent density measurements were conducted under the same conditions as the EIS measurements. At open circuit voltage, xenon lamp (one sun illumination, 100 mW/cm^2) irradiated PQD film (1.0 cm^2) in on/off cycles every 25 sec. for 375 sec. and photocurrent density was measured as a function of time (I-t curve). **Figure 5.3.4** shows the transient photocurrent response (I-t curve) for each $MAPbBr_3$ PQD film.

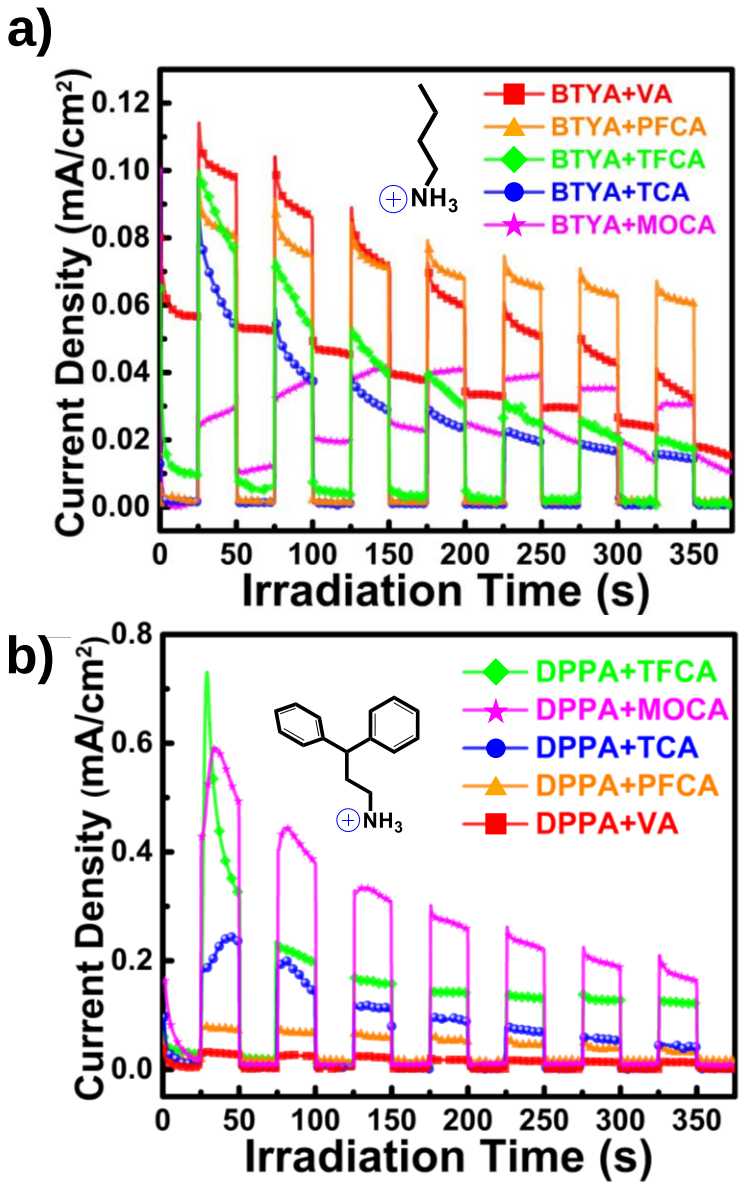

Figure 5.3.4. *Transient photocurrent response of (a) BTYA-VA,-TCA,-TFCA,-PFCA, and -MOCA and (b) DPPA-VA,-TCA,-TFCA,-PFCA, and -MOCA $MAPbBr_3$ PQD films on FTO substrate. Every 25 sec. PQD films were exposed to one sun illumination (100 mW/cm^2).*

5.3.13. Transient Photovoltage and Photocurrent Measurements

Local transient photovoltage (TPV) and transient photocurrent (TPC) decays were acquired using Agilent 5500 conductive atomic force microscopy (AFM) in contact mode. The excitation source was a green laser pulse with 532 nm wavelength generated by MGL-I-532 DPSS. In contact with the surface of film was a platinum/iridium coated silicon conductive tip (Budget Sensors ContE-G;force constant of 0.20 N/m; resonance frequency of 14 kHz). Transient data were obtained by Agilent MSOX4154A oscilloscope. Connected to the oscilloscope was an Agilent Breakout Box (N9447A) for receiving signal from the AFM controller. The oscilloscope input impedance was set to 1.0 MΩ for TPV and 50 Ω for TPC. The charge carrier lifetime and transport time of the

film was calculated using a mono-exponential decay equation:

$$X(t) = X_0 e^{\frac{-t}{\tau}}$$

where X_0 is the photocurrent or photovoltage before excitation, $X(t)$ is the photocurrent or photovoltage after excitation at time t, and τ is the charge carrier lifetime or transport time.

5.3.14. PQD-based LED Fabrication

Prepatterned ITO slides were cleaned by sonication in alconox solution (10% conc.), deionized water, 2-propanol, and ethanol, respectively, for 15 min. at 60ºC and dried using compressed nitrogen gas. A TiO_2 blocking layer (30 nm) (Solaronix Ti-nanoxide BL/SP) was prepared using a draw down method and scotch tape. This layer was heated at 125ºC on a hotplate for 5 min., then at 500ºC in an oven for 30 min. The

PQD layer (250 nm) was prepared by 50 μL of a 40 mg/mL PQD solution in toluene spin coated at 1,500 rpm 3 times. Next, 30 μL Spiro-OMeTAD (150 nm) was spun at 3000 rpm for 30 sec. and placed in a dry box for 12 hours. The gold electrode (100 nm) was thermally evaporated. The current density-voltage (*J-V*) curve of DPPA-TCA and DPPA-VA PQD-based LEDs constructed in the configuration ITO/TiO_2/PQD/Spiro-MeOTAD/Au is shown in **Figure 5.3.5.** A representative EL spectrum of DPPA-TCA $MAPbBr_3$ PQD-based LED is shown in **Figure 5.3.6**.

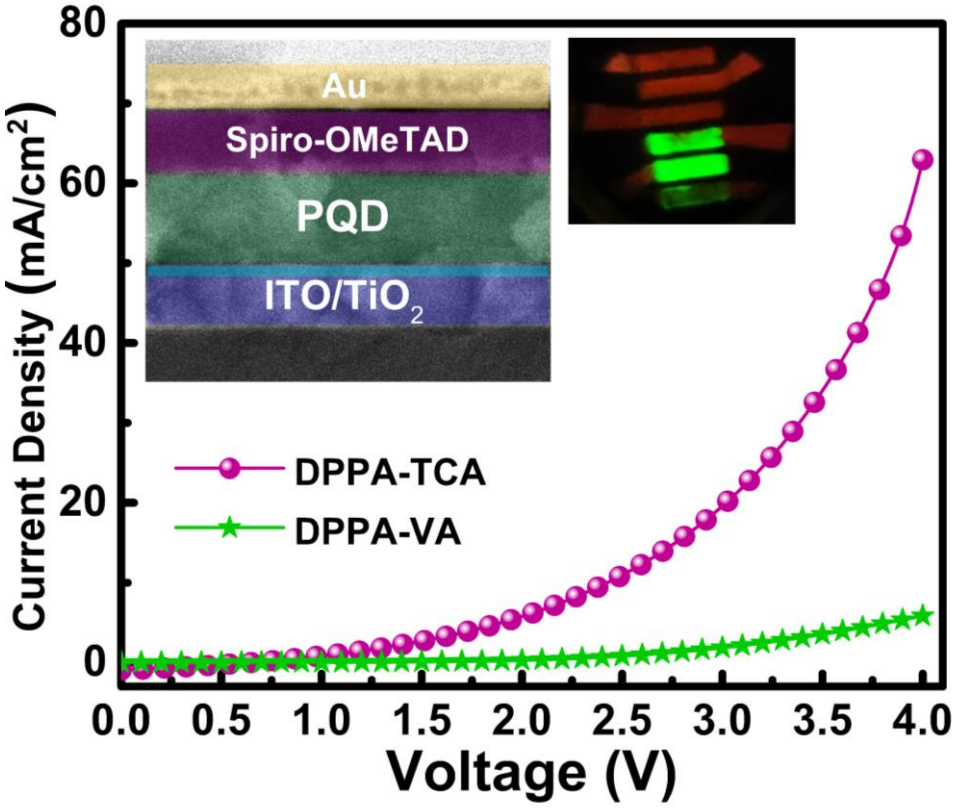

Figure 5.3.5. *Current density-voltage (J-V) curve of DPPA-TCA and DPPA-VA $MAPbBr_3$ PQD-based LEDs. Inset is SEM cross-sectional image and digital photograph of device.*

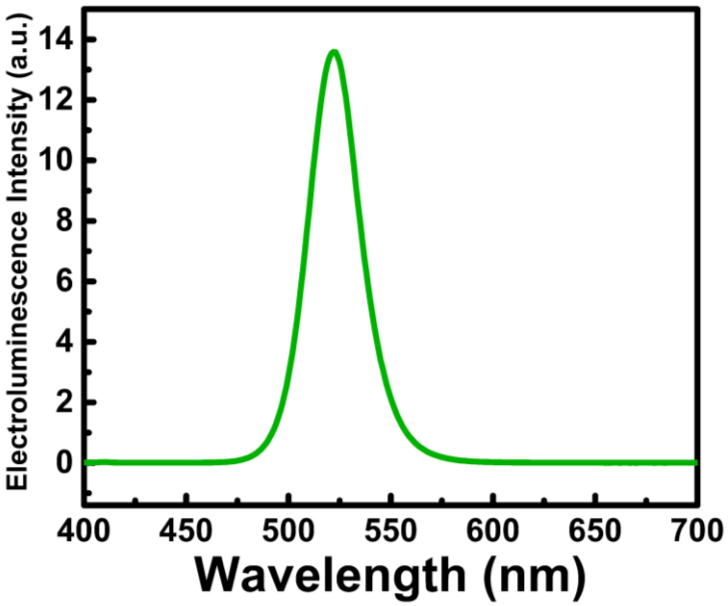

Figure 5.3.6. *Electroluminescence spectra of DPPA-TCA* $MAPbBr_3$ *PQD-based LED.*

5.3.15. References

(1) Brus, L. E. Electron–electron and Electron-hole Interactions in Small Semiconductor Crystallites: The Size Dependence of the Lowest Excited Electronic State. *J. Chem. Phys.* **1984**, *80*, 4403-4409.

(2) Leyden, M. R.; Meng, L.; Jiang, Y.; Ono, L. K.; Qiu, L.; Juarez-Perez, E. J.; Qin, C.; Adachi, C.; Qi, Y. Methylammonium Lead Bromide Perovskite Light-Emitting Diodes by Chemical Vapor Deposition. *J. Phys. Chem. Lett.* **2017**, *8*, 3193-3198.

(3) Bonabi Naghadeh, S.; Luo, B.; Pu, Y.-C.; Schwartz, Z.; Hollingsworth, W. R.; Lindley, S. A.; Brewer, A. S.; Ayzner, A. L.; Zhang, J. Z. Size Dependence of Charge Carrier Dynamics in Organometal Halide Perovskite Nanocrystals:

Deciphering Radiative Versus Nonradiative Components. *J. Phys. Chem. C* **2019**, *123*, 4610-4619.

(4) Delley, B. From Molecules to Solids with the DMol^3 Approach. *J. Chem. Phys.* **2000**, *113*, 7756.

(5) Kroupa, D. M.; Vörös, M.; Brawand, N. P.; Bronstein, N.; McNichols, B. W.; Castaneda, C. V.; Nozik, A. J.; Sellinger, A.; Galli, G.; Beard, M. C. Optical Absorbance Enhancement in PbS QD/Cinnamate Ligand Complexes. *J. Phys. Chem. Lett.* **2018**, *9*, 3425-3433.

(6) Sert, Y.; Doğan, H.; Navarrete, A.; Somanathan, R.; Aguirre, G.; Çırak, Ç. Experimental FT-IR, Laser-Raman and DFT Spectroscopic Analysis of 2,3,4,5,6-Pentafluoro-trans-cinnamic Acid. *Spectrochim. Acta A* **2014**, *128*, 119-126.

(7) Samu, G. F.; Scheidt, R. A.; Kamat, P. V.; Janáky, C. Electrochemistry and Spectroelectrochemistry of Lead Halide Perovskite Films: Materials Science Aspects and Boundary Conditions. *Chem. Mater.* **2018**, *30*, 561-569.

(8) Kim, Y. C.; Kim, K. H.; Son, D.-Y.; Jeong, D.-N.; Seo, J.-Y.; Choi, Y. S.; Han, I. T.; Lee, S. Y.; Park, N. G. Printable Organometallic Perovskite Enables Large-area, Low-dose X-ray Imaging. *Nature* **2017**, *550*, 87-91.

5.4. Results and Discussion

$MAPbBr_3$ PQDs were synthesized by following a previously reported procedure.[23] Precursor solution consisting of $PbBr_2$, MABr, DPPA or BTYA, and VA, TCA, TFCA, PFCA, or MOCA is dissolved in N,N-dimethylformamide (DMF) and rapidly injected into a vigorously stirred toluene antisolvent. A detailed description of

the synthesis is in the experimental section. Absolute PLQY data were obtained using an integrating sphere, a diagram of the measurement is displayed in **Figure 5.3.1**. Absolute PLQY for each $MAPbBr_3$ PQD sample is shown in **Table 5.4-1**. DPPA-TCA $MAPbBr_3$ PQDs are observed to have the highest absolute PLQY at 90%. Among the PQDs synthesized with BTYA, BTYA-MOCA $MAPbBr_3$ PQDs were observed to have the highest PLQY at 72%. The UV-vis absorption and photoluminescence (PL) spectra of each $MAPbBr_3$ PQD sample is displayed in **Figure 5.4.1A,B**. Each $MAPbBr_3$ PQD sample was tuned to have an exciton absorption peak between 510 and 525 nm, and PL peak between 515 and 530 nm in order to accurately compare optical and electronic properties among different PQD samples.

Table 5.4-1 *Absolute PLQY of $MAPbBr_3$ QDs and molecular structure of a) TCA, b) TFCA, c) PFCA, d) MOCA, e) VA, f) BTYA, and g) DPPA.*

$MAPbBr_3$ PQD	**PLQY(%)**
BTYA-VA	18
BTYA-TCA	52
BTYA-TFCA	30
BTYA-PFCA	18
BTYA-MOCA	72
DPPA-VA	36
DPPA-TCA	90
DPPA-TFCA	46
DPPA-PFCA	46
DPPA-MOCA	58

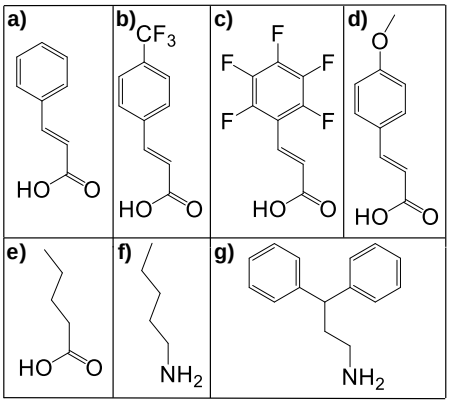

To determine the size and shape, high-resolution transmission electron microscopy (HRTEM) was performed, as shown in **Figure 5.4.1C,D**. The average diameter for the PQDs synthesized with BTYA and VA, TCA, TFCA, PFCA, or MOCA is 6.1 ± 1.5 nm, while PQDs synthesized with DPPA and each respective acid is slightly larger at 6.8 ± 1.3 nm. Shown in the inset of **Figure 5.4.1C,D** are images of lattice spacing, which is measured to be 0.29 nm for each $MAPbBr_3$ PQD sample, corresponding to the (002) crystal face of cubic $CH_3NH_3PbBr_3$.[38]

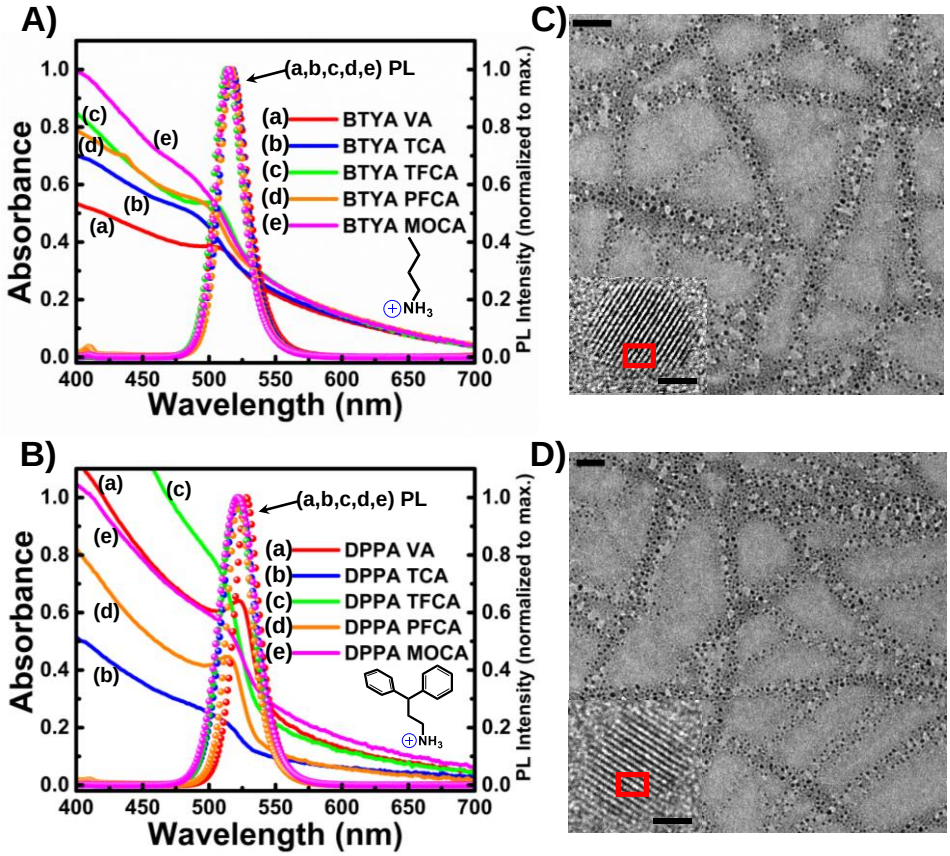

Figure 5.4.1. *UV-vis absorption (solid line) and PL spectra (dotted line) of (a) BTYA-VA (a, red), -TCA (b, blue), -TFCA (c, green), -PFCA (d, orange), and -MOCA (e, magenta) and (b) DPPA-VA (a, red), -TCA (b, blue), -TFCA (c, green), -PFCA (d, orange), and -MOCA (e, magenta) $MAPbBr_3$ PQDs suspended in toluene. (c) HRTEM image of $MAPbBr_3$ PQDs passivated with DPPA-TCA (scale bar 10 nm). The lower left inset is image of lattice spacing (scale bar 2 nm). (d) HRTEM image of BTYA-TCA $MAPbBr_3$ PQDs (scale bar 10 nm), and the lower left inset is lattice spacing image (scale bar 2 nm). HRTEM images are similar with respect to BTYA or DPPA amine with each acid.*

To confirm the presence of each capping ligand, Fourier transform-infrared (FT-IR) spectroscopy was conducted for each PQD sample, as shown in **Figure 5.3.2**. Monosubstituted aromatic C-H in the regions 770-730 and 720-680 cm^{-1} is observed for each $MAPbBr_3$ PQD, indicating the presence of TCA, TFCA, PFCA or MOCA from each respective $MAPbBr_3$ PQD.

The extent of charge carrier delocalization from passivating with conjugated capping ligands was determined from a ligand exchange using $MAPbBr_3$ magic-sized clusters (MSCs) capped with BTYA and oleic acid (OA) as well as DPPA and OA. BTYA-OA and DPPA-OA $MAPbBr_3$ MSCs were synthesized following a previously reported procedure.[39] Detail of the synthesis is in the experimental section. MSCs were chosen for ligand exchange because they are in a very strong confinement regime and more strongly confined charge carriers will have a greater sensitivity to increases to extra delocalization volume. The sizes of BTYA-OA and DPPA-OA MSCs were estimated using the Brus equation developed for QDs.[40] Due to their molecular-like structures, TEM images of the MSCs could not be obtained.[39,41] These calculated values are used as estimates and may not reflect the true size. Detail of the calculation and ligand exchange procedure is in experimental section. Before ligand exchange with TCA, the BTYA-OA and DPPA-OA MSC sizes were calculated to be 2.89 and 2.65 nm, respectively. After exchanging OA ligands with TCA ligands, a 4 nm redshift in exciton absorption peak and 4 nm red-shift in PL peak was observed for the BTYA-TCA MSC solution, equivalent of an increase in size to 2.99 nm, as shown in **Figure 5.4.2A.** The delocalization radius was estimated by subtracting the calculated MSC size before and after ligand exchange.[31] Based on the bandgap shift, this corresponds to an

increase in delocalization radius of 0.05 nm. For the DPPA-OA MSC solution, exchanging OA ligands for TCA ligands resulted in a 27 nm redshift of the absorption peak and 49 nm redshift in PL peak, as displayed in **Figure 5.4.2B.** This translates to a calculated size of 3.30 nm. Therefore, the increase in delocalization radius for DPPA-TCA MSC solution is calculated to be 0.33 nm. The larger increase in delocalization radius upon ligand exchange for the DPPA-OA MSC solution could be due to stabilization of the TCA ligands on the PQD surface from the π-π stacking interactions between the aromatic rings in the DPPA and TCA molecules. This could enable more TCA molecules to adsorb to the PQD lattice or orient TCA to have more geometric orbital overlap.

Furthermore, the PLQY before and after ligand exchange was measured. Before ligand exchange the PLQY of BTYA-OA and DPPA-OA MSC solution was calculated to be 18 ± 4% and 12 ± 3% (vs quinine sulfate, 58%), respectively. After ligand exchange, the PLQY of BTYA-TCA and DPPA-TCA MSC solution was 11 ± 3% and 36 ± 5%, respectively. This enhancement in PLQY has been previously observed in CdSe QDs upon ligand exchange with an EDL, which can be attributed to stabilization of the excitonic state and increased probability of band-edge transitions.[33]

To determine the extent of ligand interaction with the PQD core, FT-IR spectroscopy was performed before and after ligand exchange. As shown in **Figure 5.4.2C**, the most noticeable changes in the FT-IR spectra for the BTYA-OA MSCs upon ligand exchange with TCA is the appearance of strong mono-substituted aromatic C-H at 773 cm^{-1} and 688 cm^{-1}. In addition, a strong peak at 733 cm^{-1} and shoulder peak

at 716 cm^{-1} appear in the FT-IR spectrum after ligand exchange, which may also be indicative of different bound states of the TCA ligand on the PQD lattice.[42-44] For the DPPA-OA MSC ligand exchange with TCA, due to the aromatic DPPA molecule, multiple aromatic C-H is observed before ligand exchange at 770 cm^{-1}, 750 cm^{-1}, 737 cm^{-1}, and 702 cm^{-1}, as shown in **Figure 5.4.2D**. After ligand exchange, peaks in this region become stronger in intensity, sharper, and slightly shifted. Peaks after ligand exchange in the mono-substituted aromatic C-H region are at 771 cm^{-1}, 749 cm^{-1}, 733 cm^{-1}, and 700 cm^{-1} as well as the appearance of a 686 cm^{-1} shoulder peak. Shown in **Figure 5.4.2E,F** is the C=O stretching before and after ligand exchange. Before ligand exchange for BTYA-OA and DPPA-OA MSCs, there is weak and broad C=O stretching at 1630 cm^{-1} and 1626 cm^{-1}, respectively, corresponding to OA. After ligand exchange these peaks disappear and there is an appearance of a strong and sharp at peak 1635 cm^{-1} for both MSC solutions, which is assigned to the C=O stretching of TCA. Therefore, it may be concluded that TCA ligands significantly or completely replaced OA ligands.

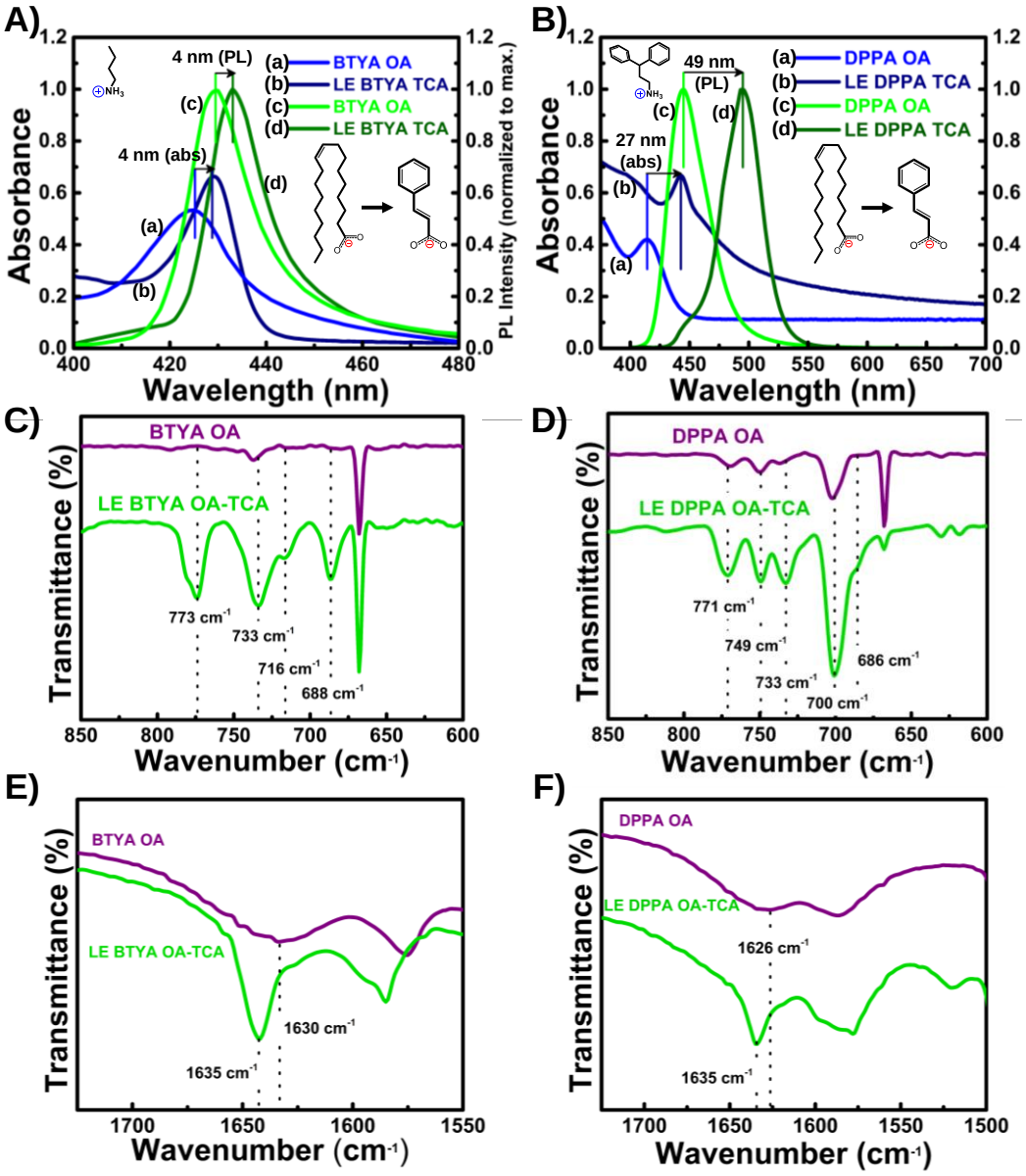

Figure 5.4.2. *UV-vis absorption spectra of (a) BTYA-OA and (b) DPPA-OA MSCs before and after ligand exchange with TCA. FT-IR spectra of (c) BTYA-OA and (d) DPPA-OA MSCs before and after ligand exchange with TCA in the C-H aromatic region, and (e) BTYA-OA and (f) DPPA-OA MSCs before and after ligand exchange with TCA in the C=O stretching region.*

The photogenerated charge carrier dynamics of each $MAPbBr_3$ PQD sample was investigated in solid films using time-correlated single-photon counting (TCSPC). Details of the measurements are described in experimental section. Comparing the valence band (VB) and conduction band (CB) edges of the PQD core with the HOMO and LUMO energy levels of each conjugated acid, based on calculations using density functional theory (DFT/B3LYP) as well as values from previous reports,[35,45,46] TCA's HOMO and LUMO orbitals are both near the VB and CB edges of the PQD core, while TFCA has LUMO more aligned to the CB edge and MOCA has its HOMO more aligned to the VB edge. The relevant energy levels are summarized in **Figure 5.3.3**. Therefore, TCA, TFCA, and MOCA are more likely to facilitate delocalization of photogenerated charge carriers in the PQD core than VA and PFCA. However, the strong interaction between the orbitals of EDLs and PQD core may facilitate trapping of charge carriers if the EDL is bound in a particular binding geometry.[37] On the surface of the PQD core, the intermolecular interaction of adjacent BTYA and EDL ligands is relatively weaker than the π-π stacking intermolecular interaction between adjacent DPPA and EDL ligands. Due to the stronger π-π stacking intermolecular interactions between adjacent DPPA and EDL ligands, vibration and rotation of the EDLs may be more restrained than with BTYA. Therefore, charge carriers delocalizing into EDLs may have less non-radiative recombination in the company of DPPA than BTYA. As shown in **Figure 5.4.3A,B**, this may contribute to the shorter or similar PL lifetimes of BTYA-TCA, BTYA-TFCA, and BTYA-MOCA $MAPbBr_3$ PQD films compared to the PL lifetimes of BTYA-VA and BTYA-PFCA $MAPbBr_3$ PQD films, which contain insulating and not energetically aligned ligands, respectively. In contrast, significantly

longer fast decay component lifetimes are observed in DPPA-TCA, DPPA-TFCA, DPPA-MOCA $MAPbBr_3$ PQD films, at 6.5 ± 0.1, 5.8 ± 0.1, and 6.3 ± 0.1 ns, respectively, compared to DPPA-VA and DPPA-PFCA $MAPbBr_3$ PQD film at 0.77 ± 0.04 and 3.05 ± 0.14 ns, respectively. This opposite trend from passivating with BTYA compared to DPPA may be due to DPPA's π-π stacking interaction, which could restrict the molecular motion of the EDLs to a greater extent than BTYA. By restricting the molecular motion of the EDLs, a dampening of non-radiative pathways slow the rate of non-radiative recombination resulting in longer PL lifetime.

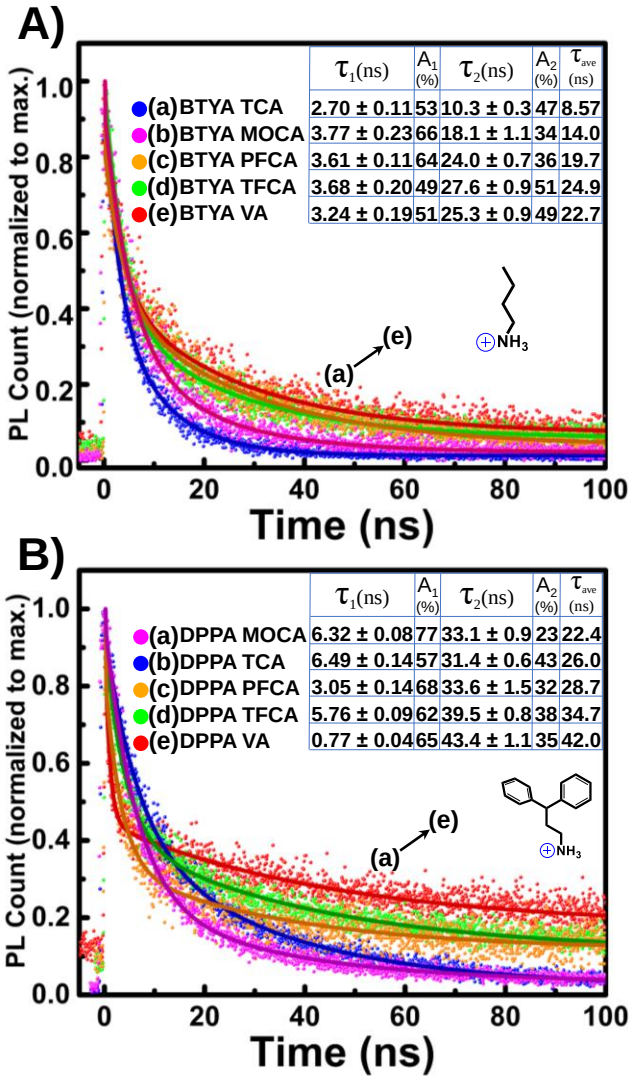

Figure 5.4.3. *Time-resolved PL spectra of (a) BTYA-VA (e, red), -TCA (a, blue), -TFCA (d, green), -PFCA (c, orange), and -MOCA (b, magenta) and (b) DPPA-VA (e, red), -TCA (b, blue), -TFCA (d, green), -PFCA (c, orange), and -MOCA (a, magenta) $MAPbBr_3$ PQD film on borosilicate glass substrate. Inset displays* $\boldsymbol{\tau_1}$, $\boldsymbol{\tau_2}$, $\boldsymbol{A_1}$, $\boldsymbol{A_2}$, *and* $\boldsymbol{\tau_{ave}}$ *representing the fast and slow decay component lifetime and amplitude, and average PL lifetime, respectively.*

Using the absolute PLQY and the average PL lifetime, the radiative and non-radiative lifetimes were calculated. Detail of the calculation is included in experimental section. As shown in **Table 5.3-1**, coupling DPPA ligand with TCA or MOCA ligands enhances its radiative rate of decay with respect to its non-radiative rate. While for BTYA ligand, when coupled with EDLs, the radiative decay is comparable or significantly slower than its non-radiative decay. The increase in radiative decay rate and PLQY in DPPA passivated PQDs could be attributed to EDL's ability to stabilize photo-excited charge carriers generated in the PQD core by forming newly available interfacial states that could enhance the probability of band-edge transitions.[33] Whereas for BTYA passivated PQDs, these interfacial states may trap charge carriers and increase non-radiative recombination.

To investigate the effect of EDLs on the conductivity and charge transport properties of PQD films, electrochemical impedance spectroscopy (EIS) was conducted. Details of the EIS measurements are supplied in experimental section. **Figure 5.4.4A,B** shows the Nyquist spectra of PQD films passivated with BTYA and DPPA with each acid, respectively. **Table 5.4-2** provides a summary of the series resistance (R_s) and charge transport resistance (R_{CT}), determined by the first and second intercepts on the real axis, respectively, as well as the lifetime of charge transfer calculated using the constant-phase element (CPE) and R_{CT}.[47] The films containing DPPA passivated PQDs have consistent R_s near 0.195 ohm, while BTYA passivated PQD films have much larger R_s ranging from 30.1 to 78.8 ohm. However, the R_{CT} and τ_{rel} for BTYA-VA and DPPA-VA $MAPbBr_3$ PQD films is similar. Therefore, DPPA ligand by itself may not have significant conductivity advantages. The conjugated acids

that are more energetically aligned with the PQD core, TCA, TFCA, and MOCA, are observed to have the highest R_{CT} and slowest τ_{rel} for BTYA passivated PQD films. This appears counterintuitive as the energetically aligned ligands should have strong PQD-ligand electronic coupling that increases surface charge carrier density. However, due to the instability and lack of π-π stacking intermolecular interaction, the strong PQD-ligand coupling may enhance trapping of charge carriers and is consistent with the TRPL measurements. As observed in TRPL measurements, BTYA and DPPA capped PQDs have the opposite trend in EIS measurements. For DPPA passivated PQDs, EDL capped PQDs have the lowest R_{CT} and fastest τ_{rel}. The fastest τ_{rel} is measured to be 0.12 ms for DPPA-TFCA $MAPbBr_3$ PQD film. Our previous work using benzylamine (BZA) and benzoic acid (BA) delocalizing ligands have a τ_{rel} of 0.63 ms,[23] which is more than five times the lifetime of DPPA-TFCA $MAPbBr_3$ PQD film. Therefore, energy level alignment as well as surface stabilization between the EDL and the PQD core is crucial for increasing surface charge carrier density and charge transport in PQD solid film.

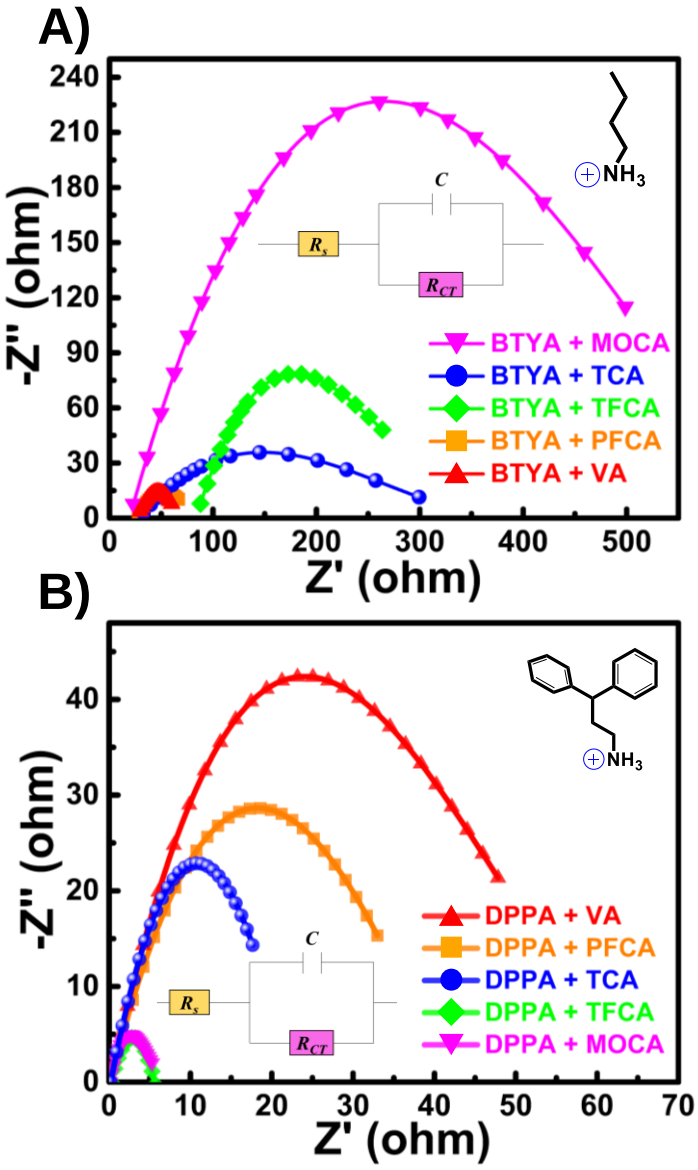

Figure 5.4.4. *Nyquist spectra of (a) BTYA-VA, -TCA,-TFCA, -PFCA, and -MOCA and (b) DPPA-VA, -TCA, -TFCA, -PFCA, and -MOCA* $MAPbBr_3$ *PQD film on FTO substrate under one sun illumination (100 mW/cm*^{2}*). Inset displays equivalent circuit.*

Table 5.4-2 *Series resistance (R_s), charge transport resistance (R_{CT}), and charge transfer lifetime (τ_{rel}) of each $MAPbBr_3$ PQD film on FTO substrate.*

$MAPbBr_3$ PQD	**R_s (ohm)**	**R_{CT} (ohm)**	**τ_{rel} (ms)**
BTYA-VA	30.1	67.5	3.20
BTYA-TCA	33.0	341	16.1
BTYA-TFCA	78.8	328	15.5
BTYA-PFCA	30.1	80.8	3.83
BTYA-MOCA	30.1	645	30.5
DPPA-VA	0.195	60.5	2.97
DPPA-TCA	0.195	21.9	1.04
DPPA-TFCA	0.195	2.67	0.12
DPPA-PFCA	0.195	40.2	1.90
DPPA-MOCA	0.195	7.18	0.34

To examine the photogenerated current density, the transient photocurrent response (I-t curve) was measured for each PQD solid film. Details of the measurements are in experimental section. As shown in **Figure 5.3.4**, the photogenerated current density measurements are consistent with the TRPL and EIS measurements. PQDs passivated with BTYA and the most energetically aligned ligands TCA, TFCA, and MOCA produce less photocurrent density than the VA ligand, while is opposite is observed for DPPA passivated PQDs. Therefore, when the average ligand binding geometry facilitates charge trapping, the EDL diminishes photocurrent density even further than using an insulating capping ligand such as VA.

To gain further insight into the effect of passivating PQDs with DPPA and EDLs, local transient photocurrent (TPC) and transient photovoltage (TPV) decay measurements were conducted using conductive atomic force microscopy (AFM).

Details of the TPC and TPV measurements are supplied in experimental section. Shown in **Figure 5.4.5(A-E)** are AFM topography images of each PQD film that contain a red square representing an area 100 × 100 nm^2 where TPC and TPV measurements were performed with similar PQD film thickness on FTO substrate. Displayed in **Figure 5.4.5F** is the TPC decay curves and the inset shows the charge transport times of each PQD film. This measurement is directly related to the conductivity and charge mobility of the PQD solid films. As shown, the PQDs passivated with energetically aligned ligands are observed to have up to three-fold faster charge transport time than PQDs capped with insulating or not energetically aligned ligands. Our previous study of BZA-BA $MAPbBr_3$ PQD film was measured to have a charge transport time of 1.52 μs.[23] Thus, our new PQD films with dual passivation using energetically aligned and π-π stacking ligands, outperform PQD film with insulating or not energetically aligned ligands as well as our previously measured BZA-BA $MAPbBr_3$ PQD film.

TPV decays were collected to determine the charge carrier recombination lifetime of PQDs passivated with DPPA and each acid. Longer lifetimes represent a slower rate of exciton recombination, and hence, greater probability of charge extraction. Shown in **Figure 5.4.5G** is the TPV decay curves and in the inset is the calculated charge carrier lifetimes. Dual passivation with EDLs and DPPA increases the charge carrier lifetime by two-folds with respective to using insulating or not energetically aligned ligands. Compared to 2.92 μs for BZA-BA $MAPbBr_3$ PQD film from our previous work,[23] the energetically aligned capping ligands coupled with DPPA shows major improvement in charge carrier lifetime.

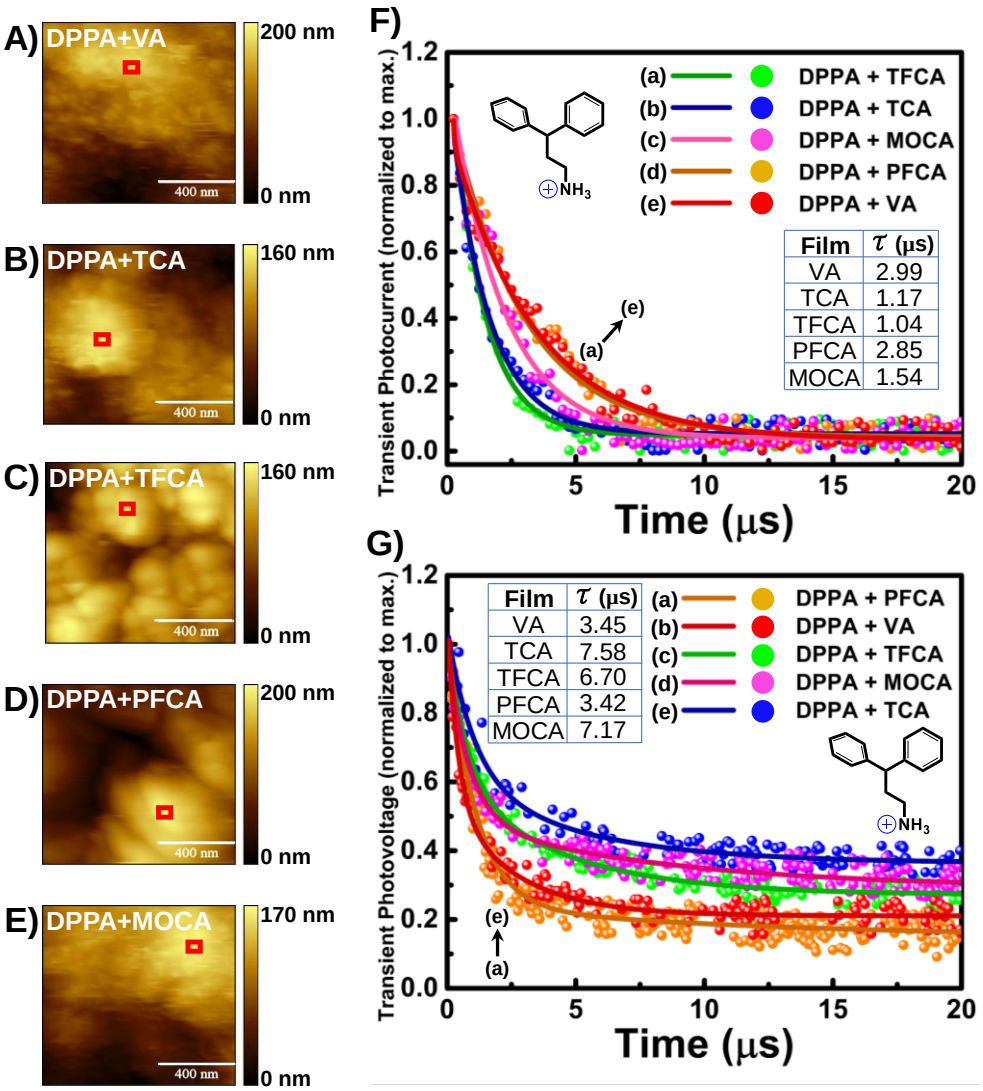

Figure 5.4.5. *AFM topography images of (a) DPPA-VA, (b) DPPA-TCA, (c) DPPA-TFCA, (d) DPPA-PFCA, and (e) DPPA-MOCA $MAPbBr_3$ PQD films on FTO substrate. The area in the red square is where films were measured for TPC and TPV. (f) TPC decay curves of DPPA-VA (e, red), -TCA (b, blue), -TFCA (a, green), -PFCA (d, orange), and -MOCA (c, magenta) $MAPbBr_3$ PQD films. (g) TPV decay curves of DPPA-VA (b, red), -TCA (e, blue), -TFCA (c, green), -PFCA (a, orange), and -MOCA (d, magenta) $MAPbBr_3$ PQD films.*

To demonstrate applications of the $MAPbBr_3$ PQDs, DPPA-TCA and DPPA-VA PQD-based LEDs were constructed and successfully demonstrated in the configuration ITO/TiO_2/PQD/Spiro-MeOTAD/Au in a preliminary study. Details of the LED fabrication are in the experimental section. As shown from the current density-voltage (*J*-*V*) curve in **Figure 5.3.5,** DPPA-TCA $MAPbBr_3$ PQD-based LEDs generate much higher current density upon increasing voltage than DPPA-VA $MAPbBr_3$ PQD-based LEDs. DPPA-VA $MAPbBr_3$ PQD-based LEDs did not light up during the measurement, however, the DPPA-TCA $MAPbBr_3$ PQD-based LED generated bright electroluminescence (EL) with a turn-on voltage of 2.5 V. A representative EL spectrum is shown in **Figure 5.3.6**. $MAPbBr_3$ PQD-based LEDs with octylamine and oleic acid capping ligands have been recently reported to have turn-on voltages between 2.9 and 4.0 V.[48-50] Therefore, DPPA-TCA $MAPbBr_3$ PQD-based LEDs show enhanced performance.

5.5. Conclusion

In summary, we report the synthesis and characterization of $MAPbBr_3$ PQDs using a combination of capping ligands that are energetically aligned and stabilized by π-π stacking. This results in higher PLQY, conductivity, and photocurrent density as well as longer PL lifetime of charge carriers compared to PQDs with insulating ligands or EDLs not stabilized on the PQD surface. In addition, DPPA passivation increases PQD's charge carrier delocalization radius by more than six-fold compared to BTYA passivation, as determined in TCA ligand exchange with OA. Furthermore, TPC and TPV measurements confirm faster charge transport times and longer charge

carrier lifetimes, respectively, for PQDs passivated with EDLs. In addition, DPPA-TCA $MAPbBr_3$ PQD-based LEDs are observed to have better performance than DPPA-VA $MAPbBr_3$ PQD-based LEDs with a low turn-on voltage of 2.5 V. This work has demonstrated that energetically aligned conjugated capping ligands coupled with a spatial orbital overlap facilitator can significantly increase surface charge carrier density for improving optical and electrical properties of PQD films for potential optoelectronic device applications.

5.6. References

(1) Sharenko, A.; Toney, M. F. Relationships between Lead Halide Perovskite Thin-Film Fabrication, Morphology, and Performance in Solar Cells. *J. Am. Chem. Soc.* **2016**, *138*, 463-470.

(2) Manser, J. S.; Christians, J. A.; Kamat, P. V. Intriguing Optoelectronic Properties of Metal Halide Perovskites. *Chem. Rev.* **2016**, *116*, 12956-13008.

(3) Snaith, H. J. Present Status and Future Prospects of Perovskite Photovoltaics. *Nat. Mater.* **2018**, *17*, 372-376.

(4) Shi, Z.; Jayatissa, A. H. Perovskite-Based Solar Cells: A Review of Recent Progress, Materials and Processing Methods. *Materials* **2018**, *11*, 729.

(5) Rashid Bin Mohd Yusoff, A.; Gao, P.; Khaja Nazeeruddin, M. Recent Progress in Organohalide Lead Perovskites for Photovoltaic and Optoelectronic Applications. *Coord. Chem. Rev.* **2018**, *373*, 258-294.

(6) Sun, J.; Wu, J.; Tong, X.; Lin, F.; Wang, Y.; Wang, Z. M. Organic/Inorganic Metal Halide Perovskite Optoelectronic Devices Beyond Solar Cells. *Adv. Sci.* **2018**, *5*, 1700780.

(7) Park, M.-H.; Kim, J. S.; Heo, J.-M.; Ahn, S.; Jeong, S.-H.; Lee, T.-W. Boosting Efficiency in Polycrystalline Metal Halide Perovskite Light-Emitting Diodes. *ACS Energy Lett.* **2019**, *4*, 1134-1149.

(8) Wei, Z.; Xing, J. The Rise of Perovskite Light-Emitting Diodes. *J. Phys. Chem. Lett.* **2019**, *10*, 3035-3042.

(9) Pham, H. D.; Xianqiang, L.; Li, W.; Manzhos, S.; Ko Ko Kyaw, A.; Sonar, P. Organic Interfacial Materials for Perovskite-Based Optoelectronic Devices. *Energy Environ. Sci.* **2019**, *12*, 1177.

(10) Zhumekenov, A. A.; Saidaminov, M. I.; Haque, M. A.; Alarousu, E.; Sarmah, S. P.; Murali, B.; Dursun, I. D.; Miao, X.-H.; Abdelhady, A. L.; Wu, T. et al. Formamidinium Lead Halide Perovskite Crystals with Unprecedented Long Carrier Dynamics and Diffusion Length. *ACS Energy Lett.* **2016**, *1*, 32-37.

(11) Xu, W.; McLeod, J. A.; Yang, Y.; Wang, Y.; Wu, Z.; Bai, S.; Yuan, Z.; Song, T.; Wang, Y.; et al. Iodomethane-Mediated Organometal Halide Perovskite with Record Photoluminescence Lifetime. *ACS Appl. Mater. Interfaces* **2016**, *8*, 23181-23189.

(12) Steirer, K. X.; Schulz, P.; Teeter, G.; Stevanovic, V.; Yang, M.; Zhu, K.; Berry, J. J. Defect Tolerance in Methylammonium Lead Triiodide Perovskite. *ACS Energy Lett.* **2016**, *1*, 360-366.

(13) Kang, J.; Wang, L.-W. High Defect Tolerance in Lead Halide Perovskite $CsPbBr_3$. *J. Phys. Chem. Lett.* **2017**, *8*, 489-493.

(14) Huang, H.; Bodnarchuk, M. I.; Kershaw, S. V.; Kovalenko, M. V.; Rogach, A. L. Lead Halide Perovskite Nanocrystals in the Research Spotlight: Stability and Defect Tolerance. *ACS Energy Lett.* **2017**, *2*, 2071-2083.

(15) Meng, G.; Shi, Y.; Wang, X.; Wang, W.; Wang, S.; Ji, M.; Hao, C. New Insight into the Ultra-Long Lifetime of Excitons in Organic-Inorganic Perovskite: Reverse Intersystem Crossing. *J. Energy Chem.* **2018**, *27*, 1496-1500.

(16) Li, M.; Begum, R.; Fu, J.; Xu, Q.; Koh, T. M.; Veldhuis, S. A.; Grätzel, M.; Mathews, N.; Mhaisalkar, S.; Sum, T. C. Low Threshold and Efficient Multiple Exciton Generation in Halide Perovskite Nanocrystals. *Nat. Comm.* **2018**, *9*, 4197.

(17) Jena, A. K.; Kulkarni, A.; Miyasaka, T. Halide Perovskite Photovoltaics: Background, Status, and Future Prospects. *Chem. Rev.* **2019**, *119*, 3036-3103.

(18) Murray, C. B.; Kagan, C. R. Charge Transport in Strongly Coupled Quantum Dot Solids. *Nat. Nanotechnol.* **2015**, *10*, 1013-1026.

(19) Hines, D. A.; Kamat, P. V. Quantum Dot Surface Chemistry: Ligand Effects and Electron Transfer Reactions. *J. Phys. Chem. C* **2013**, *117*, 14418-14426.

(20) Hines, D. A.; Kamat, P. V. Recent Advances in Quantum Dot Surface Chemistry. *ACS Appl. Mater. Interfaces* **2014**, *6*, 3041-3057.

(21) Hoffman, J. B.; Alam, R.; Kamat, P. V. Why Surface Chemistry Matters for QD−QD Resonance Energy Transfer. *ACS Energy Lett.* **2017**, *2*, 391-396.

(22) Dai, J.; Xi, J.; Li, L.; Zhao, J.; Shi, Y.; Zhang, W.; Ran, C.; Jiao, B.; Hou, X.; Duan, X.; et al. Charge Transport between Coupling Colloidal Perovskite Quantum

Dots Assisted by Functional Conjugated Ligands. *Angew. Chem., Int. Ed.* **2018**, *57*, 5754-5758.

(23) Vickers, E. T.; Graham, T. A. Chowdhury, A. H.; Bahrami, B.; Dreskin, B. W.; Lindley, S.; Bonabi Naghadeh, S.; Qiao, Q.; Zhang, J. Z. Improving Charge Carrier Delocalization in Perovskite Quantum Dots by Surface Passivation with Conductive Aromatic Ligands. *ACS Energy Lett.* **2018**, *3*, 2931-2939.

(24) Zolfaghari, Z.; Hassanabadi, E.; Pitarch-Tena, D.; Yoon, S. J.; Shariatinia, Z.; van de Lagemaat, J.; Luther, J. M.; Mora-Seró, I. Operation Mechanism of Perovskite Quantum Dot Solar Cells Probed by Impedance Spectroscopy. *ACS Energy Lett.* **2019**, *4*, 251-258.

(25) Liu, D.; Gangishetty, M. K.; Kelly, T. L. Effect of $CH_3NH_3PbI_3$ Thickness on Device Efficiency in Planar Heterojunction Perovskite Solar Cells. *J. Mater. Chem. A* **2014**, *2*, 19873-19881.

(26) Saliba, M.; Matsui, T.; Seo, J.-Y.; Domanski, K.; Correa-Baena, J. P.; Nazeeruddin, M. K.; Zakeeruddin, S. M.; Tress, W.; Abate, A.; Hagfeldt, A.; et al. Cesium-Containing Triple Cation Perovskite Solar Cells: Improved Stability, Reproducibility and High Efficiency. *Energy Environ. Sci.* **2016**, *9*, 1989-1997.

(27) Habisreutinger, S. N.; Wenger, B.; Snaith, H. J.; Nicholas, R. J. Dopant-Free Planar n-i-p Perovskite Solar Cells with Steady-State Efficiencies Exceeding 18%. *ACS Energy Lett.* **2017**, *2*, 622-628.

(28) Gao, L.; Spanopoulos, I.; Ke, W.; Huang, S.; Hadar, I.; Chen, L.; Li, X.; Yang, G.; Kanatzidis, M. G. Improved Environmental Stability and Solar Cell Efficiency of

(MA,FA)PbI_3 Perovskite Using a Wide-Band-Gap 1D Thiazolium Lead Iodide Capping Layer Strategy. *ACS Energy Lett.* **2019**, *4*, 1763-1769.

(29) Liu, I.-S.; Lo, H.-H.; Chien, C.-T.; Lin, Y.-Y.; Chen, C.-W.; Chen, Y.-F.; Su, W.-F.; Liou, S.-C. Enhancing Photoluminescence Quenching and Photoelectric Properties of CdSe Quantum Dots with Hole Accepting Ligands. *J. Mater. Chem.* **2008**, *18*, 675-682.

(30) Frederick, M. T.; Weiss, E. A. Relaxation of Exciton Confinement in CdSe Quantum Dots by Modification with a Conjugated Dithiocarbamate Ligand. *ACS Nano* **2010**, *4*, 3195-3200.

(31) Frederick, M. T.; Amin, V. A.; Swenson, N. K.; Ho, A. Y.; Weiss, E. A. Control of Exciton Confinement in Quantum Dot-Organic Complexes through Energetic Alignment on Interfacial Orbitals. *Nano Lett.* **2013**, *13*, 287-292.

(32) Frederick, M. T.; Amin, V. A.; Weiss, E. A. Optical Properties of Strongly Coupled Quantum Dot-Ligand Systems. *J. Phys. Chem. Lett.* **2013**, *4*, 634-640.

(33) Jin, S.; Harris, R. D.; Lau, B.; Aruda, K. O.; Amin, V. A.; Weiss, E. A. Enhanced Rate of Radiative Decay in CdSe Quantum Dots upon Adsorption of an Exciton-Delocalizing Ligand. *Nano Lett.* **2014**, *14*, 5323-5328.

(34) Kroupa, D. M.; Vörös, M.; Brawand, N. P.; McNichols, B. W.; Miller, E. M.; Gu, J.; Nozik, A. J.; Sellinger, A.; Galli, G.; Beard, M. C. Tuning Colloidal Quantum Dot Band Edge Positions through Solution-Phase Surface Chemistry Modification. *Nat. Commun.* **2017**, *8*, 15257.

(35) Kroupa, D. M.; Vörös, M.; Brawand, N. P.; Bronstein, N.; McNichols, B. W.; Castaneda, C. V.; Nozik, A. J.; Sellinger, A.; Galli, G.; Beard, M. C. Optical

Absorbance Enhancement in PbS QD/Cinnamate Ligand Complexes. *J. Phys. Chem. Lett.* **2018**, *9*, 3425-3433.

(36) Bronstein, N. D.; Martinez, M. S.; Kroupa, D. M.; Vörös, M.; Lu, H.; Brawand, N. P.; Nozik, A. J.; Sellinger, A.; Galli, G.; Beard, M. C. Designing Janus Ligand Shells on PbS Quantum Dots using Ligand-Ligand Cooperativity. *ACS Nano* **2019,** *13*, 3839-3846.

(37) Azzaro, M. S.; Babin, M. C.; Stauffer, S. K.; Henkelman, G.; Roberts, S. T. Can Exciton-Delocalizing Ligands Facilitate Hot Hole Transfer from Semiconductor Nanocrystals?. *J. Phys. Chem. C* **2016**, *120*, 28224-28234.

(38) Schmidt, L. C.; Pertegas, A.; Gonzalez-Carrero, S.; Malinkiewicz, O.; Agouram, S.; Minguez Espallargas, G.; Bolink, H. J.; Galian, R. E.; Perez-Prieto, J. Nontemplate Synthesis of $CH_3NH_3PbBr_3$ Perovskite Nanoparticles. *J. Am. Chem. Soc.* **2014**, *136*, 850-853.

(39) Vickers, E. T.; Xu, K.; Dreskin, B. W.; Graham, T. A.; Li, X.; Zhang, J. Z. Ligand Dependent Growth and Optical Properties of Hybrid Organo-Metal Halide Perovskite Magic Sized Clusters. *J. Phys. Chem. C* **2019**, *123*, 18746-18752.

(40) Brus, L. E. Electron–electron and Electron-hole Interactions in Small Semiconductor Crystallites: The Size Dependence of the Lowest Excited Electronic State. *J. Chem. Phys.* **1984**, *80*, 4403-4409.

(41) Peng, L.; Dutta, A.; Xie, R.; Yang, W.; Pradhan, N. Dot-Wire-Platelet-Cube: Step Growth and Structural Transformations in $CsPbBr_3$ Perovskite Nanocrystals. *ACS Energy Lett.* **2018**, *3*, 2014-2020.

(42) Cooper, J. K.; Franco, A. M.; Gul, S.; Corrado, C.; Zhang, J. Z. Characterization of Primary Amine Capped CdSe, ZnSe, and ZnS Quantum Dots by FT-IR: Determination of Surface Bonding Interaction and Identification of Selective Desorption. *Langmuir* **2011**, *27*, 8486-8493.

(43) Son, J. G.; Choi, E.; Piao, Y.; Han, S. W.; Lee, T. G. Probing Organic Ligands and their Binding Schemes on Nanocrystals by Mass Spectrometric and FT-IR Spectroscopic Imaging. *Nanoscale* **2016**, *8*, 4573-4578.

(44) Peters, J. L.; van de Bos, K. H. W.; Van Aert, S.; Goris, B.; Bals, S.; Vanmaekelbergh, D. Ligand-Induced Shape Transformation of PbSe Nanocrystals. *Chem. Mater.* **2017**, *29*, 4122-4128.

(45) Leyden, M. R.; Meng, L.; Jiang, Y.; Ono, L. K.; Qiu, L.; Juarez-Perez, E. J.; Qin, C.; Adachi, C.; Qi, Y. Methylammonium Lead Bromide Perovskite Light-Emitting Diodes by Chemical Vapor Deposition. *J. Phys. Chem. Lett.* **2017**, *8*, 3193-3198.

(46) Sert, Y.; Doğan, H.; Navarrete, A.; Somanathan, R.; Aguirre, G.; Çırak, Ç. Experimental FT-IR, Laser-Raman and DFT Spectroscopic Analysis of 2,3,4,5,6-Pentafluoro-trans-cinnamic Acid. *Spectrochim. Acta A* **2014**, *128*, 119-126.

(47) Kim, Y. C.; Kim, K. H.; Son, D.-Y.; Jeong, D.-N.; Seo, J.-Y.; Choi, Y. S.; Han, I. T.; Lee, S. Y.; Park, N. G. Printable Organometallic Perovskite Enables Large-area, Low-dose X-ray Imaging. *Nature* **2017**, *550*, 87-91.

(48) Jin, X.; Zhang, X.; Fang, H.; Deng, W.; Xu, X.; Jie, J.; Zhang, X. Facile Assembly of High-Quality Organic-Inorganic Hybrid Perovskite Quantum Dot Thin Films for Bright Light-Emitting Diodes. *Adv. Funct. Mater.* **2018**, *28*, 1705189.

(49) Yao, Y.; Yu, H.; Wu, Y.; Lu, Y.; Liu, Z.; Xu, X.; Ma, B.; Zhang, Q.; Chen, S.; Huang, W. Efficient Quantum Dot Light-Emitting Diodes Based on Trioctylphosphine Oxide-Passivated Organometallic Halide Perovskites. *ACS Omega* **2019**, *4*, 9150-9159.

(50) Huang, H.; Zhao, F.; Liu, L.; Zhang, F.; Wu, X.; Shi, L.; Zou, B.; Pei, Q.; Zhong, H. Emulsion Synthesis of Size-Tunable $CH_3NH_3PbBr_3$ Quantum Dots: An Alternative Route toward Efficient Light-Emitting Diodes. *ACS Appl. Mater. Interfaces* **2015**, *7*, 28128-28133.

Chapter 6. Ligand Dependent Growth and Optical Properties of Hybrid Organo-Metal Halide Perovskite Magic Sized Clusters

6.1. Abstract

Magic sized clusters (MSCs), small nanoparticles with a single size or narrow size distribution, possess unique chemical and physical properties. $CH3NH_3PbBr_3$ perovskite MSCs (PMSCs) were synthesized using butylamine (BTYA) and valeric acid (VA) as well as 3,3-diphenylpropylamine (DPPA) and VA as capping ligands in an excess amount. The PMSCs were characterized using UV–vis and photoluminescence (PL) spectroscopy. For BTYA-VA PMSCs, there is an excitonic absorption peak at 424 nm and PL peak at 434 nm, while the DPPA-VA PMSCs exhibit an absorption peak at 428 nm and PL peak at 451 nm. The size and optical properties of the PMSCs are found to be dependent on the ligands used for passivation. Additionally, in a series dilution of DPPA-VA PMSCs in toluene, it was discovered that different sized perovskite quantum dots (PQDs) can be synthesized with tunable PL emission with peaks ranging between 451 and 525 nm. This phenomenon was not observed for BTYA-VA PMSCs. This contrast indicates the unique interaction between the DPPA ligand and the toluene solvent for the dilution-induced PQD formation. These findings provide new insights into the mechanism of growth and stability of PMSCs that are useful for generating and understanding the formation of larger nanostructures such as QDs.

6.2. Introduction

Semiconductor magic size clusters (MSCs) are ultra-small nanoparticles that have a narrow size distribution and strong quantum confinement.[1] These discretely sized nanoclusters are usually smaller than 2 nm and have sharp absorption and photoluminescence (PL) peaks due to their molecule-like properties.[2-5] MSCs exhibit optical properties that are significantly blue shifted with respect to their bulk optical properties and reflect the structure approaching unit cell limit of the material's lattice.[6] These MSCs are the smallest building blocks for forming larger nanostructures such as nanocrystals (NCs) or quantum dots (QDs), and exhibit intriguing optical and physical properties for studying nanostructure growth and fundamental properties of well-defined nanostructures.

While the synthesis and characterization of II-VI semiconductor MSCs has been widely studied,[1,7-12] only a few studies have been reported on all inorganic metal halide perovskite MSCs (PMSCs). In one study, ultra-small $CsPbBr_3$ nanoclusters (< 2 nm) were synthesized by using a high concentration of oleylamine and oleic acid capping ligands.[13] Excessive amount of capping ligand is key towards stabilizing these $CsPbBr_3$ PMSCs that exhibit an absorption peak at 391 nm and a weak PL band peaked at 410 nm. The $CsPbBr_3$ clusters could assemble into nanoribbons after purification with width and thickness of 2.1 nm and 0.9 nm, respectively, and bright blue emission at 440 nm. In a recent study on $CsPbBr_3$ PMSCs, Peng *et al.* demonstrated size tuning in a one pot synthesis from 0.6 nm up to the quantum confinement limit (> 25 nm).[6] At the PMSC size, the absorption peak was at 402 nm and by increasing the temperature of the $CsPbBr_3$ PMSC solution, they were able to observe conversion of PMSCs to

nanowires, platelets, and then cube shaped PQDs with absorption peak at 515 nm (> 7 nm) . However, to our knowledge, there has been no study reported on organo-metal halide PMSCs and the effect of using different capping ligands.

Here, we report the synthesis of $CH_3NH_3PbBr_3$ PMSCs using butylamine (BTYA) and valeric acid (VA) as well as 3,3-diphenylpropylamine (DPPA) and VA as capping ligands. The growth and optical properties of the PMSCs are found to be strongly ligand dependent. The BTYA-VA PMSCs exhibit excitonic absorption peaked at 424 nm while DPPA-VA PMSCs at 428 nm. Additionally, DPPA-VA PMSCs show a large Stokes shift in PL with a peak at 451 nm, while the BTYA-VA PMSCs have a much smaller Stokes shift with a PL peak at 434 nm. Based on the exciton absorption peaks, the size for BTYA-VA and DPPA-VA PMSCs was estimated to be 2.58 nm and 2.72 nm, respectively. Furthermore, the stability and growth kinetics of the PMSCs were evaluated to be strongly ligand and concentration dependent.

6.3. Experimental Section

6.3.1. Materials

N,N-Dimethylformamide (DMF) 99.5% was purchased from Fisher Scientific. Toluene 100% was purchased from LabChem Inc. Chloroform 99.9% was purchase from Fisher Chemical. Lead bromide ($PbBr_2$) 98% was purchased from Alfa Aesar. Methylammonium bromide (CH_3NH_3Br) was purchased from GreatCell Solar. Butylamine (BTYA) 99% was purchased from Oakwood Chemical. 3,3-

Diphenylpropylamine (DPPA) 98% was purchased from Combi-Blocks. Valeric acid (VA) 99% was purchased from Alfa Aesar.

6.3.2. Synthesis of BTYA-VA PMSCs

$CH_3NH_3PbBr_3$ MSCs were synthesized using a solvent reprecipitation method under ambient conditions. CH_3NH_3Br (80 μmol, 9.0 mg) and $PbBr_2$ (0.20 mmol, 73 mg) were dissolved in 400 μL DMF. Then, variable amounts of VA (0.73 mmol, 80 μL mmol) was added and dissolved in precursor solution. Next, BTYA (2.02 mmol, 200 μL) was added to the precursor solution and dissolved. 100 μL of the precursor solution was injected rapidly to 5.0 mL toluene stirring at 1,300 rpm for 10 min. BTYA-VA PMSCs solutions were clear and colorless, and only observable fluorescence occurred when diluting the solution.

6.3.3. Synthesis of DPPA-VA PMSCs

$CH_3NH_3PbBr_3$ PMSCs were synthesized using a solvent reprecipitation method under ambient conditions. CH_3NH_3Br (80 μmol, 9.0 mg) and $PbBr_2$ (0.20 mmol, 73 mg) were dissolved in 400 μL DMF. Then, variable amounts of VA acid (0.73 mmol, 80 μL) was added and dissolved in precursor solution. Next, DPPA (1.45 mmol, 300 μL) was added to the precursor solution and dissolved. 100 μL of precursor solution was injected rapidly to 5.0 mL toluene stirring at 1,300 rpm for 10 min. DPPA-VA PMSCs solutions were clear and colorless, and only observable fluorescence occurred when diluting the solution.

6.3.4. Spectroscopic Measurements

Fourier-Transform infrared **(**FTIR) spectra were obtained with a Perkin Elmer FTIR spectrometer (Spectrum One, spectral resolution 4 cm^{-1}), where the samples were prepared by dropping the $CH_3NH_3PbBr_3$ solution onto a KBr pellet. UV-Vis absorption spectra were measured with an Agilent Technologies Cary 60 UV-Vis spectrophotometer. PL spectra were measured using a HORIBA Jobin Yvon Fluoromax-3 spectrofluorometer. The different concentrations of BTYA-VA and DPPA-VA PMSCs samples were prepared by adding 10, 20, 30, 40, 50, 60, 70, 80, 90, 100, 200, or 300 μL of the as synthesized DPPA-VA and BTYA-VA PMSCs solution into the 4.0 mL toluene. The photoluminescence (PL) quantum yield (QY) was measured against the standard quinine sulfate (PL QY 58%). For the DPPA-VA PMSCs, the absorbance intensity for the PL QY measurement was above 0.1 intensity because at low concentrations the DPPA-VA PMSCs converted to DPPA-VA PQDs. These intensities at 365 nm excitation wavelength were 0.15, 0.18, 0.21, 0.25, and 0.28. For the BTYA-VA PMSCs, the absorption intensities were under 0.1 at 365 nm.

6.3.5. Time-Correlated Single Photon Counting Spectroscopy

Time-resolved PL (TRPL) measurements were taken using a time-correlated single photon counting (TCSPC) system with a 200 MHz Ti:Sapphire laser (780-820 nm) with an output of 350 mW. The laser passes through a Conoptics pulse picker that was set to select 500 kHz pulse train and a BiBO crystal to generate a second harmonic pulse. The excitation pulse was centered at 405 (4.0 μJ). The sample's emission was

collected at a 90º angle using an ID100 avalanche photodiode. The instrument response function was measured to be 50 ps.

6.4. Results and Discussion

6.4.1. Synthesis and Characterization of PMSCs

$CH_3NH_3PbBr_3$ PMSCs were synthesized using a ligand-assisted reprecipitation method as described in previous reports.[14-16] To achieve BTYA-VA PMSCs, 200 µL (2.02 mmol) of BTYA was used as an excess amount as capping ligand to produce the ultra-small size of interest. Their UV-Vis absorption and PL spectra are shown in **Figure 6.4.1A**. The BTYA-VA PMSC solution shows an exciton absorption peak at 424 nm and PL peaked at 434 nm. The full-width half-maximum (FWHM) of its absorption band is 13 nm and PL band is 17 nm, indicating a narrow distribution of the PMSC sizes. The PL quantum yield (QY) of BTYA-VA PMSCs was calculated to be 19 ± 3% (R^2 = 0.99) (vs quinine sulfate, 58%).[17]

DPPA-VA PMSCs were synthesized similarly by using 300 µL (1.45 mmol) of DPPA ligand in a surplus amount. The UV-Vis absorption and PL peaks are at 428 nm and 451 nm, respectively, as shown in **Figure 6.4.1B**. The redder excitonic absorption peak, compared to that of BTYA-VA PMSCs, indicates larger size. This is consistent with the redder PL peak. However, the much larger Stokes shift (23 nm) of the PL peak relative to the excitonic absorption peak may also suggest the PL has contribution from band gap trap states. For the DPPA-VA PMSC solution, the FWHM of the absorption band is 13 nm and the PL band is 31 nm, which may be related to a broader size

distribution of PMSC sizes or trap states compared to the BTYA-VA PMSCs. The calculated PL QY of the DPPA-VA PMSC solution was determined to be 11 ± 2% (R^2 = 0.99) (vs, quinine sulfate, 58%).[17] The 19 ± 3% and 11 ± 2% PL QYs obtained from BTYA-VA and DPPA-VA PMSCs, respectively, is relatively high compared to previously reported $CsPbBr_3$ MSCs, which had PLQY values lower than 5%.[1] However, compared to PQDs, these PL QYs are relatively low with standard PQD PL QYs as low as 40% and as high as 99%.[1,18-20]

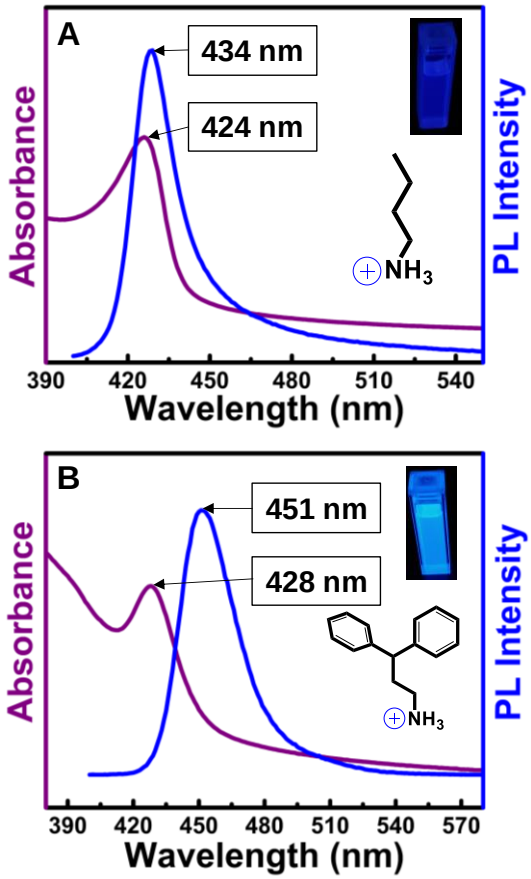

Figure 6.4.1. *UV-Vis absorption and PL spectra of (A) BTYA-VA and (B) DPPA-VA PMSCs. Insets contain amine capping ligand and digital photographs of the respective PMSC solution.*

To determine and compare the state of the surface ligands in the DPPA-VA PMSCs and DPPA-VA PQDs, FTIR spectra were measured. As shown in **Figure 6.4.2**, for the DPPA-VA PMSCs, in the region from 600 cm^{-1} to 1000 cm^{-1}, there are two sharp peaks at 690 cm^{-1} and 730 cm^{-1} corresponding to the vibration frequencies of the external plane of the C−H aromatic ring for DPPA.[21] In the 1300 cm^{-1} to 1700 cm^{-1} region, the bands at 1379 cm^{-1} and 1463 cm^{-1} can be assigned to the stretching vibration of C-H, and the bands at 1495 cm^{-1} and 1588 cm^{-1} can be assigned to the bending vibration of $-NH_2$. These signatures correspond to the DPPA molecule. Furthermore, the band at 1655 cm^{-1} can be ascribed to the stretching vibration of C=O,[16,21,22] which indicates the presence of VA molecules. In the 2800–3500 cm^{-1} region, there are four bands: two sharp bands at 2858 cm^{-1} and 2925 cm^{-1} arising from the stretching vibration of C−H, one sharp bands at 3030 cm^{-1} arising from the stretching vibration of C−C, and one broad band at 3450 cm^{-1} attributing to primary amine N−H stretch.[16,23,24] The peaks in the FTIR spectra are similar for DPPA-VA PMSCs and DPPA-VA PQDs, however, the N−H bending and the N−H stretching at 1655 cm^{-1} and 3450 cm^{-1} become more broad in the PQD FTIR spectra, indicating a change in vibrational modes that can be reflected from the changing in size or structural environment.

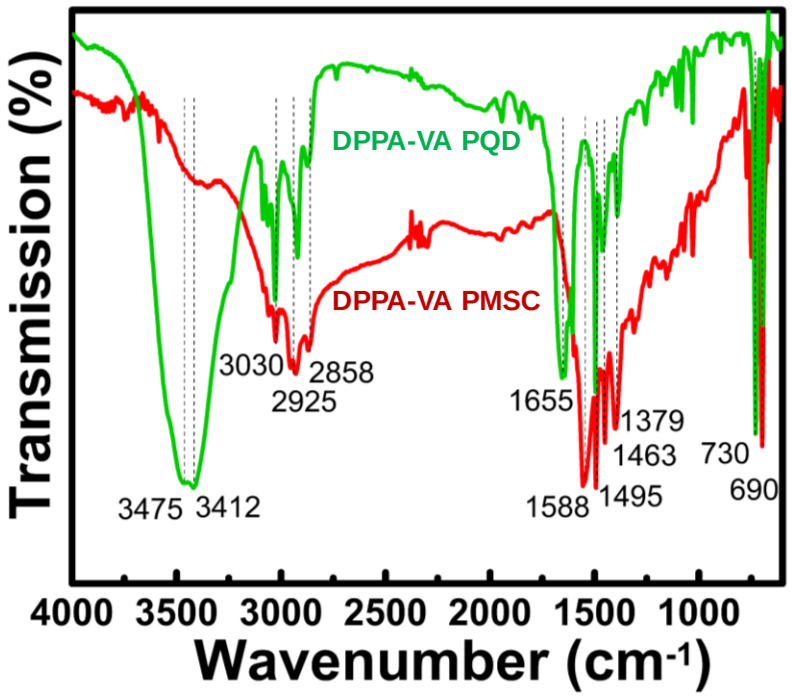

Figure 6.4.2. *FTIR spectra of DPPA-VA PMSCs and DPPA PQDs.*

The size of MSC was estimated using the Brus equation developed for QDs (assuming being applicable to MSCs):[25]

$$E_{g(PMSC)} = E_{g(bulk)} + \frac{h^2}{8r^2}\left(\frac{1}{m_e} + \frac{1}{m_h}\right)$$

where $E_{g(PMSC)}$ is the band gap of the PMSC, $E_{g(bulk)}$ is the bandgap of the bulk material, h is Planck's constant, r is the radius, m_e is the effect mass of the electron, and m_h is the effective mass of the hole. Using this relation and the size (r) and QD bandgap ($E_{g(QD)}$) from a previous report (r = 1.55 nm, $E_{g(QD)}$ = 2.64 eV, and $E_{g(bulk)}$ = 2.30 eV),[15,26] the effective reduced mass of electron and hole can be calculated ($\left(\frac{1}{m_e} + \frac{1}{m_h}\right)$ = 2.37 x 10^{30} kg^{-1}), which is then used to determine the size of the BTYA-VA and DPPA-VA PMSCs (2.58 nm and 2.72 nm) from their optical

bandgap ($E_{g(PMSC)}$ = 2.79 eV and 2.72 eV). These calculated sizes are estimates as the equation established for QDs may not hold for MSCs. However, given that it is not possible to determine the size of the MSCs using TEM due to lack of lattice structures because of their molecule-like structures, such an estimate of size serves for the purpose of comparison between different PMSCs.[1]

6.4.2. Growth and Stability of PMSCs

The growth process of the BTYA-VA and DPPA-VA PMSCs was investigated by monitoring their electronic absorption and PL spectra overtime. Optical measurements were taken at 10-minute intervals for 5 hours, and then a final measurement was taken after 24 hours. As shown in **Figure 6.4.3A**, the BTYA-VA PMSCs initially had an absorption peak at 424 nm, which red shifted to 432 nm as well as increased in absorbance intensity from 0.58 to 0.88 after the first 10 minutes. This indicates a growth process. After continuous measurements, the absorption peak continuously red shifted until stabilized at 436 nm after 50 minutes. At this point, the peak intensity dropped from 0.88 to 0.28. In addition, at 60 minutes, an additional absorption peak appeared at 405 nm. From this time to 24 hours, the 436 nm peak almost completely disappeared, while the 405 nm peak increased in intensity. Instead of continuously growing and stabilizing at a certain size with red-shifted PL as commonly observed in nanocrystal growth, the BTYA-VA PMSCs may have fragmented into smaller discrete sizes overtime. This is consistent with previous reports of MSCs.[1,27-29] This trend is confirmed in the PL spectra. Initially, there is an increase in PL intensity for the 434 nm peak, and then overtime the PL peak at 434 nm decreases

and was converted into a PL peak at 410 nm, indicating a decrease in discrete cluster size. Using Equation (1), this smaller size is calculated to be 2.12 nm.

For the DPPA-VA PMSCs, after 60 minutes the absorption peak that started at 428 nm steadily increased in intensity from 0.46 to 0.62 and red shifted to 433 nm, as shown in **Figure 6.4.3B**. At 70 minutes, the absorption peak maintained its intensity, but drastically red shifted from 433 nm to 445 nm. The absorption peak continuously red shifted and increased in intensity during the 24-hour measurement, indicating larger clusters were growing. In the meantime, the PL peak shifted from 447 nm to 471 nm and multiple PL bands appeared. Interestingly, in the absorption spectra only one sharp excitonic absorption peak is observed overtime, yet multiple bands are generated in the PL spectra. This could be due to different sized PMSCs or PQDs forming in solution or vibronic features of a specific sized PMSC, each of which could not be assigned or resolved to its corresponding excitonic peak in the absorption spectra. From the initial to the 24-hour PL measurement, the PL peak intensity increased by a factor of more than 6. This may indicate that well-passivated PMSCs or even PQDs were forming. The increase in intensity and fragmentation into different discrete sizes is consistent with previous reports.[1,27-29]

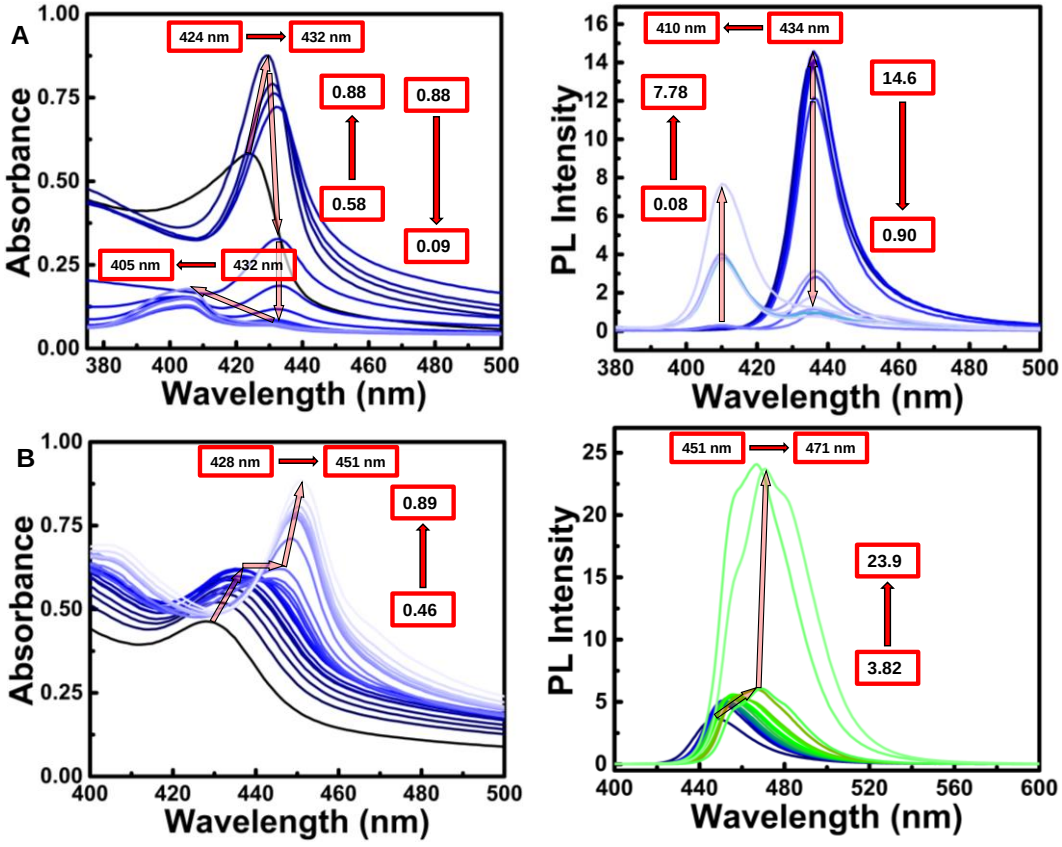

Figure 6.4.3. *UV-Vis absorption and PL spectra of (A) BTYA-VA and (B) DPPA-VA PMSCs overtime. The lightest band in each spectrum represents the measurement taken at 24 hours.*

In order to evaluate the PMSCs stability, the relative PL intensity of the BTYA-VA and DPPA-VA PMSCs solutions were measured for 1.0 h in air and dark conditions. As shown in **Figure 6.4.4**, the relative PL intensity of the DPPA-VA PMSC solution remained above 70 % after 1.0 h. However, the relative PL intensity for the BTYA-VA PMSCs decreased after 1 h to about 10%. The PMSCs degrade in air due

possibly to reaction with oxygen and water.[16,30-32] In comparison, the DPPA-VA PMSCs are more stable than the BTYA-VA PMSCs, suggesting that DPPA is a better passivating and protective ligand than BTYA.

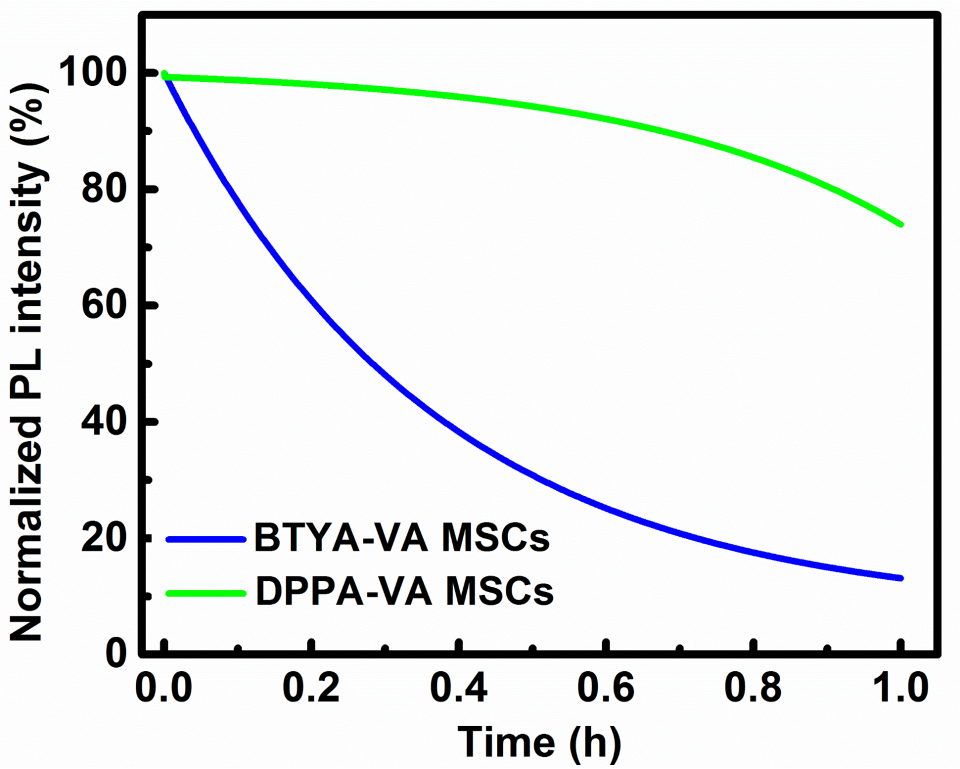

Figure 6.4.4. *Stability of DPPA-VA MSCs and BTYA-VA MSCs solution in air and in the dark: the relative fluorescence intensity as a function of exposure time.*

6.4.3. Concentration Dependence of PL Emission of PMSCs

One interesting finding is that the PL of DPPA-VA PMSCs can be tuned simply by diluting the as-synthesized solution in toluene. As shown in **Figure 6.4.5**, the PL peaks shifted from 451 nm to 525 nm with dilution. The same series dilution was

performed using a BTYA-VA PMSC solution and no change in PL resulted. Only until after 24 hours, the PL peak of the BTYA-VA PMSCs blue shifted from 438 nm to 410 nm for the two highest concentration solutions, as shown in **Figure 6.4.5A**. This observed blue shift in PL may be the result of conversion into smaller size PMSCs.

During series dilution of the DPPA-VA PMSCs in toluene, multiple PL bands were observed, as displayed in **Figure 6.4.5B**. In the initial PL measurement, the two highest concentration PMSC solutions maintained the initial PMSC PL peak at 451 nm. Successive dilution resulted in high intensity PL peaks ranging from 451 nm to 525 nm. With decreasing concentration, a red shifted shoulder peak near 505 nm continuously increased in intensity, and then, at the lowest concentrations a single PL peak at 525 nm is observed. This may indicate the formation of PQDs from collective fragments of PMSCs. Additional measurements were taken after 2 hours and resulted in an overall higher population of red shifted PL peaks between 451 and 525 nm. This trend continued after 24 hours, but with only slight increases in red shifted PL peaks populations with higher intensities. One possible explanation is that upon dilution with toluene, the ligands, due to interaction with the toluene solvent molecules, detach from the perovskite, resulting in growth into larger clusters or particles. To test this hypothesis, DPPA-VA PMSCs were diluted in chloroform, a solvent without π-π interactions. Interestingly, this trend was not observed. However, two PL peaks at 457 nm and 505 nm were observed for each dilution, as shown in **Figure 6.4.6**. These two different PL peaks are similar in peak position and relative intensity. There is a possibility that these two peaks are due to PQD formation, however, emission energy is not tunable by diluting in chloroform.

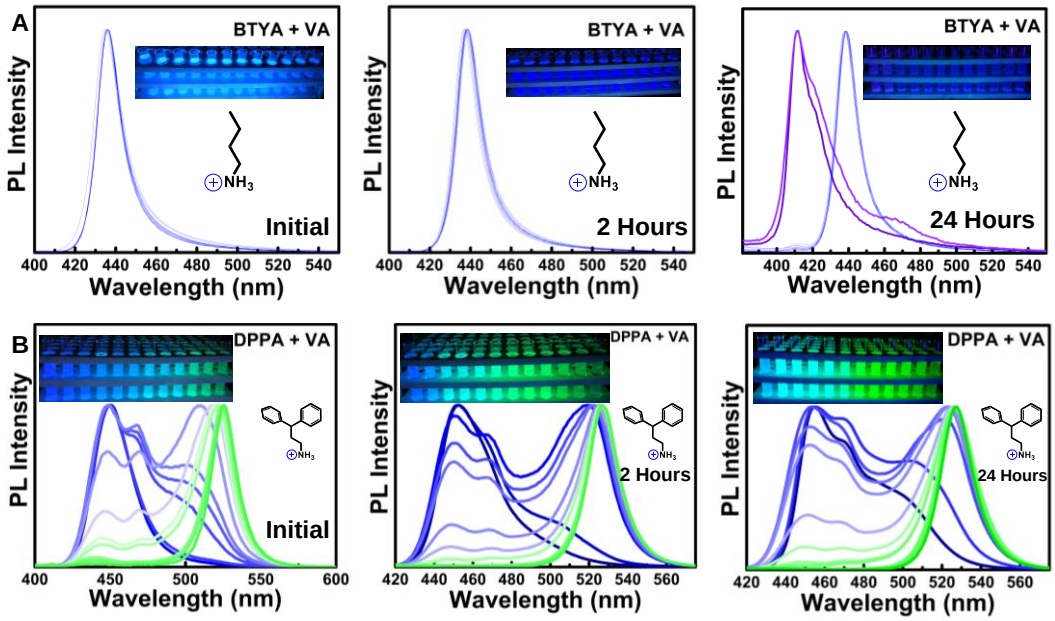

Figure 6.4.5. *PL spectra of (A) BTYA-VA and (B) DPPA-VA PMSCs in a series dilution. PL spectra were measured during the initial dilution, and then after 2 hours and 24 hours. Insets contain digital photographs after each measurement.*

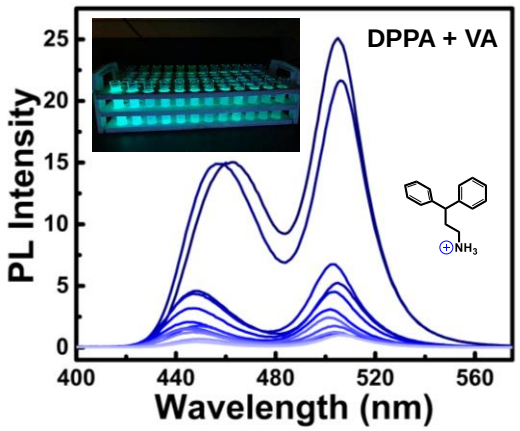

Figure 6.4.6. *DPPA-VA PMSC's PL spectra in a series dilution using chloroform.*

6.4.4. Time-Correlated Single Photon Counting

To determine the exciton lifetime of the BTYA-VA and DPPA-VA PMSCs, time-correlated single-photon counting (TCSPC) was conducted to measure the PL dynamics, as shown in **Figure 6.4.7**. The PL decays were fitted using a double exponential function:

$$L = A_1 e^{(-\frac{t}{\tau_1})} + A_2 e^{(-\frac{t}{\tau_2})}$$

where A_1 and A_2 are the amplitude of the fast and slow components, and τ_1 and τ_2 are the fast and slow component lifetimes, respectively. For the BTYA-VA PMSC sample, τ_1 was calculated to be 0.21 ± 0.01 ns and contributed 87 ± 6 % of the total decay, while τ_2 was 8.52 ± 0.47 ns and contributed 13 ± 6 %. The fast τ_1 decay is attributed to surface trap states. For the DPPA-VA PMSCs, the fast component was calculated to be 3.34 ± 0.66 ns with an amplitude of 47 ± 1 % and the slow component was 7.14 ± 0.78 ns with an amplitude of 57 ± 1 %. Between the two different PMSCs, an almost opposite contribution to fast and slow components is observed. The longer fast component lifetime from DPPA-VA PMSCs compared to the BTYA-VA PMSCs may be due to the larger size of the DPPA-VA PMSCs.[33] However, due to the longer lifetime and larger contribution to the slow component, the BTYA-VA PMSCs may have better passivation and less trap states that cause faster decay of photogenerated charge carriers.

The average lifetime (τ_{av}) was calculated based on the equation:[34]

$$\tau_{av} = \frac{A_1\tau_1^2 + A_2\tau_2^2}{A_1\tau_1 + A_2\tau_2}$$

The τ_{av} for BTYA-VA and DPPA-VA PMSCs was calculated to be 7.34 ± 0.46 ns and 6.08 ± 0.73 ns, respectively. Using the relative PL QY and τ_{av} for BTYA-VA PMSCs the radiative (τ_r) and nonradiative (τ_{nr}) lifetimes were calculated based on the equations:

$$PL\ QY = \frac{\tau_{av}}{\tau_r}$$

$$\tau_{nr} = \frac{\tau_{av}}{1 - \frac{\tau_{av}}{\tau_r}}$$

The τ_r and τ_{nr} lifetime was calculated to be 38.4 ± 2.4 ns and 9.07 ± 2.40 ns for BTYA-VA PMSCs, and for DPPA-VA PMSCs was 55.8 ± 6.7 ns and 6.82 ± 6.69 ns, respectively. For both the PMSCs, nonradiative pathways appear to be the dominate mechanism of relaxation of the exciton. Due to the small size of the PMSCs, trap states may have a more contributing effect on its optical properties. The ligand dependence of the radiative and non-radiative lifetimes indicate that the ligands are an important and integral part of the PMSCs.

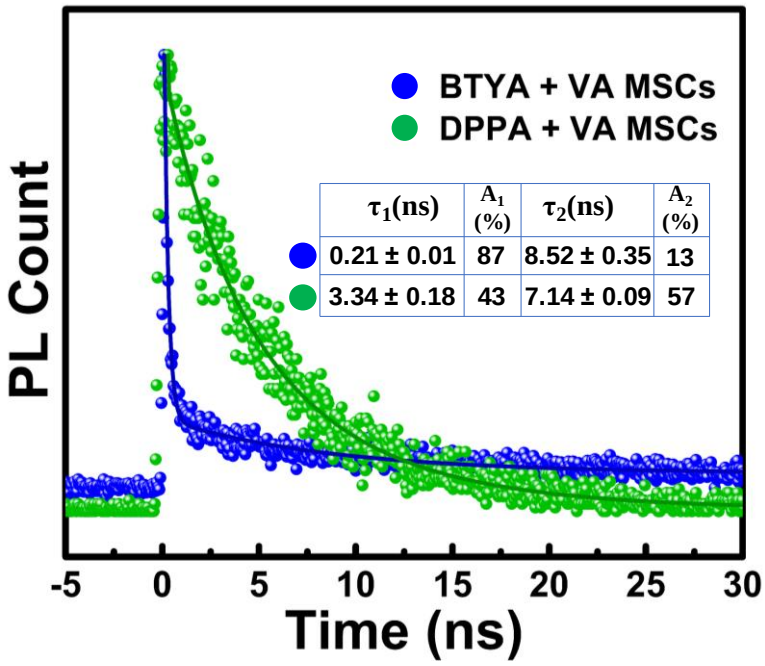

τ_1(ns)	A_1 (%)	τ_2(ns)	A_2 (%)
0.21 ± 0.01	87	8.52 ± 0.35	13
3.34 ± 0.18	43	7.14 ± 0.09	57

Figure 6.4.7. *Time-resolved photoluminescence spectra of (blue) BTYA-VA and (green) DPPA-VA PMSCs.*

6.5. Conclusion

In summary, $CH_3NH_3PbBr_3$ PMSCs were synthesized using two different amine capping ligands, BTYA and DPPA, and the same carboxylic acid, VA. The ligands play a critical role in the formation and growth of PMSCs. For the BTYA-VA PMSC synthesis, a short growth period was observed, followed by a conversion from larger PMSCs with absorbance and PL peaks at 424 nm and 434 nm to smaller PMSCs with an absorbance peak at 405 nm and PL peak at 410 nm. In the DPPA-VA PMSC synthesis, a continuous growth was observed for 24 hours. During this time interval, the increase in absorption intensity and red shift in peak position indicate that the size

of the DPPA-VA PMSCs increased. Another interesting property of the DPPA-VA PMSCs is their ability to generate tunable PL, from 451 nm to 525 nm, by simply diluting to different PMSC concentrations in toluene. This property may be attributed to detachment of ligands from the PMSCs due to strong ligand-solvent molecular interaction and further growth into larger PMSCs or even PQDs. TRPL results suggest that the exciton relaxation is dependent on the passivation ligands and is dominated by nonradiative pathways in both BTYA-VA and DPPA-VA PMSCs, which can be attributed to their very small size and thereby a high density of "surface" defects. Overall, the optical properties, size, and stability of the PMSCs are determined to be strongly ligand dependent and they are potential building blocks for larger nanostructures such as PNCs or PQDs.

6.6. References

(1) Harrell, S. M.; McBride, J. R.; Rosenthal, S. J. Synthesis of Ultrasmall and Magic-Sized CdSe Nanocrystals. *Chem. Mater.* **2013**, *25*, 1199-1210.

(2) Evans, C. M.; Guo, L.; Peterson, J. J.; Maccagnano-Zacher, S.; Krauss, T. D. Ultrabright PbSe Magic-Sized Clusters. *Nano Lett.* **2008**, *8*, 2896-2899.

(3) Ning, J.; Banin, U. Magic Size InP and InAs Clusters: Synthesis, Characterization and Shell Growth. *Chem. Commun.* **2017**, *53*, 2626.

(4) Zhang, B.; Zhu, T.; Ou, M.; Rowell, N.; Fan, H.; Han, J.; Tan, L.; Dove, M. T.; Ren, Y.; Zuo, X., et al. Thermally-Induced Reversible Structural Isomerization in Collodial Semiconductor CdS Magic-Sized Clusters. *Nat. Commun.* **2018**, *9*, 2499.

(5) Zhu, D.; Hui, J.; Rowell, N.; Liu, Y.; Chen, Q. Y.; Steegemans, T.; Fan, H.; Zhang, M.; Yu, K. Interpreting the Ultraviolet Absorption in the Spectrum of 415 nm-Bandgap CdSe Magic-Size Clusters. *J. Phys. Chem. Lett.* **2018**, *9*, 2818-2824.

(6) Peng, L.; Dutta, A.; Xie, R.; Yang, W.; Pradhan, N. Dot-Wire-Platelet-Cube: Step Growth and Structural Transformations in $CsPbBr_3$ Perovskite Nanocrystals. *ACS Energy Lett.* **2018**, *3*, 2014-2020.

(7) Soloviev, V. N.; Eichhöfer, A.; Fenske, D.; Banin, U. Size-Dependent Optical Spectroscopy of a Homologous Series of CdSe Cluster Molecules. *J. Am. Chem. Soc.* **2001**, *123*, 2354-2364.

(8) Peng, Z. A.; Peng, X. Nearly Monodisperse and Shape-Controlled CdSe Nanocrystals via Alternative Routes: Nucleation and Growth. *J. Am Chem. Soc.* **2002**, *124*, 3343-3353.

(9) Bowers II, M. J.; McBride, J. R.; Rosenthal, S. J. White-Light Emission from Magic-Sized Cadmium Selenide Nanocrystals. *J. Am. Chem. Soc.* **2005**, *127*, 15378-15379.

(10) Hsieh, T.-E.; Yang, T.-W.; Hsieh, C.-Y.; Huang, S.-J.; Yeh, Y.-Q.; Chen, C.-H.; Li, E. Y.; Liu, Y.-H. Unraveling the Structure of Magic-Size $(CdSe)_{13}$ Cluster Pairs. *Chem. Mater.* **2018**, *30*, 5468-5477.

(11) Zhang, J.; Hao, X.; Rowell, N.; Kreouzis, T.; Han, S.; Fan, H.; Zhang, C.; Hu, C.; Zhang, M.; Yu, K. Individual Pathways in the Formation of Magic-Size Clusters and Conventional Quantum Dots. *J. Phys. Chem. Lett.* **2018**, *9*, 3660-3666.

(12) Luan, C.; Gokcinar, O. O.; Rowell, N.; Kreouzis, T.; Han, S.; Zhang, M.; Fan, H.; Yu, K. Evolution of Two Types of CdTe Magic-Size Clusters from a Single Induction Period Sample. *J. Phys. Chem. Lett.* **2018**, *9*, 5288-5295.

(13) Xu, Y.; Zhang, Q.; Lv, L.; Han, W.; Wu, G.; Yang, D.; Dong, A. Synthesis of Ultrasmall CsPbBr3 Nanoclusters and their Transformation to Highly Deep-Blue-Emitting Nanoribbons at Room Temperature. *Nanoscale* **2017**, *9*, 17248.

(14) Vickers, E. T.; Graham, T. A. Chowdhury, A. H.; Bahrami, B.; Dreskin, B. W.; Lindley, S.; Bonabi Naghadeh, S.; Qiao, Q.; Zhang, J. Z. Improving Charge Carrier Delocalization in Perovskite Quantum Dots by Surface Passivation with Conductive Aromatic Ligands. *ACS Energy Lett.* **2018**, *3*, 2931-2939.

(15) Bonabi Naghadeh, S.; Luo, B.; Pu, Y.-C.; Schwartz, Z.; Hollingsworth, W. R.; Lindley, S. A.; Brewer, A. S.; Ayzner, A. L.; Zhang, J. Z. Size Dependence of Charge Carrier Dynamics in Organometal Halide Perovskite Nanocrystals: Deciphering Radiative Versus Nonradiative Components. *J. Phys. Chem. C* **2019**, *123*, 4610-4619.

(16) Xu, K.; Vickers, E. T.; Rao, L.; Lindley, S. A.; Allen, A. C.; Luo, B.; Li, X.; Zhang, J. Z. Synergistic Surface Passivation of $CH_3NH_3PbBr_3$ Perovskite Quantum Dots with Phosphonic Acid and (3-Aminopropyl)triethoxysilane. *Chem. Eur. J.* **2019**, *25*, 5014-5021.

(17) Brouwer, A. M. Standards for Photoluminescence Quantum Yield Measurements in Solution (IUPAC Technical Report). *Pure Appl. Chem.* **2011**, *83*, 2213-2228.

(18) Veldhuis, S. A.; Tay, Y. K. E.; Bruno, A.; Dintakurti, S. S. H.; Bhaumik, S.; Muduli, S. K.; Li, M.; Mathews, N.; Sum, T. C.; Mhaisalkar, S. G. Benzyl Alcohol-

Treated $CH_3NH_3PbBr_3$ Nanocrystals Exhibiting High Luminescence, Stability, and Ultralow Amplified Spontaneous Emission Thresholds. *Nano Lett.* **2017**, *17*, 7424-7432.

(19) Krieg, F.; Ochsenbein, S. T.; Yakunin, S.; ten Brinck, S.; Aellen, P.; Suess, A.; Clerc, B.; Guggisberg, D.; Nazarenko, O.; Shynkarenko, Y., et al. Colloidal $CsPbX_3$ (X= Cl, Br, I) Nanocrystals 2.0: Zwitterionic Capping Ligands for Improved Durability and Stability. *ACS Energy Lett.* **2018**, *3*, 641-646.

(20) Jana, A.; Kim, K. S. Water-Stable, Fluorescent Organic-Inorganic Hybrid and Fully Inorganic Perovskites. *ACS Energy Lett.* **2018**, *3*, 2120-2126.

(21) Jha, O.; Yadav, T. K.; Yadav, R. A. Structural and Vibrational Study of a Neurotransmitter Molecule: Dopamine [4-(2-aminoethyl) benzene-1,2-diol]. *Spectrochim. Acta A.* **2018**, *189*, 473-484.

(22) Wang, S.; Wang, Y.; Zhang, Y.; Zhang, X.; Shen, X.; Zhuang, X.; Lu, P.; Yu, W. W.; Kershaw, S. V.; Rogach, A. L. Cesium Lead Chloride/Bromide Perovskite Quantum Dots with Strong Blue Emission Realized via a Nitrate-Induced Selective Surface Defect Elimination Process. *J. Phys. Chem. Lett.* **2019**, *10*, 90-96.

(23) Wheeler, L. M.; Sanehira, E. M.; Marshall, A. R.; Schulz, P.; Suri, M.; Anderson, N. C.; Christians, J. A.; Nordlund, D.; Sokaras, D.; Kroll, T., et al. Targeted Ligand-Exchange Chemistry on Cesium Lead Halide Perovskite Quantum Dots for High-Efficiency Photovoltaics. *J. Am. Chem. Soc.* **2018**, *140*, 10504-10513.

(24) Jeon, N. J.; Noh, J. H.; Kim, Y. C.; Yang, W. S.; Ryu, S.; Seok, S. I. Solvent Engineering for High-Performance Inorganic-Organic Hybrid Perovskite Solar Cells. *Nat. Mater.* **2014**, *13*, 897-903.

(25) Chukwuocha, E. O.; Onyeaju, M. C.; Harry, T. S. T. Theoretical Studies on the Effect of Confinement on Quantum Dots Using the Brus Equation. *WJCMP* **2012**, *2*, 96-100.

(26) Sheng, R.; Ho-Baillie, A.; Huang, S.; Chen, S.; Wen, X.; Hao, X.; Green, M. A. Methylammonium Lead Bromide Perovskite-Based Solar Cells by Vapor-Assisted Deposition. *J. Phys. Chem. C* **2015**, *119*, 3545-3549.

(27) Kudera, S.; Zanella, M.; Giannini, C.; Rizzo, A.; Li, Y.; Gigli, G.; Cingolani, R.; Ciccarella, G.; Spahl, W.; Parak, W. J.; Manna, L. *Adv. Mater.* **2007**, *19*, 548-552.

(28) Cossairt, B. M.; Owen, J. S. *Chem. Mater.* **2011**, *23*, 3114-3119.

(29) Yu, K.; Hu, M. Z.; Wang, R.; Piolet, M. I. L.; Frotey, M.; Zaman, M. B.; Wu, X.; Leek, D. M.; Tao, Y.; Wilkinson, D.; Li, C. *J. Phys. Chem. C* **2010**, *114*, 3329-3339.

(30) Luo, B.; Pu, Y.-C.; Lindley, S.; Yang, Y.; Lu, L.; Li, Y.; Li, X.; Zhang, J. Z. Organolead Halide Perovskite Nanocrystals: Branched Capping Ligands Control Crystal Size and Stability. *Angew. Chem. Int. Ed.* **2016**, *55*, 8864-8868.

(31) Luo, B.; Bonabi Naghadeh, S.; Allen, A.; Li, X.; Zhang, J. Z. Peptide-Passivated Lead Halide Perovskite Nanocrystals Based on Synergistic Effect Between Amino and Carboxylic Functional Groups. *Adv. Funct. Mater.* **2017**, *27*, 1604018.

(32) Krieg, F.; Ochsenbein, S. T.; Yakunin, S.; ten Brinck, S.; Aellen, P.; Süess, A.; Clerc, B.; Guggisberg, D.; Nazarenko, O.; Shynkarenko, Y.; Kumar, S.; Shih, C.-J.; Infante, I.; Kovalenko, M. V. Colloidal $CsPbX_3$ (X = Cl, Br, I) Nanocrystals 2.0: Zwitterionic Capping Ligands for Improved Durability and Stability. *ACS Energy Lett.* **2018**, *3*, 641-646.

(33) de Mello Donega´, C.; Koole, R. Size Dependence of the Spontaneous Emission Rate and Absorption Cross Section of CdSe and CdTe Quantum Dots. *J. Phys. Chem. C* **2009**, *113*, 6511−6520.

(34) Zhang, M.; Tian, Z.-Q.; Zhu, D.-L.; He, H.; Guo, S.-W.; Chen, Z.-L.; Pang, D.-W. Stable $CsPbBr_3$ Perovskite Quantum Dots with High Fluorescence Quantum Yields. *New J. Chem.* **2018**, *42*, 9496.